

TOMMI MIKKONEN

# Fourier Transform Photoacoustic Spectroscopy with Broadband Lasers



TOMMI MIKKONEN

Fourier Transform  
Photoacoustic Spectroscopy  
with Broadband Lasers

ACADEMIC DISSERTATION

To be presented, with the permission of  
the Faculty of Engineering and Natural Sciences  
of Tampere University,  
for public discussion in the auditorium TB109  
of the Tietotalo, Korkeakoulunkatu 1, Tampere,  
on 28 April 2023, at 12 o'clock.

# ACADEMIC DISSERTATION

Tampere University, Faculty of Engineering and Natural Sciences  
Finland

*Responsible  
supervisor  
and Custos*

Professor Juha Toivonen  
Tampere University  
Finland

*Pre-examiners*

Professor Tobias Herr  
Universität Hamburg  
Germany

Docent Tom Kuusela  
University of Turku  
Finland

*Opponent*

Professor Vincenzo Spagnolo  
Politecnico di Bari  
Italy

The originality of this thesis has been checked using the Turnitin OriginalityCheck service.

Copyright ©2023 author

Cover design: Roihu Inc.

ISBN 978-952-03-2844-3 (print)

ISBN 978-952-03-2845-0 (pdf)

ISSN 2489-9860 (print)

ISSN 2490-0028 (pdf)

<http://urn.fi/URN:ISBN:978-952-03-2845-0>



Carbon dioxide emissions from printing Tampere University dissertations have been compensated.

PunaMusta Oy – Yliopistopaino  
Joensuu 2023







# PREFACE

This work was carried out in the Applied Optics research group in the Photonics Laboratory at Tampere University partly in collaboration with the Ultrafast Photonics group. I gratefully acknowledge the financial support from the Faculty of Engineering and Natural Sciences and the technical support from Gasera. Moreover, I acknowledge Fulbright Finland Foundation, Vilho, Yrjö and Kalle Väisälä Foundation and Emil Aaltonen Foundation for supporting my research visit to the United States.

I would like to thank Prof. Juha Toivonen for the trust and guidance since my first summer internship in 2016. The numerous opportunities you have provided have been a solid foundation for my professional career. Likewise, I thank Prof. Goëry Genty for his mentorship and thorough investment in my scientific writing. I would also like to thank Prof. Gerard Wysocki for warmly welcoming me to Princeton University and for the punctual support during my visit. I also thank Prof. Alexandra Foltynowicz for the opportunity to collaborate and visit Umeå University twice, and Prof. Markku Vainio for generously providing me a work environment in Helsinki, and both of them for the support in my funding applications.

I have had the privilege to belong in the most supportive and friendly work environments during the past seven years. I want to sincerely thank all the people I have spent time with in Tampere, Helsinki, Princeton and Umeå. This includes my room mates, group members, football and volleyball players, Optica student chapter officers, lunch and conference trip companions, lab buddies, and co-authors.

Finally, I thank my parents Markku and Marja-Leena for their continuous support during my 21 years of studies, and my partner Emilia for always supporting my dreams and brightening my days.

Princeton, December 2022

Tommi Mikkonen



# ABSTRACT

Gas sensing plays a key role in the progress towards a healthier, safer and more sustainable society. The amount of gas sensing applications are immense with varying requirements, and thus numerous sensors with different characteristics are needed. This thesis contributes to the task by introducing a new optical gas sensing technique, Fourier transform photoacoustic spectroscopy (FT-PAS) implemented with a spectrally broadband mid-infrared laser and a sensitive cantilever microphone. The main benefits of FT-PAS are the fast acquisition of a wide spectral range that is only limited by the light source, and the effective enhancement of sensitivity with a high-power light source. Two light sources are demonstrated in this thesis, namely an incoherent fiber-based supercontinuum and a frequency down-converted mode-locked optical frequency comb. Besides high power spectral density, the advantage of broadband lasers stems from their high spatial coherence enabling high spectral resolution and efficient coupling to multipass cells.

The performance of cantilever-enhanced FT-PAS is excellent while requiring a sample volume of less than ten milliliters. The detection limit for methane is 90 parts per billion in five seconds, which can be significantly lowered through longer averaging. The highest demonstrated spectral resolution is  $0.013\text{ cm}^{-1}$  with no compromise in the detection sensitivity and limited by pressure broadening. However, two orders of magnitude worse spectral resolution already provides sufficient selectivity for complex multi-species detection. The unique combination of high performance and low gas consumption makes the technique attractive for the analysis of volatile substances and samples with limited availability. The detection of chemical warfare agents for forensic crime scene investigation and online warning systems is one potential application of the technique demonstrated in this thesis. In the near future, both the performance and the applicability of FT-PAS are expected to remarkably improve, establishing the technique as a notable alternative in many industrial, medical and security applications.



# TIIVISTELMÄ

Kaasujen havainnointi on merkittävässä roolissa kestävän, terveellisen ja turvallisen yhteiskunnan luomisessa. Lukuisten eri sovelluskohteiden vaatimukset kaasujen havainnointiin vaihtelevat valtavasti, ja siksi useita erityyppisiä sensoreita tarvitaan. Tämä väitöskirja edistää tätä tavoitetta esittelemällä uuden optisen kaasujen havainnointitekniikan, valoakustisen Fourier-muunnosspektroskopian laajakaistaisella keski-infrapunlaserilla ja herkällä läppämikrofonilla. Tekniikan merkittävimmät hyödyt ovat laajan, ainoastaan valonlähteen rajoittaman spektrisen kaistan nopea mittaus sekä herkkyyden tehokas parantaminen valonlähteen tehoa kasvattamalla. Tässä väitöskirjassa käytettyjen valonlähteiden, superjatkumon ja optisen taajuuskamman hyöty suuren optisen tehotiheyden lisäksi on korkea paikkakoherenssi, joka mahdollistaa erinomaisen spektrisen resoluution sekä tehokkaan kytkennän moniläpäisykammioon.

Tekniikan suorituskkyky on erinomainen vaadittavan näytetilavuuden ollessa alle kymmenen millilitraa. Metaanin havaintoraja viiden sekunnin mittausajalla on 90 miljardisosaa, jota voidaan parantaa merkittävästi keskiarvoistamalla. Korkein demonstroitu spektrinen resoluutio on  $0.013 \text{ cm}^{-1}$ , joka ei heikennä systeemin herkkyyttä ja jota rajoittaa paineleveneminen. Kaksi kertaluokkaa huonompi spektrinen resoluutio kuitenkin mahdollistaa jo hyvän selektiivisyyden monen kaasun samanlaiseen havainnointiin. Hyvän suorituskyvyn ja pienen näytetilavuuden ainutlaatuisen yhdistelmän ansiosta tekniikka on potentiaalinen esimerkiksi haihtuvien yhdisteiden ja saatavuudeltaan rajoitettujen näytteiden analysoimiseen. Eräs potentiaalinen ja tässä väitöskirjassa demonstroitu sovelluskohde on kemiallisten taistelua-aineiden havaitseminen rikostutkinnassa ja jatkuvatoimisissa varoitusjärjestelmissä. Lähitulevaisuudessa sekä tekniikan suorituskyvyn että sovellettavuuden odotetaan kehittyvän merkittävästi, mikä vahvistaa tekniikan asemaa vaihtoehtona teollisiin, lääketieteellisiin ja turvallisuussovelluksiin.





# CONTENTS

Preface . . . . .	v
Abstract . . . . .	vii
List of symbols and abbreviations . . . . .	xvi
Original publications . . . . .	xvii
1 Introduction . . . . .	1
1.1 Aim and scope of the work . . . . .	4
1.2 Structure of the thesis . . . . .	5
2 Optical gas sensing . . . . .	7
2.1 Ro-vibrational energy levels and transitions . . . . .	7
2.2 Analytical absorption spectroscopy . . . . .	11
2.3 Absorption spectroscopy techniques . . . . .	12
2.4 Broadband light sources . . . . .	15
3 Photoacoustic spectroscopy . . . . .	19
3.1 Operation principle . . . . .	19
3.2 Noise sources . . . . .	22
3.3 Instrumentation . . . . .	24
4 Fourier transform photoacoustic spectroscopy . . . . .	29
4.1 Operation principle . . . . .	29
4.2 Experimental setups . . . . .	32
4.3 Noise characteristics . . . . .	37

5	Performance characteristics . . . . .	43
5.1	Detection limit . . . . .	43
5.2	Dynamic range and linearity . . . . .	46
5.3	Accuracy . . . . .	47
5.4	Stability . . . . .	50
5.5	Multi-species detection . . . . .	52
6	Applications . . . . .	55
6.1	Hydrocarbons and volatile organic compounds . . . . .	55
6.2	Chemical warfare agents . . . . .	57
7	Conclusions . . . . .	61
	References . . . . .	65
	Publication I . . . . .	89
	Publication II . . . . .	95
	Publication III . . . . .	105
	Publication IV . . . . .	111
	Publication V . . . . .	121

# LIST OF SYMBOLS AND ABBREVIATIONS

AWD	Allan-Werle deviation
CWA	chemical warfare agent
DAS	direct absorption spectroscopy
DCS	dual-comb spectroscopy
DGA	dissolved gas analysis
DIMP	diisopropyl methylphosphonate
FFT	fast Fourier transform
FTIR	Fourier transform infrared (spectroscopy/spectrometer)
FT-PAS	Fourier transform photoacoustic spectroscopy
FTS	Fourier transform spectroscopy
HITRAN	high-resolution transmission molecular absorption database
ICL	interband cascade laser
IR	infrared
LED	light emitting diode
LOD	limit of detection
NDIR	non-dispersive infrared
OFC	optical frequency comb
OPD	optical path difference
OPO	optical parametric oscillator
PA	photoacoustic
PAA	photoacoustic analyser

PAS	photoacoustic spectroscopy
ppb	parts per billion by volume
ppm	parts per million by volume
ppt	parts per trillion by volume
PSD	power spectral density
QCL	quantum cascade laser
QTF	quartz tuning fork
RF	radio frequency
RIN	relative intensity noise
SC	supercontinuum
SI	scanning interferometer
SNR	signal-to-noise ratio
TDLAS	tunable diode laser absorption spectroscopy
VOC	volatile organic compound

$A$	cross sectional area of the gas cell
$B$	rotational constant
$c$	concentration as volume mixing ratio
$C_{\text{cell}}$	cell constant
$C_v$	heat capacity
$E$	energy
$E_{\text{rot}}$	rotational energy
$E_{\text{vib}}$	vibrational energy
$F$	optical enhancement factor
$f$	frequency
$I$	intensity
$I_0$	original intensity

$J$	rotational quantum number
$L$	optical path length
$l$	length of the gas cell
$m$	sensitivity
$N$	molecular number density
$N_p$	number of passes
$P$	optical power
$p$	pressure
$P_0$	original optical power
$P_I$	optical power incident to the gas cell
$P_N$	low-pass filtered noise in optical power
$Q$	heat energy
$R_m$	mirror reflectance
$S$	photoacoustic signal
$S_0$	amplitude of the photoacoustic signal
$S_B$	background signal
$S_m$	microphone sensitivity
$T$	temperature
$T_0$	ambient temperature
$T_w$	window transmission
$v$	vibrational quantum number
$V_{OPD}$	optical path difference scan velocity
$x$	optical path difference
$\alpha$	absorption coefficient
$\delta$	phase shift
$\Delta\nu$	spectral resolution

$\Delta P$	change in optical power
$\Delta p$	pressure change
$\Delta T$	temperature change
$\eta_{\text{nr}}$	efficiency of thermal relaxation
$\Lambda$	instrument lineshape function
$\lambda$	wavelength
$\nu$	wavenumber
$\Pi$	boxcar function
$\sigma$	absorption cross section or noise
$\sigma_{\text{LS}}$	source-induced noise
$\sigma_{\text{T}}$	thermal noise
$\sigma_{\text{tot}}$	total noise

## ORIGINAL PUBLICATIONS

- Publication I      T. Mikkonen, C. Amiot, A. Aalto, K. Patokoski, G. Genty and J. Toivonen. Broadband cantilever-enhanced photoacoustic spectroscopy in the mid-IR using a supercontinuum. *Optics Letters* 43.20 (2018), 5094–5097.
- Publication II     I. Sadiq, T. Mikkonen, M. Vainio, J. Toivonen and A. Foltynowicz. Optical frequency comb photoacoustic spectroscopy. *Physical Chemistry Chemical Physics* 47.44 (2018), 27849–27855.
- Publication III    T. Mikkonen, Z. Eslami, G. Genty and J. Toivonen. Supercontinuum intensity noise coupling in Fourier transform photoacoustic spectroscopy. *Optics Letters* 47.7 (2022), 1713–1716.
- Publication IV    T. Mikkonen, T. Hieta, G. Genty and J. Toivonen. Sensitive multi-species photoacoustic gas detection based on mid-infrared supercontinuum source and miniature multipass cell. *Physical Chemistry Chemical Physics* 24 (2022), 19481–19487.
- Publication V     T. Mikkonen, D. Luoma, H. Hakulinen, G. Genty, P. Vanninen and J. Toivonen. Detection of gaseous nerve agent simulants with broadband photoacoustic spectroscopy. *Journal of Hazardous Materials* 440 (2022), 129851.

### *Author's contribution*

This thesis summarizes five peer-reviewed publications. Their key results and the author's contribution to each of these publications are described below.

- Publication I      In this article, we demonstrate a supercontinuum light source in

Fourier transform photoacoustic spectroscopy for the first time. J. Toivonen planned the experiment, and C. Amiot developed the supercontinuum source. The author built the rest of the experimental setup with the help of co-authors, carried out most of the experiments and data analysis, and contributed to the preparation of the manuscript along with the co-authors.

Publication II      This paper reports high-resolution Fourier transform photoacoustic spectroscopy with an optical frequency comb light source. The experiment was planned by M. Vainio, A. Foltynowicz and J. Toivonen. I. Sadiek and the author constructed the experimental setup and conducted the experiments. I. Sadiek analysed the data and prepared the manuscript, while all authors contributed to the finalization of the paper.

Publication III     This letter describes the effect of the intensity fluctuations of the light source on the noise in Fourier transform photoacoustic spectroscopy. The author planned the experiments with the help of co-authors, built the spectroscopic experimental setup, carried out the spectroscopic experiments, simulations and data analysis, and prepared the manuscript. Z. Eslami carried out the relative intensity noise experiment. G. Genty and J. Toivonen contributed to finalizing the publication.

Publication IV      In this publication, a significant improvement in the sensitivity of Fourier transform photoacoustic spectroscopy is reported. The author was responsible for the experimental design, carrying out the experiments and data analysis, and writing the manuscript. T. Hieta assisted in the designing and construction of the multipass arrangement. All authors contributed to the planning of the work and the finalization of the paper.

Publication V        This article reports the application of supercontinuum-based Fourier transform photoacoustic spectroscopy for the detection of nerve agents. The study was planned by the author, J. Toivonen, H. Hakulinen and P. Vanninen. The author carried out the



experiments and analysed the data with the help of D. Luoma, and prepared the manuscript. G. Genty and J. Toivonen contributed to finalizing the publication.



# 1 INTRODUCTION

Information is increasingly gathered from the surroundings for higher automation, sustainability and safety. Besides weather parameters [1, 2], material identities [3] and three-dimensional maps of urban environments and forests [4, 5], one of the most fundamental parameters to assess is the composition of air which both affects and provides insight on industrial processes [6–13], the climate [14–18] and human health [19–25]. Monitoring the production conditions and emissions of industrial processes improves the product quality and minimizes raw material, energy and waste, examples ranging from fruit storage (chemicals emitted from fruits indicate ripening) [10] to detecting natural gas leaks [18, 26]. Localizing and reducing greenhouse gas emissions is also crucial in the context of global warming [27], which has led to significant emission restrictions in fossil fuel combustion and automotive industry [28, 29]. Moreover, many industrial air pollutants such as nitrogen oxides, carbon monoxide and formaldehyde should be monitored in urban environments and indoor air due to their damaging impact on human health [19]. Less frequently but even more detrimentally, gas sensing is needed in the detection of more lethal substances such as chemical warfare agents for screening, diagnosing poisoning and forensic investigation [20, 21].

Each application has its unique requirements for assessing the composition of air. Arguably the most important requirements are selectivity and dynamic range, which describe the ability to detect the target substance reliably, that is with a sufficiently small interference from other gas species, and the range of concentrations that can be analysed, respectively. Concentrations of gas species are generally expressed as volume mixing ratios with typical units of percent by volume (%), parts per million by volume (ppm), parts per billion by volume (ppb) and parts per trillion by volume (ppt) [30]. Detecting low concentrations is especially crucial for the monitoring of atmospheric trace gases [15] and breath analysis for disease diagnostics [24], while the monitoring of combustion processes [11–13] and gas leaks [18, 26] require oper-

ation also at high concentrations. Detection limit describes the smallest detectable concentration. In the literature, however, a term (detection) sensitivity is often used instead, although sensitivity generally refers to a change in sensor output (e.g., voltage) per input quantity (e.g., concentration). Other relevant sensing requirements are response time, precision, ability to detect multiple species, required sample volume and stability/lifetime, in addition to more practical features such as susceptibility to surrounding conditions (i.e., temperature, vibrations), calibration procedure, autonomous operation and footprint (size, weight, cost, energy consumption) [31].

A massive variety of gas sensing technologies exist to satisfy the specific needs of different applications [30–32]. The simplest methods rely on sensing elements such as metal oxide semiconductors [33–35], conductive polymers [36] or carbon nanomaterials [37], whose electrical properties change when specific gas molecules are in contact with the material. The gas adsorption on the sensing material can alternatively be monitored acoustically, most commonly using a quartz crystal resonator whose resonance frequency varies with the additional mass of the element [38]. Another simple sensing principle relies on burning the target gas and monitoring the released heat energy, which is practical for combustible gases and for gases whose thermal conductivity differs from that of air [31, 39]. The aforementioned sensors typically have a very small footprint with sufficiently low detection limits, but usually they suffer from low selectivity, sensitivity to environmental factors and/or long-term instability [30–32]. A traditional gas sensing technology with a high performance is gas chromatography, which separates gas compounds according to their relative vapor pressures before detecting them one after another typically by burning or with a mass spectrometer [40]. Although extremely sensitive and selective, the method is also slow and has a large footprint [30, 31].

Optical gas sensing methods take advantage of molecule-specific interactions between light and a gas medium. These interactions are conventionally studied as a function of wavelength, thus the field of study is known as optical spectroscopy. Optical sensors are generally rapid, stable and insensitive to environmental interference [41]. Moreover, the selectivity is typically high and the detection limits low, but the sensor performance varies greatly between different techniques. Optical sensors based on the absorption of light are the most typical for gas-phase molecular detection, the majority of such techniques monitoring the attenuation of light in the gas medium [30]. A fundamental disadvantage of the attenuation-based approach is

the detection of small changes from a large background signal, which can be overcome with background-free, i.e., emissive, approaches where the signal is ideally zero without an analyte and only appears when the analyte is present. However, many implementations of so-called background-free techniques do have a small background feature that needs to be addressed. One of the most popular emissive techniques is photoacoustic spectroscopy (PAS). In PAS, periodic illumination of the gas medium produces local heating and pressure variations (i.e., sound waves) in the medium, which are listened and recorded with a microphone [42]. The amplitude of the sound signal is directly proportional to the incident optical power, thus lasers are conventionally employed for higher sensitivity. Inherently low detection limits can be further reduced with a sensitive pressure transducer such as an interferometrically read thin cantilever [43], which enables sub-ppt detection in a sample volume of a few milliliters [44].

Laser-based absorption spectroscopy provides fast gas sensing with high sensitivity and selectivity, but the ability for multi-species detection is restricted by the tuning range of the laser. Spectrally broadband detection is typically carried out using a light source with a wide spectral coverage by dispersing its spectral components with a grating and analysing them separately [30]. Wavelength-scanning is however time-consuming, and thus Fourier transform spectroscopy (FTS) has become an extremely popular method. FTS relies on a well-known connection (Fourier transform) between temporally recorded sinusoidal waves and their frequency content. This enables the measurement of the source spectrum by recording its total (frequency down-converted) intensity over a certain time period [45]. Thermal emitters are by far the most used light sources in FTS due to their small footprint and a suitable emission spectrum. However, novel laser-based broadband emitters such as supercontinuum (SC) sources and optical frequency combs (OFCs) have been increasingly applied to FTS [46–52] and absorption spectroscopy in general [53, 54]. These sources have a unique combination of high emission power, a wide spectral bandwidth and directionality, and are still under significant research and development [55, 56].

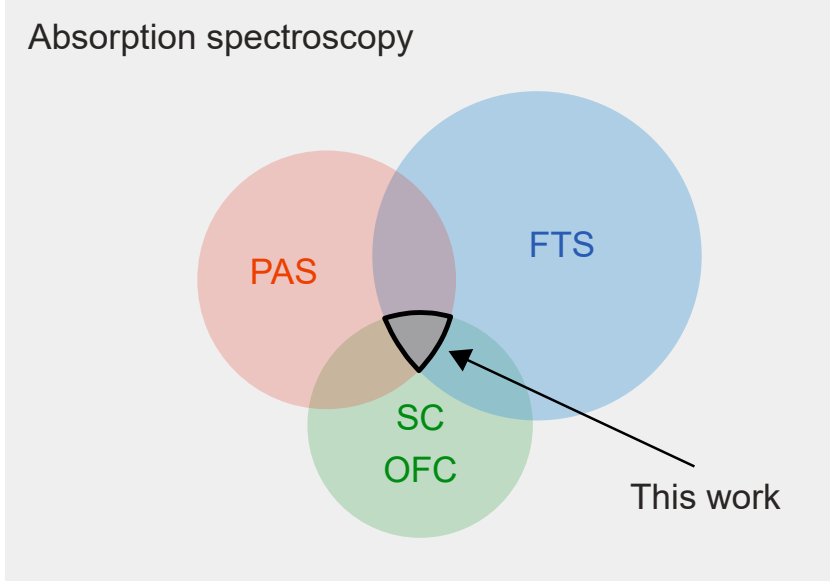


**Figure 1.1** Venn diagram of the research area of this thesis in the context of absorption spectroscopy.

## 1.1 Aim and scope of the work

This thesis studies FTS with SC and OFC light sources and cantilever-enhanced photoacoustic detection for gas sensing. This new technique combines three research fields in absorption spectroscopy as illustrated in Fig. 1.1. These research fields have been studied in pairs in the past [46–52, 57–66], but the particular combination of the three fields has remained unexplored.<sup>1</sup> The advantages of the technique depend on the basis of comparison. Compared to traditional FTS with SC and OFC light sources [46–52], photoacoustic detection with a cantilever microphone is expected to yield higher sensitivity and lower sample consumption. As for the comparison to SC-based PAS with optical filters [57–59], FTS provides faster detection with better selectivity. Finally, compared to photoacoustic FTS using a thermal emitter [60–66], SC and OFC sources should improve the sensitivity through higher optical power and better coupling to multipass cells and cavities.

The objective of this thesis is thorough investigation of this technique and its

<sup>1</sup>After the first publications of this thesis, the research area of this work has been further studied elsewhere [67–71].

future potential. The key research questions of the thesis are:

- Is the technique experimentally realizable?
- What is the performance of the technique?
- What benefits and problems are characteristic to the technique compared to competing methods?
- What are the potential application areas for the technique?

The research is carried out through an extensive literature review and experimental inquiries supported by theoretical and numerical studies. The research questions are investigated in five peer-reviewed publications listed in the appendices, which include the first experimental demonstration of the technique, the characterization of noise, extensions to the performance in terms of detection limit, spectral resolution and multi-species detection, and the demonstration of the technique in a selected application.

## 1.2 Structure of the thesis

This thesis consists of seven chapters introducing the rich field of optical gas sensing, describing the applied technique and presenting the key results. Chapter 1 describes gas sensing in general and briefly outlines the field of absorption spectroscopy treated in more detail in Chapter 2. In this chapter, the physical background of light absorption by gas-phase molecules and the analytical description of absorption spectroscopy along with the most prominent techniques are discussed. Moreover, an overview of infrared (IR) light sources with a wide spectral bandwidth is given, focusing on SC and OFC sources. Chapter 3 gives a detailed description of PAS including the analytical treatment of the sound wave formation and detection, noise sources and different implementations. FTS is discussed in Chapter 4 focusing on the implementation with photoacoustic detection, along with the summary of experimental systems used in this thesis and the characterization of noise. Chapter 5 presents the performance characteristics of the technique in terms of detection limit, dynamic range, accuracy, stability and multi-species detection. In Chapter 6, the potential of the developed technique to selected application areas is discussed. The focus is on the detection of chemical warfare agents supported by experimental results. Chapter 7 summarizes the key findings of the thesis, connects the reported technique and

its performance to other optical gas sensing methods, and suggests future research directions.



## 2 OPTICAL GAS SENSING

Optical sensing methods utilize different interactions between electromagnetic radiation and matter to reveal various properties of the probed material and its surroundings [41]. Material identities and concentrations are the most wanted properties, which are discoverable by each substance's unique wavelength-dependent response to light and the magnitude of this response, respectively. Light-matter interactions are therefore studied as a function of wavelength, and experimental methods of this type are called optical spectroscopy. In this chapter, the physical background of the molecule-specific response to light is discussed. Resulting from quantized energy levels of molecules, light-matter interactions such as absorption, emission and scattering are presented with the most focus directed on gas-phase absorption spectroscopy of molecules. Finally, widely employed absorption spectroscopy techniques and different spectrally broadband IR light sources are reviewed.

### 2.1 Ro-vibrational energy levels and transitions

A molecule may store kinetic and potential energy mainly in five ways in the gas phase: as translational (kinetic), electronic (potential), vibrational (potential, kinetic), rotational (kinetic) and nuclear (potential) energy [72]. Electronic energy is related to the distribution of electrons around the nuclei (molecular orbitals), and translational/vibrational/rotational energies simply correspond to the physical motions of the molecule. Contrary to translational and rotational motion, vibrations of large molecules can be very complicated. Fortunately, any complex vibration can be considered as a combination of so-called normal vibrations, in which all nuclei experience harmonic motion with the same frequency and phase [73]. As an example, normal vibrational modes of methane ( $\text{CH}_4$ ) are shown in Fig. 2.1, where three of the vibrations are degenerate, that is there are more than one normal vibration at the same frequency.

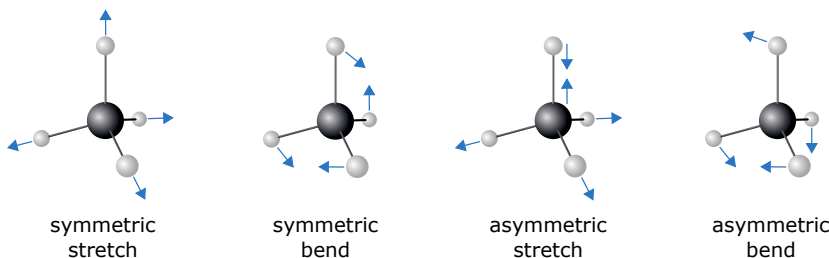


**Figure 2.1** Normal vibrational modes of methane. The arrows indicate movement of the nuclei during one half of the motion while the movement is opposite during the other half. Symmetric bend is doubly degenerate and both asymmetric vibrations are triply degenerate.

In contrast to classical particles which may possess any amount of energy, electronic, vibrational, rotational and nuclear energy of a molecule may only have discrete values [72]. These quantized energy levels all contain information about the molecule, but molecular structure is especially clearly recorded in the vibrational and rotational levels. In the strongest approximation, considering the vibration of a harmonic oscillator and the rotation of a rigid rotor (linear molecule), combined vibrational and rotational (ro-vibrational) energy can be written

$$E = E_{\text{vib}}(v_i) + E_{\text{rot}}(v_i, J) = hc_0 \nu \left( v_i + \frac{1}{2} \right) + B_{v_i} J(J+1), \quad (2.1)$$

where  $h$  is the Planck constant,  $c_0$  is the speed of light,  $\nu$  is the classical vibration wavenumber,  $v_i$  is the vibrational quantum number for normal vibration  $i$ ,  $B_{v_i}$  is the rotational constant and  $J$  is the rotational quantum number [73]. In a more accurate treatment, the vibrational energy term takes into account the anharmonicity and the degeneracy of the vibration, and the rotational energy term includes centrifugal distortion, Coriolis interaction and additional terms for nonlinear molecules [73].

Ro-vibrational energy levels are schematically illustrated in Fig. 2.2, which includes the ground and the first excited vibrational levels and the first five rotational levels for these two vibrational levels. An isolated molecule occupies its lowest energy state ( $v = 0$  and  $J = 0$ ), but the insertion of sufficient energy transitions the molecule to a higher energy level. When considering electromagnetic radiation, electronic transitions require ultraviolet or visible light, vibrational transitions IR radiation and rotational transitions far-IR light [73]. An excited molecule eventually relaxes back to the ground state via different decay mechanisms [41]. The dominant

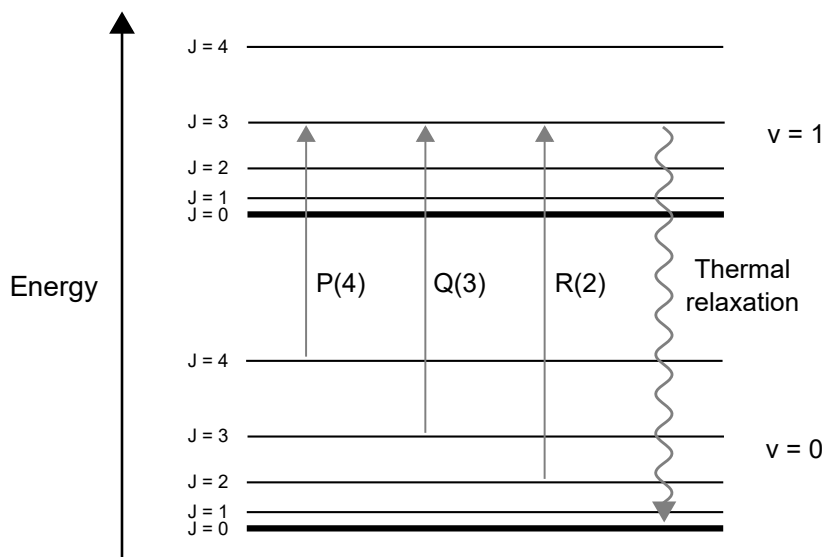


**Figure 2.2** A schematic of a ro-vibrational energy diagram for the first two vibrational levels and the first five rotational levels. The difference between the pure vibrational and pure rotational energy spacing is exaggerated and is typically two orders of magnitude. Three transitions corresponding to different changes in the rotational quantum number are shown as straight arrows. The curved arrow illustrates thermal relaxation, where the transition from the excited state to the ground state occurs gradually via collisions.

decay path in the IR region is non-radiative involving a gradual release of energy to the surroundings via collisions and hence increasing the local temperature of the medium (curved arrow in Fig. 2.2). Neglecting resonant energy transfer (to another molecule) and the formation of triplet states, the emission of a photon is another relevant decay process mostly utilized in electronic spectroscopy.

Ro-vibrational energy levels are conventionally studied with two light-induced excitation processes, absorption and Raman scattering [41, 73]. Raman scattering occurs when the photon energy exceeds the transition energy and the electron cloud of the molecule oscillates with the photon's electric field, radiating similar to an antenna at the original frequency. Certain molecular rotations and vibrations at lower frequencies modulate the polarizability of the medium, which results in additional frequencies in the scattered radiation [41]. These new frequencies are symmetrically around the original frequency and displaced by the transition energy. In the absorption process on the other hand, the electric field of a photon whose energy matches the transition drives the molecule to vibrate and rotate, transferring its energy to the

molecule. The vibrational transition is only possible when the vibration changes the charge distribution of the molecule, that is there is a change in the dipole moment during the vibration, while the rotational transition requires permanent dipole moment from the molecule [73]. It follows that ro-vibrational absorption cannot be utilized in the detection of homonuclear molecules such as nitrogen and oxygen, which fortunately produce Raman scattering due to their polarizability-changing vibrations. In general, absorption is more widely utilized process for gas-phase samples due to the weakness of Raman scattering.

Selection rules limit the possible transitions from one energy level to another. Besides restrictions on the dipole moment, the vibrational selection rule is  $\Delta v_i = \pm 1$  in the harmonic oscillator approximation, but anharmonicity enables also the usually weak overtone transitions with  $\Delta v_i = \pm 2, \pm 3, \dots$  [73]. Transitions involving more than one normal vibration are also allowed and called combination tone transitions. For absorption, the rotational selection rule is generally  $\Delta J = 0, \pm 1$ , but  $J = 0$  is not always allowed, for example for most diatomic molecules [73]. This gives rise to three (or two) branches in the ro-vibrational spectrum, namely an R-branch ( $\Delta J = +1$ ), a P-branch ( $\Delta J = -1$ ) and a Q-branch ( $\Delta J = 0$ ). One transition from each branch is illustrated in Fig. 2.2, where the number in parenthesis describes the initial rotational quantum number.

The strength of the transition depends on the magnitude of the dipole moment associated with the corresponding molecular movement (transition moment) and the population of the initial state [73]. A typical quantity that contains these factors is the absorption cross section, which can be considered as the absorption probability for a single molecule or an effective cross sectional area of the molecule where the photon must hit to be absorbed [41, 74]. As an example, the absorption cross section of the fundamental ( $v = 0 \rightarrow v = 1$ ) asymmetric stretching band of  $\text{CH}_4$  is shown in Fig. 2.3. Three branches and the population distribution (thermal excitation to rotational levels) are clearly visible. Although not properly visible in Fig. 2.3, the transitions are not indefinitely narrow but are broadened by several mechanisms. The fundamental limitation for the linewidth stems from the Heisenberg uncertainty principle, stating that the finite excitation lifetime smears out the transition energy/frequency. In practice, the transition linewidth is limited by pressure broadening (energy exchange in collisions) and Doppler broadening (frequency shift due to molecular motion) [73]. Depending on the conditions, a single transition

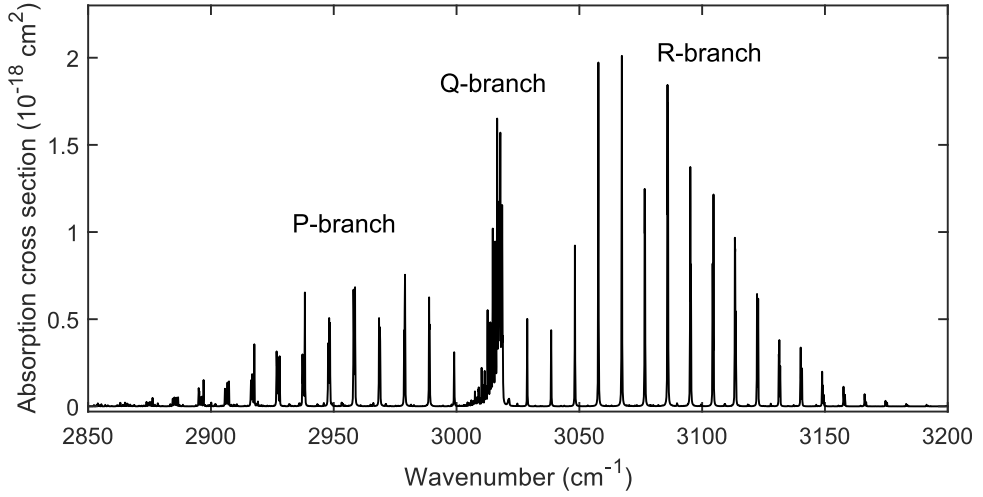


**Figure 2.3** A ro-vibrational absorption cross section spectrum of the fundamental asymmetric stretching of  $\text{CH}_4$ , modelled using the HITRAN database [75]. Three branches corresponding to different changes in the rotational quantum number are visible.

can be considered to have a Gaussian (Doppler broadening dominant), a Lorentzian (pressure broadening dominant) or a Voigt profile (a combination of Gaussian and Lorentzian profiles) [41, 73]. For larger molecules than  $\text{CH}_4$ , line broadening may lead to the disappearance of individual lines and the formation of broad absorption features.

## 2.2 Analytical absorption spectroscopy

The optical power of IR radiation propagating through a gas medium decreases exponentially at optical frequencies matching the allowed and broadened ro-vibrational transitions. This effect is formulated by the Beer-Lambert law,

$$\frac{P(\nu)}{P_0(\nu)} = e^{-\alpha(\nu)L} \approx 1 - \alpha(\nu)L, \quad (2.2)$$

which states the relation between the original and transmitted optical powers  $P_0(\nu)$  and  $P(\nu)$ , the absorption coefficient  $\alpha(\nu)$  and the optical path length  $L$ . For future convenience, the formula is written here using optical powers instead of more popular intensities or irradiances [30, 41], which are directly related considering the entire

cross sectional area of the probe beam. Moreover, optical frequencies are described by wavenumbers  $\nu = 1/\lambda$ , where  $\lambda$  is the wavelength. Molecule-specific absorption coefficients are extremely small in the gas phase, and thus the first order Taylor approximation is often used for the Beer-Lambert law to yield a simpler linear form shown in Eq. 2.2. The absorption coefficient can be written as

$$\alpha(\nu) = N \sum_i [\sigma_i(\nu) c_i], \quad (2.3)$$

where  $N$  is the total number density of the medium and  $\sigma_i(\nu)$  and  $c_i$  are the absorption cross section and the concentration (as a volume mixing ratio) of compound  $i$ , respectively.

A limit of detection (LOD) states the smallest detectable concentration and is conventionally defined by the noise level  $\sigma$  (typically in V) and the sensitivity  $m$  (typically in V/ppm) of the system

$$\text{LOD} = \frac{3\sigma}{m} = \frac{3\sigma c}{S - S_B} = \frac{3c}{\text{SNR}}, \quad (2.4)$$

where the factor three sets a confidence level to 99.7% [76]. The noise level can be estimated from the standard deviation of the temporal or spectral signal. The sensitivity is evaluated from a calibration measurement and can be written as the ratio between the true analyte signal  $S - S_B$  and the concentration, which enables reformulation of the equation using the signal-to-noise ratio (SNR) of the measurement. The true analyte signal is the recorded analyte signal  $S$  subtracted by a background contribution  $S_B$  persistent in a blank measurement. As detecting lower concentrations is often preferable, different absorption spectroscopy techniques have been developed to increase the analyte signal and to decrease the noise level and the blank signal.

## 2.3 Absorption spectroscopy techniques

Absorption spectroscopy techniques record the amount of absorbed radiation within a sample medium at a certain wavelength(s) preferably in the mid-IR region where the strongest fundamental vibrational transitions are located. The majority of the techniques monitor the decrease of optical power with a direct relation to the properties of the medium through Eq. 2.2 and Eq. 2.3, photoacoustic spectroscopy being

the most important exception discussed not until the next chapter. One of the simplest and the most popular attenuation-based methods requiring only a suitable light source and a photodetector is **tunable diode laser absorption spectroscopy (TDLAS)** [30]. The technique utilizes a narrow emission linewidth of a semiconductor laser, which is tuned on a single ro-vibrational transition of the target molecule [77]. Compact diode lasers are nowadays available for nearly any wavelength between the visible and the mid-IR region, and electrical control of the emission wavelength enables wavelength modulation [78]. In this different implementation of TDLAS, a significant noise reduction and thus lower detection limits are achieved by modulating the wavelength of the laser at a high frequency around the transition and demodulating the detected signal often at the second harmonic frequency [79]. The selectivity and multi-species detection of a conventional system can be improved with spectrally tunable sources such as an external-cavity diode laser or an optical parametric oscillator (OPO) [80].

Direct absorption spectroscopy (DAS) can also be implemented with broadband light sources such as light emitting diodes (LEDs) and thermal emitters, which take advantage of entire absorption bands of molecules [30]. **Non-dispersive infrared (NDIR)** sensors employ optical filters to create a reference (no absorption) and an active (absorption) channel, whose optical powers are then compared [81]. Relatively high selectivity can be achieved by a proper selection of filters, and additional active channels enable multi-species detection. For example, a tunable Fabry-Perot filter increases the selectivity and flexibility of the sensor significantly [82]. Although the footprint of NDIR sensors can be very small, the selectivity and sensitivity is defeated by TDLAS. The selectivity of broadband techniques can be significantly improved with a dispersive component such as a grating, which allows wavelength scanning or direct broadband detection when employed with a sensor array [30].

Fast and cost-effective detection of multiple wavelengths with high spectral resolution is provided by **Fourier transform spectroscopy (FTS)** [45], whose operation principle is described in more detailed in Chapter 4. In contrast to the conventional broadband technique with spectral scanning, in FTS the broadband radiation is detected in the time domain rather than in the spectral domain. The temporally varying radiation is only detectable when strongly down-converting the optical frequencies for example using a Michelson interferometer. The spectral resolution is straightforwardly tuned by changing the maximum optical path difference, and thus

FTS systems range from low-resolution field devices to high-resolution laboratory instruments [83, 84]. The compromise between sufficient spectral resolution and a compact size can be improved by clever interferometer designs [85], or electro-optic materials [86], for example. Furthermore, the interferometer can be replaced with a dispersive material such as an optical fiber, which separates in time the spectral components of pulsed light [87]. As a clarification, one should note that in the literature an FTS system with a thermal light source is generally referred to as a Fourier transform infrared (FTIR) spectrometer or simply an FTIR.

The sensitivity of all the aforementioned techniques can be enhanced by increasing the optical (absorption) path length [30], which leads to stronger attenuation of light in an unchanged gas medium (see Eq. 2.2). The strategy for enhancing the path length depends on the gas cell configuration, and in open path systems for example the path length is inherently long. In traditional closed or open gas cells, the optical path length enhancement is implemented with various mirror designs [30], which can be classified into multipass cells and (resonant) cavities although the terminology in the literature is mixed. In a multipass cell, the light beam propagates on a well-defined path between the mirrors creating spot patterns at the reflectors with no overlap. The most commonly used design is a Herriott cell, where a typically circular spot pattern provides up to two orders of magnitude optical path enhancement [88, 89]. An optical cavity consists of highly reflective mirrors forming a standing wave for the radiation. Compared with the multipass cells, cavities are typically less robust, currently poorly available for broadband mid-IR operation and often require a light source with high spatial coherence, but on the other hand they are the basis of the most sensitive gas sensing methods available with optical path lengths reaching kilometers [30, 90]. A common technique is **cavity ring-down spectroscopy**, where the decay constant of a light pulse in the cavity is recorded [90]. Another noteworthy approach is **noise immune cavity-enhanced optical heterodyne spectroscopy**, which combines cavity and wavelength modulation techniques [91].

Traditional broadband light sources are inherently spatially incoherent and therefore not favorable for cavity-enhanced techniques or high-resolution FTS with decent sensitivity. However, during the last few years new light sources combining the high power spectral density and directionality of lasers and the large spectral bandwidth of thermal sources have been increasingly applied to spectroscopy [53, 80, 92]. Such unique emitters are supercontinuum and frequency comb light sources, which



enable more sensitive multi-species detection with the aforementioned optical techniques. For example, both sources can relatively easily be coupled into a multipass cell or a cavity, often followed by a grating or a high resolution FTS instrument [46, 51, 52, 93–98]. Furthermore, frequency combs have enabled a completely new spectroscopic method, **dual-comb spectroscopy (DCS)**, which is essentially FTS without a separate down-converting element. In DCS, two stabilized and slightly frequency shifted frequency combs overlap spatially generating a down-converted comb typically in the radio frequencies (RFs) easily detectable with a single photodetector [99]. Most importantly, the frequency separation (i.e., the repetition rate in pulsed combs) of the two combs must be different determining the frequency separation of the RF comb, while the difference in the offset frequency sets the spectral location of the RF comb. By introducing a sample to the beam path of one of the combs, for example, absorption features can be recovered from the RF comb, enabling extremely fast, high resolution and high sensitivity broadband measurement.

## 2.4 Broadband light sources

A light source is considered spectrally broadband when its spectrum covers a wide range of wavelengths, although a clear limit for the spectral bandwidth is not established. Traditional broadband IR sources are heated elements such as the Sun or a light bulb, whose temperature-dependent spectrum follows the Planck’s black body radiation law. For reasonable temperatures below 3000 K, the spectrum mostly covers the IR region, and higher temperatures both increase the overall power spectral density and shift the spectrum towards visible light as illustrated by the Sun [72]. Despite omnidirectional emission with no spatial coherence, thermal emitters are widely used in NDIR sensors and FTS due to their small footprint and a wide spectrum [30, 53]. LEDs are a strong competitor for thermal emitters especially in NDIR sensors due to their more efficient distribution of optical power on the targeted absorption bands, however still suffering from poor spatial coherence [30, 100].

Supercontinuum (SC) light sources are unique emitters generated by injecting laser radiation into a medium where new frequencies are created through complex interplay of light-matter interactions [55]. These interactions can be divided into linear and nonlinear depending on the relation between the electric field and material polarization [101]. Linear processes such as dispersion (wavelength-dependent

phase velocity of light) are generally significantly stronger compared to nonlinear effects that are only notable with strong electric fields. The simplest second-order nonlinear processes are the generation of sum and difference frequencies from two initial optical fields, the latter process being a popular approach to convert near-IR radiation into mid-IR. Four-wave mixing is another fundamental process generating one or two frequencies from two or three initial frequencies. In the degenerate case, two optical waves at the same frequency produce a pair of sidebands symmetrically around the pump frequency. With no initial seeding, the sidebands are created from noise at frequencies that satisfy the phase-matching condition. The time-domain description of this process is also known as modulation instability. The most prominent third-order process is the optical Kerr effect that describes the dependence of refractive index on the light intensity. As an example of many possible processes, Kerr effect creates a phase shift in a propagating optical pulse and produces new frequencies around the original frequency. In the anomalous dispersion regime, self-phase modulation and dispersion may compensate each other creating an optical soliton whose spectrum remains constant or changes periodically. These and other nonlinear processes are described in more detail elsewhere [55, 101].

SC generation is especially beneficial in optical fibers due to the long interaction length enhancing light-matter interactions, spatially controlled output, and the freedom to control the broadening by tailoring the dispersion profile of the fiber [102]. The material of the optical fiber limits the maximum spectral coverage when properly pumped, current options ranging from standard silica in the visible and near-IR to fluoride and chalcogenide fibers in the mid-IR [53]. Besides material properties (transmission, dispersion, nonlinearity), SC generation depends on the characteristics of the pump (peak power, pumping wavelength, pulse duration, polarization). It follows that SC generation can coarsely be categorized into four regimes depending on the duration of the pump pulse (short/long pulses) and the pumping wavelength with respect to the dispersion profile of the fiber (normal/anomalous group velocity dispersion) [103]. The impact of different nonlinear effects varies between these regions, which strongly affects the characteristics of the resulting SC in terms of bandwidth and pulse-to-pulse fluctuations. The widest spectra are typically generated through soliton dynamics in the anomalous dispersion regime, where the broadening of long pulses (duration longer than a few picoseconds) is initiated by noise-seeded modulation instability breaking the pulse to several solitons [55]. The

initiation of this process from noise leads to a temporally incoherent SC with large spectral fluctuations between the pulses. Despite this disadvantage, fiber-based SC sources pumped with long pulses in the anomalous dispersion regime provide commercially viable options with high spatial coherence, high power spectral density and wide spectral coverage increasingly applied in mid-IR absorption spectroscopy [53, 102]. However, it should be noted that with certain parameters such as pumping with femtosecond pulses in the normal dispersion regime the broadening process is completely coherent from pulse to pulse [55].

An optical frequency comb (OFC) may be considered a coherent SC that consists of narrow equidistant frequency components. A traditional OFC is a femtosecond mode-locked laser, where short pulses result from millions of longitudinal cavity modes with a spacing corresponding to the repetition rate of the laser [56]. Initially applied in ultra-precise atomic clocks, the generation of narrowly spaced OFCs in the mid-IR region has recently increased the number of spectroscopic implementations [80, 92]. In addition to direct mid-IR mode-locked lasers based on thulium-doped silica fibers [104], transition metals doped into chalcogenide hosts [105] or mode-locked quantum cascade lasers (QCLs) [106] and interband cascade lasers (ICLs) [107], mid-IR OFCs can be generated from a mid-IR continuous wave laser via four wave mixing (a Kerr comb) [108] or from a near-IR comb through nonlinear frequency down-conversion (difference frequency generation or optical parametric oscillation) [80]. While Kerr combs and QCL combs have the smallest footprint, frequency-converted OFCs typically provide good frequency stability, narrow frequency spacing and tunability important for high-resolution gas spectroscopy.



### 3 PHOTOACOUSTIC SPECTROSCOPY

Photoacoustic (PA) spectroscopy (PAS) investigates the absorption-induced effect on the gas medium rather than on the incident light that is the focus in conventional absorption spectroscopy techniques [109]. This approach is enabled by the PA effect that converts absorbed radiation into sound waves. The effect was discovered already in 1880 by Alexander Graham Bell when attempting to transmit sound using light [110], but technological deficiency and the lack of quantitative description lead to the oblivion of the phenomenon for decades. The first spectroscopic gas analysis using PAS was reported in 1938 [111], but wider interest in photoacoustics was only sparked by the invention of the laser in the late 1960's [109, 112]. Through decades of methodological and technological development, photoacoustics is currently widely employed both in imaging [113] and spectroscopy of solid, liquid and gas-phase samples [114]. In this chapter, the operation principle of gas-phase PAS is analytically described, different sources of noise are presented and the instrumentation and different PAS techniques are reviewed.

#### 3.1 Operation principle

The operation principle of PAS relies on inducing periodic heating in the gas medium, which produces a sound wave detectable with a microphone. This principle is illustrated with a simple experimental system in Fig. 3.1. The generation of periodic heating requires that the light source's optical power on the probing wavelength varies temporally. This variation is traditionally implemented by modulating the amplitude of the incident radiation either with a pulsed source or with separate modulation that can be both external (e.g., mechanical chopper in Fig. 3.1) or internal (e.g., current modulation in semiconductor lasers). Wavelength modulation can alternatively be employed with certain advantages discussed later. Considering a single-frequency light source amplitude-modulated sinusoidally at a frequency  $f$ ,

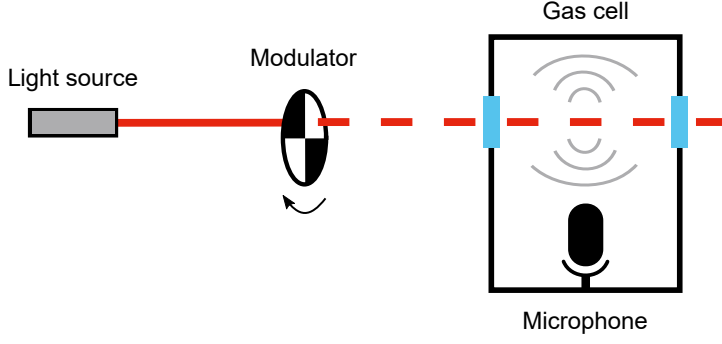


**Figure 3.1** A simple PAS system containing a light source, a mechanical chopper as an amplitude modulator, a gas cell and a microphone. The amplitude of the emission is modulated to inflict periodic absorption of light in the gas medium, which leads to periodic release of heat and periodic pressure changes. The pressure transducer records the created sound waves.

the time-dependent optical power can be written

$$P_0(\nu, t) = P_I(\nu)[1 + \cos(2\pi f t)], \quad (3.1)$$

where  $P_I(\nu)$  denotes the average optical power incident to the gas medium.

Incident radiation excites molecules in the gas medium to ro-vibrational energy levels dictated by the emission wavelength. The de-excitation process in the IR region is predominantly non-radiative leading to local heating of the medium. The released heat energy  $Q(\nu, t)$  is related to the absorbed optical power (acquired from Eq. 2.2) according to

$$\frac{dQ}{dt} = \eta_{nr} = \eta_{nr}[P_0(\nu, t) - P(\nu, t)] = P_0(\nu, t)\alpha(\nu)L\eta_{nr}, \quad (3.2)$$

where  $\eta_{nr}$  describes the efficiency of thermal relaxation that depends on the probed transition and the gas matrix [115]. In PAS,  $\eta_{nr}$  can be considered to also depend on the modulation period of the radiation, because the typical combination of slow relaxation and fast modulation leads to poor overall relaxation efficiency [116]. At low modulation frequencies ( $f < 1000$  Hz), complete thermal relaxation can reasonably be expected for many molecules especially in ambient air, although some exceptions have been observed [117, 118]. Assuming a constant volume of the medium consisting of diatomic molecules, the relation between the released heat energy and the

following change in temperature is

$$dQ = C_v dT = \frac{5}{2} N A l k dT, \quad (3.3)$$

where  $C_v$  is the heat capacity of the medium,  $A$  and  $l$  are the cross sectional area and the length of the gas cell (assuming the light beam fills the gas cell perfectly), and  $k$  is the Boltzmann constant.

A substitution of Eq. 3.1 and Eq. 3.3 to Eq. 3.2 yields a differential equation

$$\frac{dT}{dt} = \frac{1}{C_v} \frac{dQ}{dt} = \frac{2P_I(\nu)\alpha(\nu)L\eta_{nr}}{5NAIk} [1 + \cos(2\pi f t)] \quad (3.4)$$

with a solution

$$T(t) = T_0 + \frac{2P_I(\nu)\alpha(\nu)L\eta_{nr}}{5NAIk} \left[ t + \frac{\sin(2\pi f t)}{2\pi f} \right], \quad (3.5)$$

where  $T_0$  denotes ambient temperature. The second term describes a monotonically increasing temperature, which in practice eventually balances out with heat conduction to the walls of the gas cell. This heat sinking could be included in the treatment [119], but for simplicity the second term in Eq. 3.5 is simply neglected here, resulting in a periodically changing temperature with an amplitude  $\Delta T$  around the ambient temperature

$$T(t) = T_0 + \frac{P_I(\nu)\alpha(\nu)L\eta_{nr}}{5\pi f N A I k} \sin(2\pi f t) = T_0 + \Delta T \sin(2\pi f t). \quad (3.6)$$

Inverse proportionality with the modulation frequency is based on an assumption that the temperature accumulates in the gas cell for a sufficiently long time compared to the modulation period. However, fast relaxation and heat conduction together with a nearby heat sink will break this assumption, and the amplitude of the temperature variation may even be independent on the modulation frequency.

Pressure follows the temperature according to the ideal gas law. By defining the optical enhancement factor  $F = L/l$  (the effective number of beam passes through the gas cell) and including all quantities related to the heat transfer in the cell constant

$C_{\text{cell}}(f)$ , the pressure change is

$$\Delta p = Nk\Delta T = \frac{P_I(\nu)\alpha(\nu)\eta_{\text{nr}}F}{5\pi f A} = P_I(\nu)\alpha(\nu)FC_{\text{cell}}(f). \quad (3.7)$$

By considering the generation of sound waves more carefully, many other effects could be included in the cell response, such as the quality factor of the resonator and the damping of high frequencies due to a finite thermal relaxation process and heat transfer. Some of these details will be discussed later.

Pressure variations induced through the periodic absorption of incident radiation by gas molecules and the cyclic release of heat are converted into an electrical signal using a pressure transducer, more familiarly a microphone. For a microphone with a frequency-dependent sensitivity  $S_m(f)$ , the sinusoidal PA signal from a monochromatic source is

$$S(t) = S_m(f)\Delta p \sin(2\pi f t + \delta') = S_0(f) \sin(2\pi f t + \delta'), \quad (3.8)$$

where a phase shift  $\delta'$  is added due to the pressure wave propagation from the heat source to the microphone. The amplitude of the PA signal is then

$$S_0(f) = P_I(\nu)\alpha(\nu)FC_{\text{cell}}(f)S_m(f), \quad (3.9)$$

which conveniently reveals the main advantages of PAS. The amplitude is directly proportional to the absorption cross section, which makes the technique emissive contrary to the attenuation-based approaches. Moreover, the cell response and the microphone sensitivity depend only on the frequencies of the sound waves and thus all (optical) wavelengths are detected equally well. Finally, the direct proportionality to the optical power provides an efficient approach to enhance the sensitivity.

## 3.2 Noise sources

There are five conventional sources of noise in PAS: acoustic noise, acceleration noise, electric noise, thermal noise and noise arising from a gas flow [109, 112, 119]. However, noise from the gas flow is only present in flow-through systems with turbulent flow [112]. External noise contributions from acoustic waves (acoustic noise) and mechanical vibrations (acceleration noise) present the downside of operating



with certain microphones, but these noise sources can be largely eliminated with proper instrumentation. When these three noise sources are eliminated, electric noise from the microphone (or its amplifier) or thermal noise becomes dominant. Thermal noise is the fundamental noise limit in PAS originating from Brownian motion in the gas medium, which results in random pressure fluctuations [109].

In addition to these five sources of noise, intensity fluctuations of the light source introduce an additional noise contribution. Because its origin is less intuitive compared to other noise sources and it is typically neglected in the literature, the source-induced noise is discussed in more detail here. To account for the temporal fluctuations in the exciting optical power, optical power is now described by its average value  $P_I(\nu)$  and the temporal change  $\Delta P(\nu, t)$

$$P_I(\nu) \rightarrow P_I(\nu) + \Delta P(\nu, t), \quad (3.10)$$

which leads to two different effects depending on the time scale. Considering time scales around the measurement time, power fluctuations are directly reflected in the PA amplitude at the specific wavenumber via Eq. 3.9, which leads to amplitude variations on the corresponding frequency. However, power variations on shorter time scales lead to a very different effect creating noise across the entire detection bandwidth.

To study this, the differential equation 3.4 is solved again, now with the time-dependent incident power resulting in

$$T(\nu, t) = T_0 + \Delta T \sin(2\pi f t) + \frac{\alpha(\nu)L\eta_{\text{nr}}}{C_\nu} \int \Delta P(\nu, t) [1 + \cos(2\pi f t)] dt. \quad (3.11)$$

In addition to the temperature change from a stable light source (second term), the temperature at any given moment of time  $t$  includes a contribution from the cumulative temperature change of the power variations (third term). This accumulation is valid in timescales dictated by the relaxation dynamics and thermal diffusion. When considering a continuous wave or a quasi continuous wave (pulse period shorter than the time constants) light source, these slow thermal processes damp the fast power fluctuations and the noise from the light source is low-pass filtered. These low-pass filtered intensity fluctuations add noise, that is new frequencies, to the ideal sinusoidal temperature trace.

Denoting the filtered power noise as  $P_N(\nu, t)$  and its frequency content as

$P_N(\nu, f)$ , the PA spectrum from a single wavenumber component is modified to

$$S_0(f) \rightarrow S_0(f) + P_N(\nu, f)\alpha(\nu)F\hat{C}_{\text{cell}}S_m(f), \quad (3.12)$$

where  $\hat{C}_{\text{cell}}$  is the cell constant for the noise which, most importantly, does not depend on the modulation frequency. In addition to the amplitude  $S_0(f)$  (generated from a stable source, Eq. 3.9) corresponding to wavenumber  $\nu$ , intensity noise at this wavenumber generates noise across the acoustic spectrum. Defining  $\sigma_{\text{LS}}(\nu)$  as the standard deviation (std) of the amplitude variations in the PA spectrum, the spectral noise induced by the intensity fluctuations of the light source at wavenumber  $\nu$  is

$$\begin{aligned} \sigma_{\text{LS}}(\nu) &= \text{std}[P_N(\nu, f)]\alpha(\nu)F\hat{C}_{\text{cell}}S_m(f) \\ &\propto \text{RIN}(\nu)P_I(\nu)\alpha(\nu)F\hat{C}_{\text{cell}}S_m(f), \end{aligned} \quad (3.13)$$

because  $\text{std}[P_N(\nu, f)] \propto \text{std}[P_N(\nu, t)] \propto \text{std}[\Delta P(\nu, t)]$  and the relative intensity noise (RIN) is defined as  $\text{RIN}(\nu) = \text{std}[\Delta P(\nu, t)]/P_I(\nu)$  [**Publication III**].

The main implication of Eq. 3.13 is that the noise induced by the light source is not constant but depends on the absorbed radiation inside the gas cell. It follows that the noise depends on the gas concentrations (Eq. 2.3), which leads to a unique relation between the concentration and the SNR of the spectrum. As the PA amplitude is also directly proportional to the concentration (Eq. 3.9), there exists a threshold concentration after which the source-induced noise becomes dominant and the SNR independent on the concentration [120].

### 3.3 Instrumentation

Similar to conventional absorption spectroscopy, a dominant drive in the development of PAS systems has been the ability to detect lower and lower concentrations of different gas species. In addition to enhancing the amplitude through factors shown in Eq. 3.8 and eliminating the noise sources presented previously, a coherent background amplitude from the absorption of light by the cell windows must be considered. Carbon dioxide lasers have historically been popular light sources in PAS due to their high mid-IR output power, but now they are largely replaced by diode lasers and OPOs with wider spectral coverage and tunability [114, 121]. With these

lasers, wavelength modulation is an especially useful approach allowing the separation of the coherent background signal (at frequency  $f$ ) from the molecular signal (at frequency  $2f$ ) [114]. As a result, the most sensitive PAS systems have implemented wavelength modulation of a mid-IR QCL or an OPO to yield ppt-level detection limits [44, 122]. Moreover, multipass configurations and cavities can be implemented to further amplify the signal [123–128].

Besides optical enhancement, the induced acoustic wave can be amplified by maximizing the cell constant. Acoustically resonant cells are traditionally employed by matching the modulation frequency and the acoustic frequency of the resonator [109]. This leads to a standing acoustic wave enhancing the acoustic signal typically two but up to four orders of magnitude [114, 129]. The best benefit is achieved in combination with wavelength modulation by adjusting the second harmonic frequency on the resonance frequency of the resonator. Despite the absence of acoustic amplification, non-resonant gas cells are beneficial in many applications as the dependence of the resonance frequency on environmental conditions needs no consideration, and the dimensions of the gas cell can be freely chosen to maximize the PA signal within a compact system [130]. In general, the cell constant is inversely proportional to the cross sectional area of the gas cell (Eq. 3.7), and thus narrow cylindrical cells with down to sub-milliliter volumes are advantageous [44, 119, 126, 131–134].

Many solutions have been reported to overcome the coherent signal from the window absorption when wavelength modulation is not feasible. Acoustic buffer volumes or open gas cells (no windows) are typical for acoustically resonant operation, while differential cells can be employed to both resonant and non-resonant systems [121, 135]. A typical differential approach has two resonator tubes placed side by side in the gas cell with both resonators equipped with individual microphones [136–138]. When light is directed through only one of the resonators, the difference signal from the microphones eliminates the window signal among all other coherent noise (external noise and flow noise) present in both resonators. Many other differential designs have also been demonstrated with varying properties [135, 139–142], including an implementation with wavelength modulation [143].

Numerous microphones have been developed during the past 40 years to replace a conventional capacitive pressure transducer, which has a circular membrane that stretches out radially due to the pressure variations. Besides a flexible diaphragm or

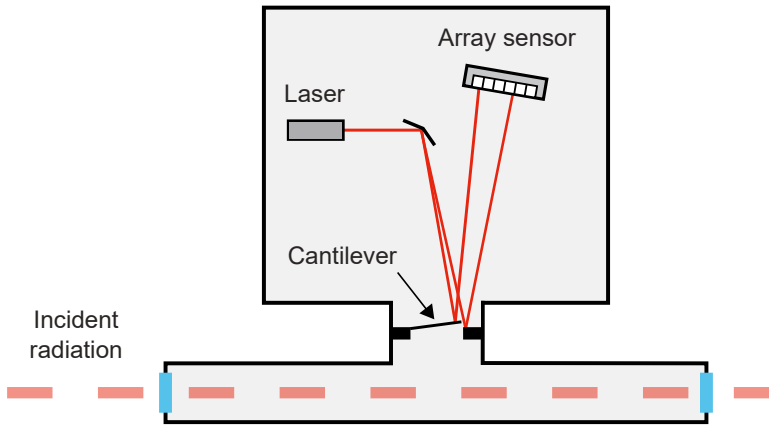


**Figure 3.2** A typical design of the cantilever pressure transducer with an interferometric readout. Pressure waves generated by modulated radiation and periodic absorption displace a thin cantilever. In the interferometer, one laser beam is directed on the cantilever while the other beam reflects from the frame of the cantilever. The spatial interference pattern between the laser beams recorded with an array photodetector reveals the displacement of the cantilever.

a film [144, 145], sensing elements such as quartz tuning forks (QTFs) [146, 147], cantilevers [148–150] and optical fibers [151] have been reported with typical detection principles based on the piezoelectric effect [146, 148, 152], laser beam deflection [145] or interferometry [144, 147, 149, 151]. Despite the type of microphone employed, phase-sensitive lock-in techniques are generally used to amplify the PA signal [114]. Current state-of-the-art pressure transducers are piezoelectric QTFs and interferometrically read silicon cantilevers, which both utilize bending of the sensing element instead of stretching enabling superior performance compared to the conventional design [114]. As a result, both microphones have been demonstrated to provide ppt-level detection limits [44, 122]. With the QTF, incident light is focused between the prongs where the PA effect leads to a resonant symmetric vibration, thus eliminating ambient noise that produces a piezoelectrically inactive antisymmetric vibration [153]. Cantilever microphone is a thin slab of typically silicon, which moves similar to a saloon door due to the pressure variations [154]. Exceptionally high-performance detection of the cantilever movement is provided by a Michelson-type interferometer and an array detector illustrated in Fig. 3.2.

Spectrally broadband PAS has been implemented with a tunable laser, an array of lasers or LEDs [155, 156], and with a broadband light source along with optical filters [57–59, 157] or a grating [158]. However, all these approaches acquire

spectral information sequentially. Although parallel dual-frequency operation has been reported with the QTF [159], multi-frequency detection in general necessitates a broadband frequency response from the microphone. Moreover, acoustically resonant broadband operation requires a carefully designed system such as several separate resonators [160]. The situation with non-resonant gas cells is significantly simpler, thus they can effortlessly be employed in the PA implementation of FTS [60–67].



## 4 FOURIER TRANSFORM PHOTOACOUSTIC SPECTROSCOPY

Fourier transform photoacoustic spectroscopy (FT-PAS) may be considered FTS with photoacoustic detection or a broadband implementation of PAS depending on the viewpoint. Nevertheless, the technique is unique for the acquisition of broad absorption spectra with good spectral resolution in a reasonable time and in a small sample volume. FT-PAS is traditionally applied for solid and liquid samples with an additional benefit of depth profiling [62, 161–167], but numerous gas-phase implementations have also been reported [60–67]. In this chapter, the operation principle of FT-PAS is introduced, the experimental devices from **Publications I–V** are summarized and the noise characteristics of the technique are discussed.

### 4.1 Operation principle

The operation of FT-PAS relies on the parallel down-conversion and the concurrent wavelength-dependent amplitude modulation of incident broadband light, and the simultaneous detection of the resulting numerous pressure waves using a microphone with a wide frequency response. A typical experimental system and the operation principle of FT-PAS are illustrated in Fig. 4.1. The analytical treatment of FT-PAS begins by considering the propagation of a collimated broadband source with an intensity spectrum  $I_0(\nu)$  through a scanning Michelson interferometer illustrated in Fig. 4.1a. A beamsplitter divides the initial beam between two arms, and by translating one of the mirrors a phase delay  $\delta(\nu) = 2\pi x/\lambda = 2\pi\nu x$  is introduced to the corresponding beam [168]. This phase delay depends on the optical path difference (OPD)  $x$  between the interferometer arms and on the wavenumber. The beamsplitter combines the beams at the output, resulting in a total intensity that depends on

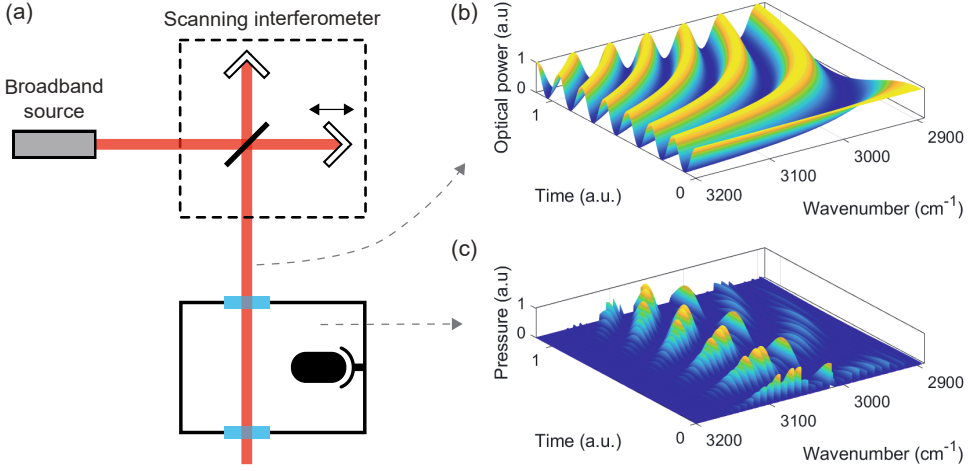


**Figure 4.1** An illustration of the operation principle of FT-PAS. (a) A schematic experimental setup, where a scanning interferometer down-converts the radiation from a broadband light source to frequencies which are detectable with a microphone after the PA effect. (b) Simulated wavenumber-dependent intensity modulation of a light source with a rectangular spectrum. The relative frequencies are exaggerated. (c) Simulated pressure trace when probing the fundamental asymmetric stretch band of methane with the modulated light source in (b).

the OPD. For a single spectral component, this intensity is

$$I(\nu, x) = \frac{I_0(\nu)}{2} (1 + \cos[\delta(\nu)]) = \frac{I_0(\nu)}{2} [1 + \cos(2\pi\nu x)], \quad (4.1)$$

where the factor two results from the 50% throughput of the Michelson interferometer. The intensity maxima occur at intervals of one wavelength,  $x = \lambda = 1/\nu$ , and thus the modulation frequency  $f$  (in Hz) is

$$f = V_{\text{OPD}}\nu, \quad (4.2)$$

where  $V_{\text{OPD}}$  is the OPD scan velocity (in cm/s). The physical velocity of the mirror is usually two or four times slower than  $V_{\text{OPD}}$  depending on the configuration of the interferometer.

Each spectral element of the light source corresponds to a unique modulation frequency clearly seen in Eq. 4.2. This is illustrated in Fig. 4.1b, where the source spectrum is flat between 2900–3200 cm<sup>-1</sup> and the differences in the modulation frequencies are exaggerated. Changing intensities to optical powers (by integrating the spatial intensity distribution over the beam area) and transitioning into time domain



(using  $x = V_{\text{OPD}}t$  and Eq. 4.2), a temporally varying optical power is found

$$P(\nu, t) = \frac{P_0(\nu)}{2} [1 + \cos(2\pi f t)] = P_1(\nu) [1 + \cos(2\pi f t)], \quad (4.3)$$

similar to Eq. 3.1. Now considering again the broadband nature of the light source, each spectral component of the source experiences the phenomenon described by Eq. 4.3. As a result, all components interfere with each other and the total time-dependent optical power  $P(t)$  is acquired by integrating Eq. 4.3 over the spectrum of the light source.

Each absorbed spectral component of the modulated light will generate a pressure wave in the gas cell, whose frequency and amplitude (mostly via absorption cross section) depends on the wavenumber. The temporally varying pressure for different spectral components is illustrated in Fig. 4.1c for the asymmetric C–H stretch band of  $\text{CH}_4$  using the exaggerated modulation frequencies from Fig. 4.1b. At the beginning of the simulation, all spectral elements interfere constructively and the spectrum of  $\text{CH}_4$  is visible around  $t = 0$  (compare with Fig. 2.3). Following the procedure in Chapter 3, the total PA signal recorded with the microphone is

$$S(t) = \int_0^\infty S_0(f) \sin(2\pi f_\nu t + \delta') df. \quad (4.4)$$

Artificially defining  $S_0(-f) = S_0(f)$ , the PA spectrum  $S_0(f)$  is the Fourier transform of the interferogram,  $S_0(f) = \mathcal{F}\{S(t)\}$ , which can be transferred to the optical domain using Eq. 4.2.

In the ideal case of scanning the interferometer infinitely long, the PA spectrum consists of narrow lines whose width is dictated by the physical broadening mechanisms. In reality, the maximum OPD  $x_{\text{max}}$  of the interferogram often results in further spectral broadening of these lines. To take spectral resolution of the system into account, the formalism is transformed from  $S(f, t)$  back to  $S(\nu, x)$ . A limited OPD translates into truncation of the interferogram signal, and thus the truncation by a simple boxcar function  $\Pi(x)$  results in a modified spectrum

$$S'_0(\nu) = \mathcal{F}\{\Pi(x)S_0(x)\} = 2x_{\text{max}} \text{sinc}(2\pi\nu x_{\text{max}}) * S_0(\nu), \quad (4.5)$$

where operator  $*$  denotes convolution [168]. The lines are broadened by a sinc-

function, whose width sets the spectral resolution  $\Delta\nu$ , typically defined as [73]

$$\Delta\nu = \frac{1}{x_{\max}}. \quad (4.6)$$

Besides the limited delay range, the cross sectional area of the collimated beam also leads to the broadening of the spectral lines [168]. However, this effect is mainly relevant for thermal emitters and other spatially incoherent light sources, in which case separate apertures are used for high-resolution measurements.

The sinc-function in Fig. 4.5 causes artifacts to the spectrum [168], which can be reduced by apodization at the expense of spectral resolution [169]. By introducing the instrument lineshape function  $\Lambda(\nu)$  that is the Fourier transform of the apodization function, the PA spectrum finds its final general form

$$S'_0(\nu) = \Lambda(\nu) * S_0(\nu) \approx [P_I(\nu) F C_{\text{cell}}(f) S_m(f)] \times [\Lambda(\nu) * \alpha(\nu)]. \quad (4.7)$$

To obtain a spectrum that is proportional to the convolved absorption coefficient with the least post-processing, all other factors in Eq. 4.7 should be as flat as possible. Therefore, both the gas cell and the microphone should be operated off-resonance. Capacitive microphones and optically read cantilevers have been demonstrated to have a sufficiently flat frequency response for broadband detection [62, 68]. The optical enhancement factor and the optical power are not always flat but can be relatively easily corrected for.

## 4.2 Experimental setups

Four different FT-PAS setups were constructed and tested in this thesis. These systems consist of three fundamentally different light sources, three scanning interferometers (SIs) and three photoacoustic analysers (PAAs) that include a gas cell, a cantilever microphone and an optical enhancement system. The main properties and differences of these subsystems are summarized in Table 4.1 with more details found in the corresponding publications.

The three light sources, a thermal emitter, a SC and an OFC have very different characteristics starting from the footprint to the emitted power spectral density (PSD) spectra shown in Fig. 4.2. The SC and OFC sources are home-built (in

**Table 4.1** Parameters and properties of the light sources, scanning interferometers (SIs) and photoacoustic analysers (PAAs, including the gas cell, cantilever microphone and optical enhancement system) used in this thesis. The first five quantities of the light sources describe the pump and the last four the entire source. The PSD is given at  $3000\text{ cm}^{-1}$ . CMOS stands for complementary metal-oxide-semiconductor.

Light source	Thermal	SC	OFC
Pump wavelength ( $\mu\text{m}$ )	-	1.55	1.95
Pulse peak power (kW)	-	10	200
Pulse duration (ps)	-	600	0.09
Repetition rate (MHz)	-	0.07–0.4	125
PSD ( $\mu\text{W}/\text{cm}^{-1}$ )	$\sim 10$	$\sim 70$	70
Spectral coverage ( $\mu\text{m}$ )	2–20	1–3.5	3.2–3.5
Spatially coherent	No	Yes	Yes
Temporally coherent	No	No	Yes
Footprint	Small	Moderate	Large
Publication	I	I, III, IV, V	II
Scanning interferometer	SI1	SI2	SI3
Spectral resolution ( $\text{cm}^{-1}$ )	$>1$	$>0.0037$	13
OPD scan velocity (mm/s)	1	Tunable	2
Delay type	Linear	Linear	Rotational
Light source monitoring	No	Yes	No
Size ( $\text{m} \times \text{m} \times \text{m}$ )	$0.3 \times 0.3 \times 0.2$	$2 \times 1 \times 0.2$	$0.2 \times 0.2 \times 0.1$
Publication	I, IV, V	II	III
Photoacoustic analyser	PAA1	PAA2	PAA3
Gas cell length (cm)	10	9.5	5
Gas cell diameter (mm)	4.5	4	4
Total sample volume ( $\text{cm}^3$ )	8	7	-
Optical enhancement factor	2	1.8 or 6.3	2
Cantilever dimensions ( $\text{mm}^3$ )	$6 \times 1.5 \times 0.01$	$5 \times 1.2 \times 0.01$	-
Number of cantilevers	One	One	Two
Detector	4 photodiodes	CMOS	CMOS
Publication	I	II, IV, V	III

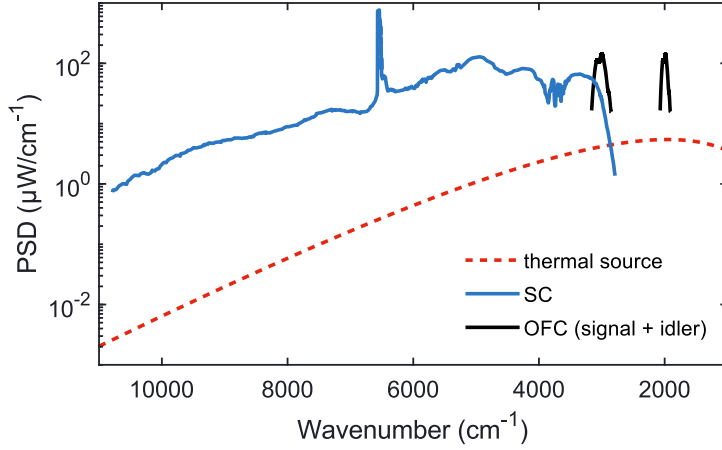


**Figure 4.2** Power spectral density (PSD) spectra of the main light sources used this thesis. Experimentally acquired SC spectrum corresponds to 70 kHz repetition rate with no optical filtering. The OFC signal spectrum (at  $3000 \text{ cm}^{-1}$ ) was measured while the idler spectrum was estimated based on the information in Ref. [170]. One should note that both the idler and signal of the OFC can be tuned a few hundred nanometers. The spectrum of the thermal emitter was calculated from the Planck's law and using experimental information from **Publication I**.

Tampere University and Umeå University respectively [93, 170]) systems with high spatial coherence and similar PSDs around  $3000 \text{ cm}^{-1}$ . The SC source employs a compact erbium-doped fiber laser and two successive optical fibers (silica and fluoride) to achieve extensive spectral broadening on both sides of the pump [93]. The repetition rate of the pump laser is adjustable and changes the pulse energy thus affecting the spectral broadening [**Publication I**]. The default repetition rate was 70 kHz, which results in a spectrum covering  $11000\text{--}2800 \text{ cm}^{-1}$  ( $0.9\text{--}3.6 \text{ nm}$ ) as seen in Fig. 4.2. The broadening process of 0.6 ns pump pulses in noise-seeded, which leads to large pulse-to-pulse intensity fluctuations [**Publication III**]. The OFC on the other hand is temporally very stable as it is based on an OPO pumped with a mode-locked thulium-doped fiber laser [170]. The output consists of two emission spectra (signal and idler) which are narrow ( $\sim 300 \text{ cm}^{-1}$ ) compared to the SC but slightly tunable.

All three amplitude modulators are SIs with different maximum OPDs and delay mechanisms. SI1 and SI2 employ traditional linear delay lines, but the OPD generation in SI2 is twice as efficient. Rotational motion is utilized in SI3 to produce the path difference, which is practical for low-resolution field systems [85]. The obtainable spectral resolutions with these interferometers can be illustrated by considering

the ro-vibrational spectrum of  $\text{CH}_4$  in Fig. 2.3, where the transitions in the P- and R-branches are separated by about  $10 \text{ cm}^{-1}$  with linewidths of about  $0.1 \text{ cm}^{-1}$  (in atmospheric conditions). The transitions in the side branches are clearly resolved with SI1 but not with SI3 [**Publication I**, **Publication III**], and using SI2 the rotational fine structure also in the Q-branch can be resolved even at underpressures [**Publication II**].

The PAAs (excluding external optical enhancement of PAA2) range from an older prototype [64] to a state-of-the-art commercial device (PA201 from Gasera Ltd.) illustrated in Fig. 3.2. The gas cells are small cylinders, which in PAA1 and PAA3 are closed from one end and gold coated to yield an optical enhancement factor of two. PAA2 on the other hand has windows on both ends of the cell providing more freedom to amplify the optical power with external mirrors. For an external mirror configuration, the wavenumber-dependent optical enhancement factor is

$$F(\nu) = \frac{L}{l} = \sum_{i=1}^{N_p} [T_w(\nu)]^{2i-1} [R_m(\nu)]^{i-1}, \quad (4.8)$$

where  $N_p$  is the number of passes,  $T_w(\nu)$  is the window transmittance and  $R_m(\nu)$  is the mirror reflectance. The importance of minimizing optical losses especially for systems with a large number of passes is illustrated in Fig. 4.3a, which is calculated using Eq. 4.8 and where the losses are given per single pass  $(1 - T_w^2 R_m)$ . PAA2 was employed with two different multipass configurations including a simple two-pass design [**Publication II**] and a more efficient ten-pass Herriott cell [**Publication IV**, **Publication V**]. The optical enhancement of the Herriott cell and the corresponding simulated intensity patterns at the mirrors are shown in Fig. 4.3b,c respectively.

The PAAs employ several tricks to eliminate external noise sources. Acoustic noise is efficiently attenuated by sealing the cell tightly with windows and O-rings. Acceleration noise (external mechanical vibrations) in the vertical direction are eliminated by orienting the cantilever plane vertically, and further damping is provided by vibration isolated plates, a differential microphone design (PAA3) [157], and a balance volume which compensates the vibration-induced bending of the cantilever [119]. The balance volume raises the total sample volumes of the systems to a few milliliters. Finally, all systems were placed on a vibration isolated optical table for further reduction of acceleration noise.

The majority of the experiments in this work were carried out approximately in

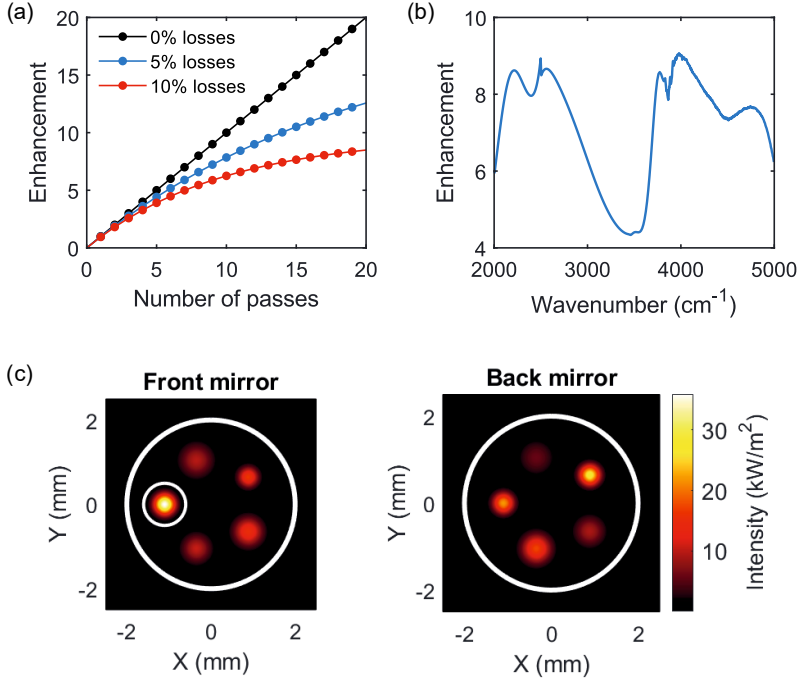


**Figure 4.3** Design and modelling of the multipass system. (a) Theoretical multipass enhancement for three different losses per pass, showing the futility of a large number of passes for a lossy system. (b) Theoretical multipass enhancement for ten beam passes based on the wavenumber-dependent losses of the system. (c) Simulated intensity pattern at both mirrors of the multipass cell for ten beam passes. The outer white ring represents the cross section of the gas cell, and the inner ring illustrates the aperture guiding light inside the cell.

atmospheric conditions. In general, choosing the total pressure inside the gas cell is crucial in PAS as it affects the performance through molecular absorption (pressure broadening), sensitivity of the microphone, and the vibrational-translational relaxation rate of the target transition [114]. The latter two are characteristic specifically for PAS, and their importance varies between different systems and especially microphones. Most importantly, the total pressure affects the frequency and the quality of the pressure transducers' resonance [116, 119]. Cantilever microphone is operated off-resonance and thus the effect is small compared to a QTF, for example. Relaxation rates and their pressure dependence is most relevant when the modulation frequency is high compared to the relaxation rates, which is the case for example in QEPAS systems [116]. However, in CEPAS the modulation frequencies are low compared to the relaxation rates, and the effect may be neglected. The total pressure inside the cell, typically ranging 0.3–1.1 bar, is controlled by built-in gas exchange

systems of the PAAs. Moreover, two of the analysers (PAA1 and PAA2) contain thermostats to heat up the cell up to 50 °C. The temperature of the gas medium also affects the sensitivity of the microphone (this effect is small for the cantilever) and plays a crucial role in acoustically resonant systems as the speed of sound and therefore the resonance frequency are temperature dependent [171]. One should also note that the temperature affects the adsorption-desorption process on the cell walls, which is important when handling volatile substances.

### 4.3 Noise characteristics

The main noise sources in FT-PAS are electric noise, thermal noise and the intensity noise of the light source. Electric noise is negligible when considering the cantilever microphone [119], and the total noise of the FT-PAS spectrum can then be written

$$\sigma_{\text{tot}} = \sqrt{\sigma_{\text{T}}^2 + \sigma_{\text{LS}}^2}, \quad (4.9)$$

where  $\sigma_{\text{T}}$  is thermal noise and  $\sigma_{\text{LS}}$  is the source-induced noise. The source-induced noise is especially relevant when dealing with pulsed light sources that exhibit large pulse-to-pulse intensity variations. In the broadband approach, each spectral component produces its own noise contribution  $\sigma_{\text{LS}}(\nu)$  according to Eq. 3.13. Assuming these noise components are uncorrelated, the total noise contribution from the light source is

$$\sigma_{\text{LS}} = \sqrt{\int_{\nu_{\min}}^{\nu_{\max}} \sigma_{\text{LS}}^2(\nu) d\nu}, \quad (4.10)$$

where  $\nu_{\min}$  and  $\nu_{\max}$  describe the bandwidth of the light source. In the special case of a single absorbing species,  $\sigma_{\text{LS}}$  is directly proportional to the concentration

$$\sigma_{\text{LS}} \propto \sqrt{\int_{\nu_{\min}}^{\nu_{\max}} [\text{RIN}(\nu)P_{\text{I}}(\nu)\sigma(\nu)c]^2 d\nu} \propto c, \quad (4.11)$$

derived from Eq. 4.10, Eq. 3.13 and Eq. 2.3.

Eq. 4.10 describes the multiplex disadvantage well-known in conventional FTS [172, 173]. All detected spectral components create noise, such that intensity noise at each spectral element produces noise within the entire detection bandwidth. Therefore, light sources with high pulse-to-pulse intensity fluctuations have been reported

to increase the noise level in FTS [46]. FT-PAS introduces a favorable modification to the multiplex disadvantage, as only the absorbed spectral components are detected (in contrast to all spectral components of the light source in FTS). Considering only the source-induced noise, this results in a significant decrease in the noise level [**Publication III**]. In FTS, the source-induced noise is generally eliminated with balanced detection [47, 174] or by limiting the bandwidth of the detected light with spectral filters [46]. Limiting the detection bandwidth is also viable in FT-PAS, where the purpose is to eliminate futile absorption in the gas cell [**Publication III**].

The dependence of the detected noise on the amount of absorption in FT-PAS was characterized by measuring varying concentrations of water ( $\text{H}_2\text{O}$ ) and ethylene ( $\text{C}_2\text{H}_4$ ) [**Publication III**, **Publication IV**]. The noise study for  $\text{C}_2\text{H}_4$  is shown in Fig. 4.4, where the upper plot contains the recorded spectra at three concentrations together with a spectrum of no light entering the gas cell, and the lower plot shows the resulting dependence between the concentration and the noise level with additional concentration values. The experimental data in Fig. 4.4b agrees very well with the fit function  $\sqrt{a^2 + (bx)^2}$  derived from Eq. 4.9 and Eq. 4.11. Moreover, thermal noise estimated from the fit agrees with the value obtained from the background spectrum (no light entering the cell, grey line in Fig. 4.4a).

The behavior seen in Fig. 4.4 has both advantages and disadvantages for the sensor. Fortunately, the source-induced noise does not affect the detection limit, as thermal noise is dominant at low analyte concentrations. However, this only applies when considering a single absorbing species in the cell and its detection limit. More generally, the detection limit of any species is not affected by the source-induced noise from itself, but on the other hand in multi-species samples the detection limit of any species may be deteriorated by other species in the mixture. As a result, the detection of a low concentration of one species and a high concentration of another species is limited.

The dependence of noise on the concentration leads to a unique relation between the concentration and the SNR of the spectrum, which in typical sensors increases with the concentration. Further analysis of the  $\text{C}_2\text{H}_4$  measurement set shown in Fig. 4.4 confirms that the SNR saturates to around 60 at high concentrations as seen in Fig. 4.5. At concentrations above approximately 100 ppm, thermal noise becomes negligible and both the amplitude and noise depend linearly on the concentration. The fit function, adopting the noise relation presented previously and a linear depen-



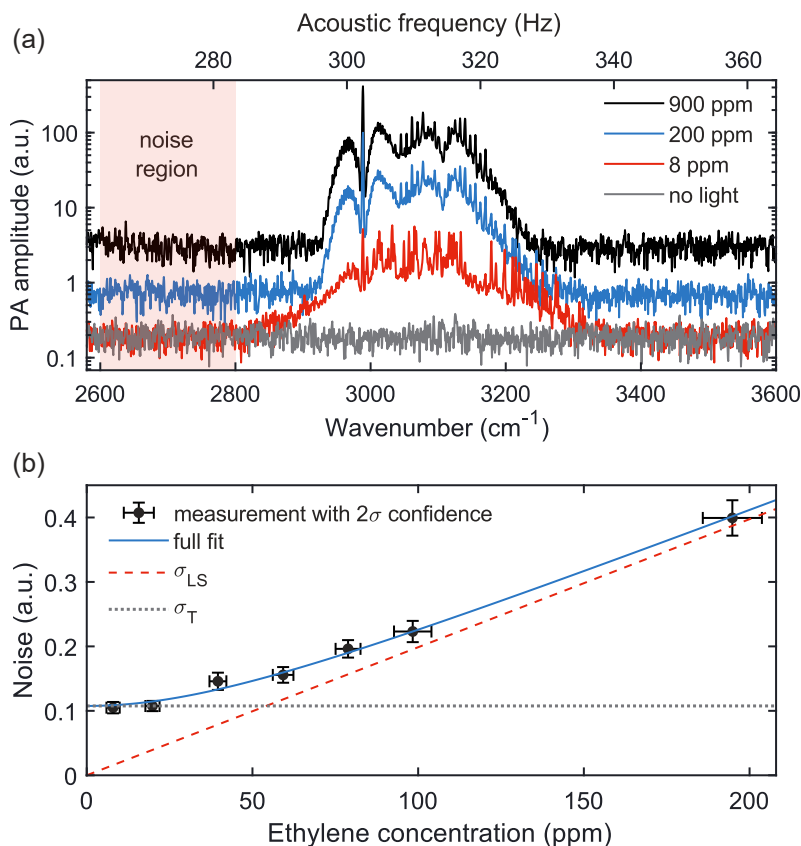


**Figure 4.4** Characterization of FT-PAS noise using  $\text{C}_2\text{H}_4$  at concentrations ranging 8–900 parts-per-million (ppm). (a) Recorded ro-vibrational spectra ( $\Delta\nu = 1 \text{ cm}^{-1}$ , 100 s averaging corresponding to five scans) of the asymmetric C–H stretching of  $\text{C}_2\text{H}_4$  at three concentrations and with no incident light. The spectra are shown in acoustic frequencies (top axis) and the corresponding optical wavenumbers (bottom axis). (b) The noise level as a function of  $\text{C}_2\text{H}_4$  concentration below 200 ppm (in the linear region of the Beer-Lambert law). The noise was calculated from single-scan spectra as the standard deviation of the PA amplitude at 2600–2800  $\text{cm}^{-1}$  (red region) and averaged over the scans with constant concentration. Noise contributions from thermal noise ( $\sigma_T$ ) and source-induced noise ( $\sigma_{LS}$ ) are separated from the fit (see text for details). Adapted from **Publication IV**.

dependency of the PA amplitude on the concentration, is in excellent agreement with the experimental results. The fit is successful even at regions where the linear approximation of the Beer-Lambert law is not valid, because both components of the fit (amplitude and noise) experience identical nonlinearity at high concentrations. Similar behavior between the concentration and the SNR without complete saturation has also been reported in single-frequency PAS [120]. Although high SNRs cannot be

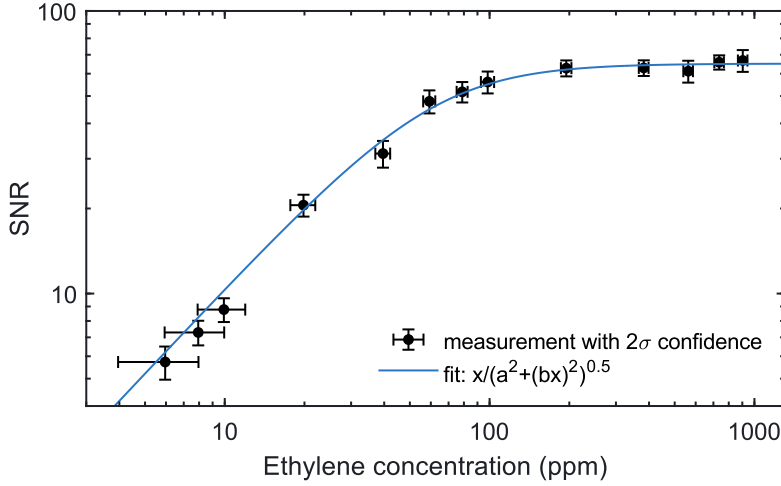


**Figure 4.5** Signal-to-noise ratio (SNR) of the single-scan FT-PAS spectra ( $\Delta\nu = 1 \text{ cm}^{-1}$ ) of  $\text{C}_2\text{H}_4$  as a function of concentration. The fit function employs linear dependence of the PA amplitude on the concentration and the noise relation described by Eq. 4.9 and Eq. 4.11. The error bars were obtained from estimated dilution errors (horizontal) and repetitive measurements at each concentration (vertical).

reached with these systems, the performance is generally not compromised as SNRs above 10 are considered sufficient and the SNR can be improved with averaging.

The relation between the RIN of the light source and the noise level has not been systematically investigated (experimentally). Ten and five times higher noise levels were reported for two SC sources compared to a thermal emitter [**Publication I**]. However, as the incident optical powers and the bandwidths of the sources are very different (which affects the noise, see Eq. 3.13) and the source-induced noise was not characterized for that system, the relation between RIN and noise cannot be evaluated reliably. In **Publication I**, incorrect conclusions concerning this matter were drawn. A reliable experimental indication on the noise-RIN dependence was found by comparing the measurements between the OFC and a filtered SC which have similar PSD spectra. The recorded FT-PAS spectra of  $\text{CH}_4$  in Fig. 4.6 display a two-fold noise level for the SC regardless of the slightly lower overall amplitude of the spectrum. The difference between the noise levels is surprisingly small as the OFC is considered temporally coherent and the SC source very noisy.

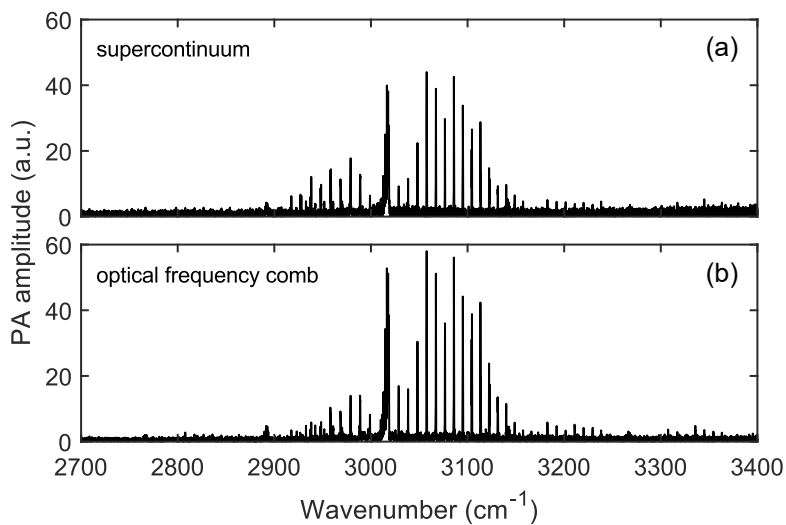


**Figure 4.6** Experimentally recorded FT-PAS spectra (single scan) of  $\text{CH}_4$  using (a) the incoherent and filtered SC and (b) the OFC source. The repetition rate of the SC was 70 kHz, the scanning interferometer was SI2 with a spectral resolution of  $0.03 \text{ cm}^{-1}$ , and the photoacoustic analyser was PAA2 with an optical enhancement of 1.8 (see Table 4.1 for more details). The noise level is two times higher in the spectrum recorded with the SC.



## 5 PERFORMANCE CHARACTERISTICS

The performance of a gas sensor compasses a variety of properties that describe the the sensor's ability to identify and quantify gas molecules. In this chapter, the capabilities of the FT-PAS systems constructed in this thesis are described in detail in terms of detection limit, dynamic range and linearity, accuracy, stability and capability for multi-species detection.

### 5.1 Detection limit

The calculation of the detection limit according to Eq. 2.4 requires background correction and an estimation of the noise level. The background signal includes contributions from light absorption by interfering molecules in the gas cell and by the cell windows. The absorption feature from the windows follows the spectrum of the light source assuming all spectral components are equally absorbed [67]. The true analyte signal can then be separated from the background using analyte and interference references and the spectrum of the light source, which are fitted to the raw PA spectrum. The background correction procedure is illustrated in Fig. 5.1 for 500 ppb of  $\text{CH}_4$ . Fig. 5.1a shows the raw PA spectrum (black line) with no clear indication of  $\text{CH}_4$  present. The  $\text{CH}_4$  spectrum corrected for interfering molecular absorption (dominated by  $\text{H}_2\text{O}$ ) and window absorption is shown in Fig. 5.1c (black line), which is in agreement with the  $\text{CH}_4$  reference weighted through the fitting routine. The contribution of  $\text{H}_2\text{O}$  absorption is shown in Fig. 5.1a, and the absorption feature from the window absorption is illustrated in Fig. 5.1b.

The reference spectrum of  $\text{CH}_4$  was recorded at a relatively high concentration of 30 ppm to mitigate the effect of window absorption while remaining in the linear region of the Beer-Lambert law (see Fig. 5.3). Furthermore, the  $\text{CH}_4$  reference was water-corrected by fitting an  $\text{H}_2\text{O}$  reference to the methane-free region of the raw reference spectrum. The PSD spectrum of the SC shown in Fig. 5.1b was estimated

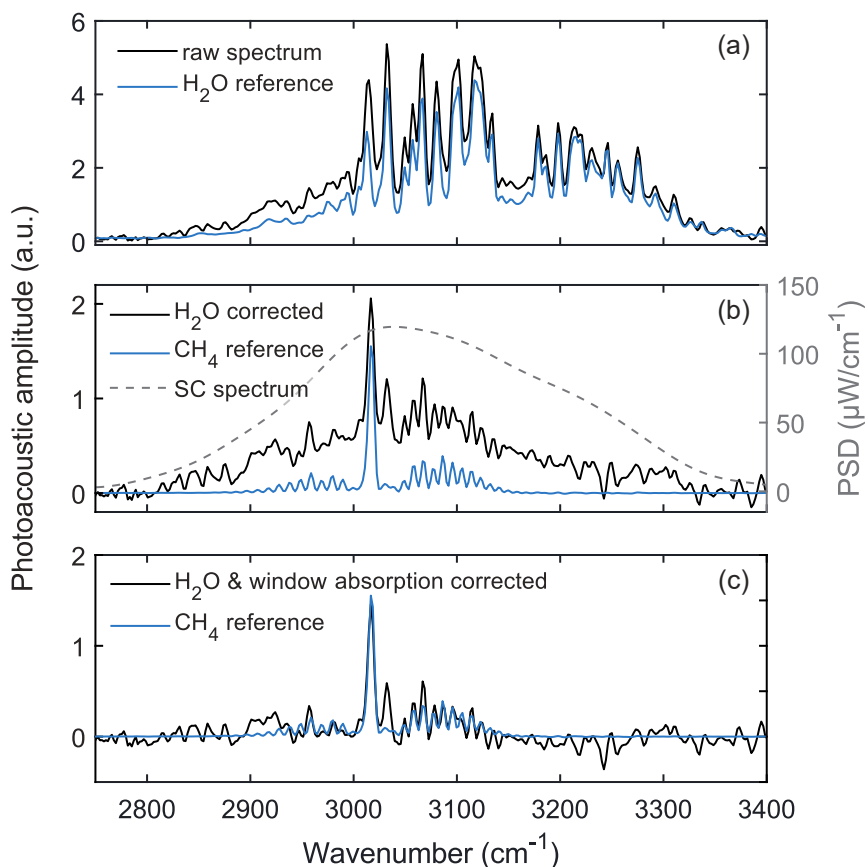


**Figure 5.1** An illustration of background correction for a spectrum containing 500 ppb of  $\text{CH}_4$  (single scan), carried out by spectrally fitting three reference spectra ( $\text{CH}_4$ ,  $\text{H}_2\text{O}$ , window) to the raw FT-PAS spectrum. The experiment employed the SC source (90 kHz repetition rate), S11 ( $4 \text{ cm}^{-1}$  spectral resolution) and PAA2 (optical enhancement of 6.3). (a) The raw spectrum (black line) and the  $\text{H}_2\text{O}$  contribution of the fit (blue line). (b) Water-corrected  $\text{CH}_4$  spectrum (black line) displaying the broad absorption feature from the windows which follows the SC spectrum (dashed grey line, right axis). This background feature is mostly eliminated during the  $\text{H}_2\text{O}$  subtraction, but typically additional correction is needed. (c) The final  $\text{CH}_4$  spectrum (black line) corrected for  $\text{H}_2\text{O}$  and window absorption with respect to the  $\text{CH}_4$  reference (blue line) also shown in plot (b).

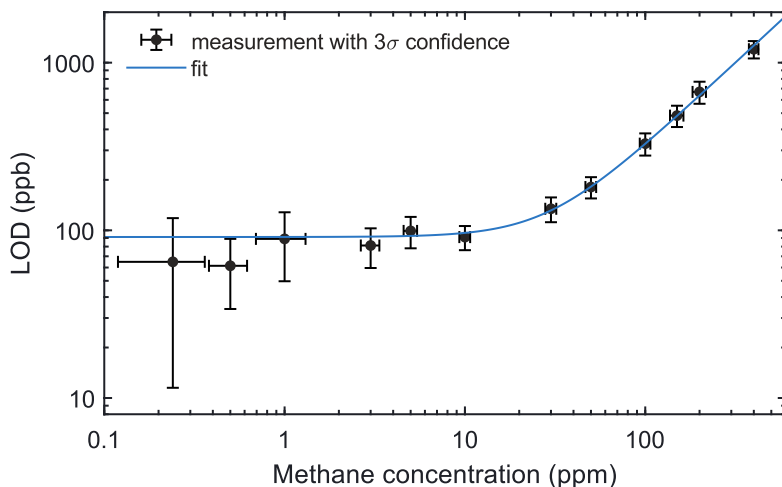


**Figure 5.2** The limit of detection (LOD) of  $\text{CH}_4$  as a function of  $\text{CH}_4$  concentration when calculating the LOD from the SNR of the background-corrected spectrum. The experiment was carried out with the SC source (90 kHz repetition rate), S11 ( $4 \text{ cm}^{-1}$  spectral resolution) and PAA2 (optical enhancement of 6.3). The fit function was  $\sqrt{a^2 + (bx)^2}$  derived from Eq. 2.4 and the fit function from Fig. 4.5.

by measuring the spectrum of the SC source at the fiber output and modelling the propagation of the SC radiation through the system. The model took into account the wavenumber-dependent losses of the employed long-pass filter and the windows of the gas cell and other experimentally observed losses of the system that were assumed to be wavenumber-independent. Absorption of atmospheric molecules (before the gas cell) could be included in the model [Publication III], but here the relevant wavenumber region is sufficiently transparent.

The noise level is typically calculated as the standard deviation of the PA amplitude in a non-absorbing spectral region (see Fig. 4.4a) [67] [Publications I–V]. Moreover, the noise level should be calculated from a spectrum where the source-induced noise is negligible compared to thermal noise, as the noise level increases significantly with the analyte concentration when using noisy light sources [Publication III]. This is illustrated in Fig. 5.2, where the LOD is calculated from measurements with varying  $\text{CH}_4$  concentrations of 0.24–500 ppm. Fig. 5.2 indicates that the noise level should be calculated from a measurement containing less than 10 ppm of  $\text{CH}_4$ , which has not always been the practice [67] [Publication I, Publication II]. The reported  $\text{CH}_4$  detection limits for different FT-PAS systems are summarized in Table 5.1, all normalized to 100 s. Besides spectral resolution and the incident PSD of the light

**Table 5.1** A summary of reported limits of detection (LOD,  $3\sigma$ , 100 s) of  $\text{CH}_4$  in **Publications I–IV**, along with the corresponding spectral resolutions ( $\Delta\nu$ ) and incident power spectral densities (PSDs) of the systems.

Light source	LOD (ppb)	$\Delta\nu$ ( $\text{cm}^{-1}$ )	PSD ( $\mu\text{W}/\text{cm}^{-1}$ )	Publication
Thermal emitter	1800	4	1.6	I
SC	990	4	31	I
OFC	3300	0.033	21	II
SC	240	13	19	III
SC	20	4	18	IV

source, differences in the LODs arise from varying optical enhancement factors, gas cell geometries and cantilever microphones (Table 4.1), apodization functions and the procedures for calculating the noise level.

Considering spectrally broadband techniques, the detection limit may alternatively be estimated by taking advantage of the entire absorption band of the target gas instead of a single spectral point in Eq. 2.4. With this approach, the LOD is calculated by recording a high-SNR reference of the analyte and spectrally fitting that to several blank measurements (no analyte in the gas cell) [94]. The fit results in a concentration trace (ideally zero on average) whose deviation yields the detection limit. Compared to the SNR-based approach, this method produces similar results when the analysed absorption spectrum has a single dominant peak such as  $\text{CH}_4$  and  $\text{C}_2\text{H}_4$  at low spectral resolutions. However, employing the multi-line fitting routine for broadband spectra with similar amplitude levels improves the LOD significantly [52].

## 5.2 Dynamic range and linearity

Dynamic range is here defined as the range of concentrations for a specific compound that can be analysed with the sensor. The lower end of the dynamic range is set by the detection limit (usually a value of  $3.3 \times \text{LOD}$  is used), which depends on the measurement parameters (spectral resolution and averaging), while the high end is limited by the nonlinearity of the Beer-Lambert law. The response curve in Fig. 5.3 demonstrates a dynamic range of 0.27–400 ppm ( $\text{CH}_4$ ) for a SC-based FT-PAS system in **Publication V**. However, the upper limit can be extended several orders of mag-



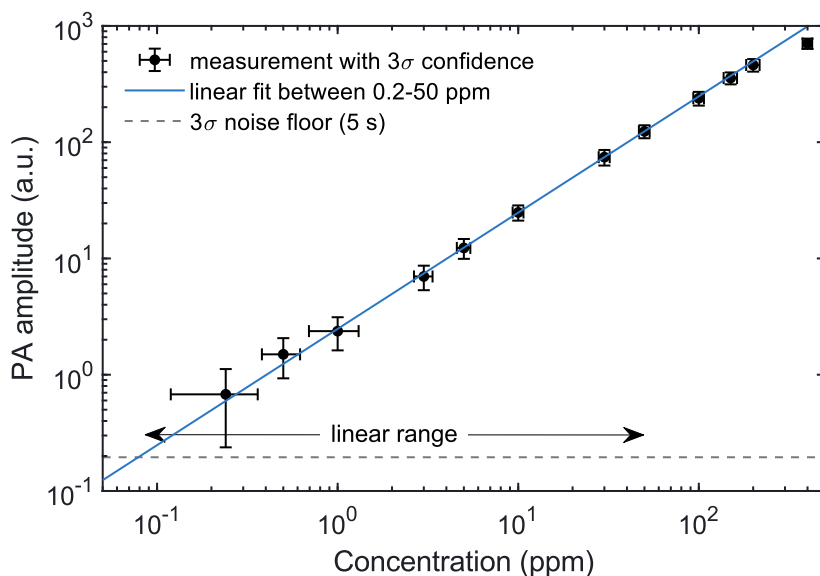


**Figure 5.3** An experimental response curve of an FT-PAS system in **Publication V** for  $\text{CH}_4$  concentrations ranging 0.24–400 ppm ( $\Delta\nu = 4 \text{ cm}^{-1}$ ). The y-axis refers to the strongest background-corrected PA amplitude of  $\text{CH}_4$ . The system exhibits high linearity ( $R^2=0.99998$ ) in the linear region of the Beer-Lambert law. The dashed grey line shows the noise level for a single scan with a confidence level of 99.7%.

nitude, especially when shifting the analysis to weaker absorption lines of the  $\text{CH}_4$  spectrum. High dynamic range of the system is largely enabled by the cantilever microphone [119], which also provides extremely linear response for concentrations below 50 ppm. The linear region of the dynamic range defines the sensitivity of the sensor, and is typically utilized in the calibration of PA systems [7, 44, 136, 175] [Publication V].

### 5.3 Accuracy

Accuracy describes the system’s ability to attain certain physical properties (e.g., the absorption coefficient or the absorption cross section) of the probed gas medium. The evaluation of accuracy requires theoretical estimation of the chosen property and the processing of experimental data into a comparable form [Publications I–V]. This comparison process for  $\text{C}_2\text{H}_4$  at  $1 \text{ cm}^{-1}$  spectral resolution is examined here in more detail [Publication IV]. The quantity under comparison is the instrument-

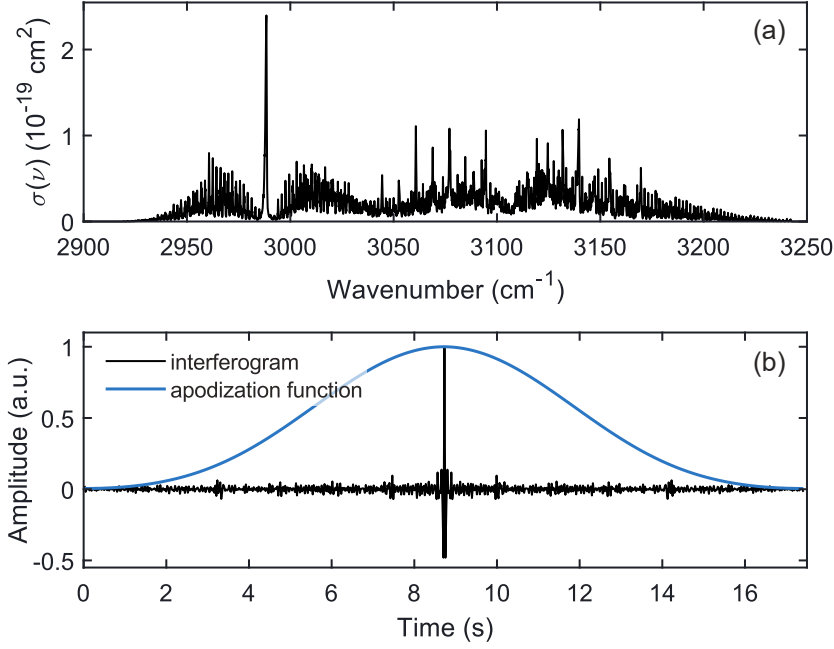


**Figure 5.4** (a) A reference  $\text{C}_2\text{H}_4$  spectrum from the HITRAN database [176]. (b) A truncated interferogram (black line) of the high-resolution spectrum in (a), and the chosen apodization function (blue line), whose multiplication and Fourier transform yields a spectrum at the desired lower spectral resolution.

modified absorption cross section  $\Lambda(\nu) * \sigma(\nu)$ , which is found in the analytical form of the FT-PAS spectrum

$$S'_0(\nu) \propto [P_I(\nu)F(\nu)] \times [\Lambda(\nu) * \sigma(\nu)] \quad (5.1)$$

obtained from Eq. 4.7 and Eq. 2.3, and including only the wavenumber-dependent quantities.

The theoretical estimation of  $\Lambda(\nu) * \sigma(\nu)$  requires a reference absorption cross section spectra of  $\text{C}_2\text{H}_4$ , shown in Fig. 5.4a and obtained from the high-resolution transmission molecular absorption database (HITRAN) [176]. This spectrum needs to be convoluted with the instrument lineshape function unless the spectral resolution of the system is high enough to resolve all features of the reference [**Publication II**]. The convolution  $\Lambda(\nu) * \sigma(\nu)$  can be represented in the time domain as a multiplication between the interferogram and the apodization function as illustrated in Fig. 5.4b. The interferogram was acquired by calculating the inverse fast Fourier transform

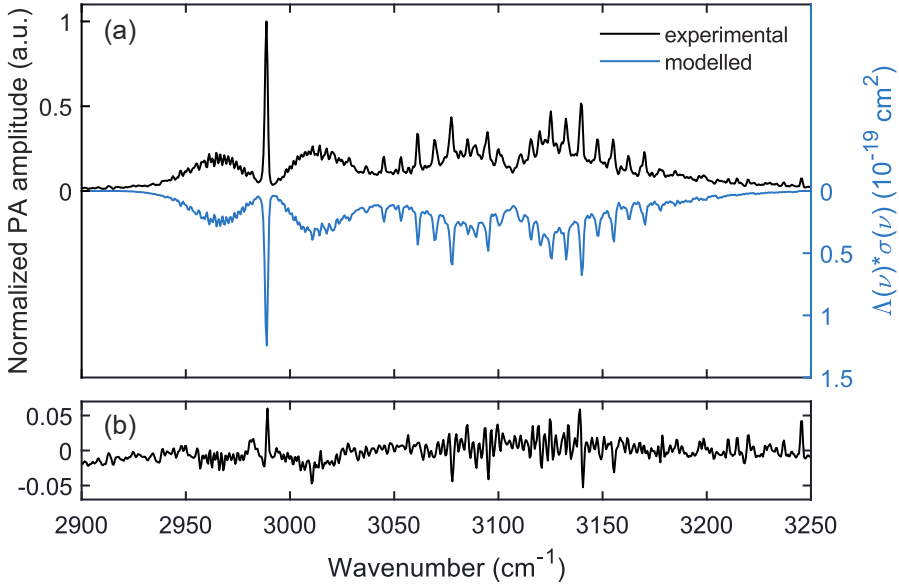


**Figure 5.5** (a) Experimentally recorded (black line, left axis) and modelled (blue line, right axis, inverted) absorption spectra of the fundamental asymmetric C–H stretching of  $\text{C}_2\text{H}_4$  at the spectral resolution of  $1\text{ cm}^{-1}$ . (b) The difference between the two spectra at (a), when the theoretical spectrum was also normalized to have values between 0 and 1.

(FFT) of the reference  $\text{C}_2\text{H}_4$  spectrum at acoustic frequencies. The resulting symmetric interferogram was then shortened from the edges and multiplied with a three-term Blackman-Harris function (blue line in Fig. 5.4b) [169]. The optimum truncation point was found near the acquisition time (20 s) by comparing the modelled spectrum at different truncation points to the experimental spectrum (black line in Fig. 5.5). Finally, the FFT of the windowed interferogram was calculated, the result shown in Fig. 5.5 (blue line, inverted).

Experimental acquisition of  $\Lambda(\nu) * \sigma(\nu)$  shown in Fig. 5.5 (black line) was carried out by dividing the background-corrected  $\text{C}_2\text{H}_4$  spectrum by the effective optical power per spectral element  $P_I(\nu)F(\nu)$  according to Eq. 5.1. This quantity is two times smaller compared to the effective PSD spectrum inside the cell (Fig. 5.1b), because the spectral sampling period of the recorded spectrum is about  $0.5\text{ cm}^{-1}$ . The experimental and simulated spectra in Fig. 5.5 are in agreement. The discrepancies are expected to result mostly from inaccurate PSD normalization due to the non-real-time recording of the SC spectrum and the approximated modelling of the SC spectrum through the system. A complete evaluation of accuracy would require

a comparison between the absolute amplitudes of the experimental and simulated quantities, which is however only possible for self-referencing systems (no calibration).

## 5.4 Stability

The deviation of the sensor's performance over time is described by stability. On times scales of a few scans, a term repeatability (or precision) is conventionally used, which describes the system's random errors or noise sources in contrast to the systematic errors reflected in the accuracy. Repeatability is most simply estimated by recording repeated measurements of an unchanged sample and analysing the fluctuations in the PA amplitude (or the retrieved concentration) over time. These fluctuations include all noise sources of the system, most importantly thermal noise, direct (average) intensity fluctuations of the light source and coupled source-induced noise  $\sigma_{LS}$ . Fig. 5.6a shows the acquired H<sub>2</sub>O concentration over 1080 s with the standard deviation of 2.6% [**Publication III**]. For another FT-PAS system, the repeatability was estimated to be 4.8% [**Publication IV**], which may suggest an unknown noise source in the latter system.

Allan-Werle deviation (AWD) is a widely used approach to analyse repeated measurements further revealing different types of noise sources, determining the longest statistically relevant averaging time for the sensor and predicting the detection limit [177]. AWDs of the high-concentration H<sub>2</sub>O trace (Fig. 5.6a) and a zero-level measurement (Fig. 5.6b, a non-absorbing region of a high-concentration measurement) are shown in Fig. 5.6c. An optimum integration time of 100 s was obtained for the high-concentration trace. Before 100 s the AWD decreases with the inverse square root of the averaging time that holds for white noise, and afterwards a drift also visible in the concentration trace (Fig. 5.6a) begins to dominate causing a sudden increase in the curve. The drift was most likely caused by the variation of the SC spectrum or H<sub>2</sub>O desorption from the cell walls. The zero-level AWD is about three times lower compared with the high-concentration AWD, indicating significant contribution from direct power fluctuations of the light source in the high-concentration trace. Therefore, the zero-level AWD predicts the detection limit more accurately, although here it still overestimates due to the source-induced noise present in the measurement. The zero-level AWD follows the theoretical curve through the entire

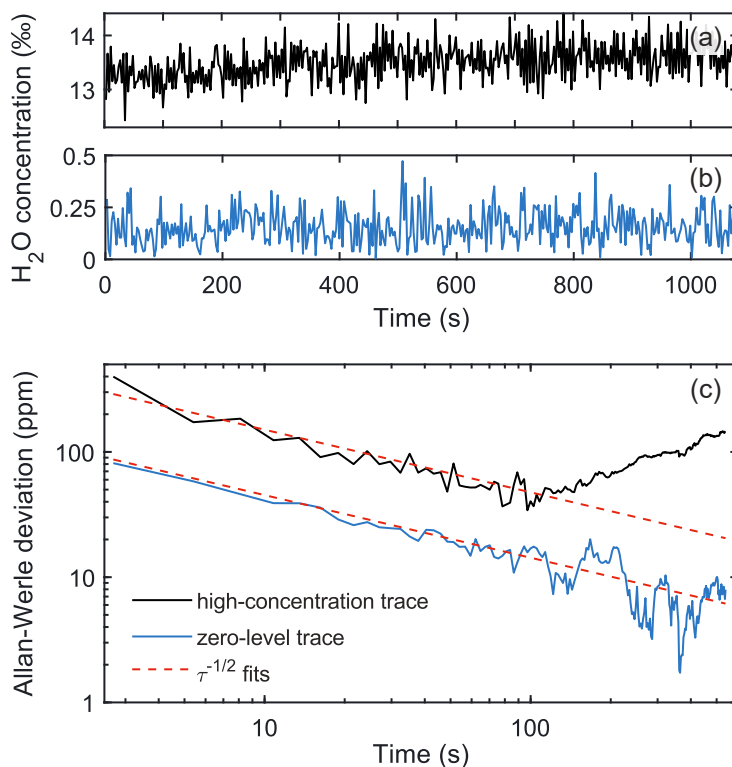


**Figure 5.6** Allan-Werle deviation of two H<sub>2</sub>O traces for the system including the SC (70 kHz repetition rate), SI3 and PAA3. (a) A high-concentration H<sub>2</sub>O trace acquired from the calibrated maximum PA amplitude of the H<sub>2</sub>O spectrum around 3800 cm<sup>-1</sup> [Publication III]. (b) A zero-level trace of H<sub>2</sub>O acquired similarly but analysing a single frequency in a non-absorbing region of the spectrum. (c) Allan-Werle deviations of the high-concentration trace (black line) and the zero-level trace (blue line), and fitted lines describing theoretical averaging of white noise (dashed red lines).

investigation period, confirming that both thermal noise and source-induced noise are white.

Allan-Werle analysis generally requires hundreds of data points to function properly, and thus it may not be a practical tool for high-resolution measurements with a long single-scan acquisition time. In such cases, stability may be evaluated by calculating the LOD as a function of the averaging time [Publication IV], or comparing the recorded spectra between a certain time period. The latter approach is shown in Fig. 5.7a, where two C<sub>2</sub>H<sub>4</sub> spectra were acquired with an 80 minute delay between them. The water-corrected spectra remain relatively stable over time, although small deviations are visible. This indicates that the light source has some long-term varia-

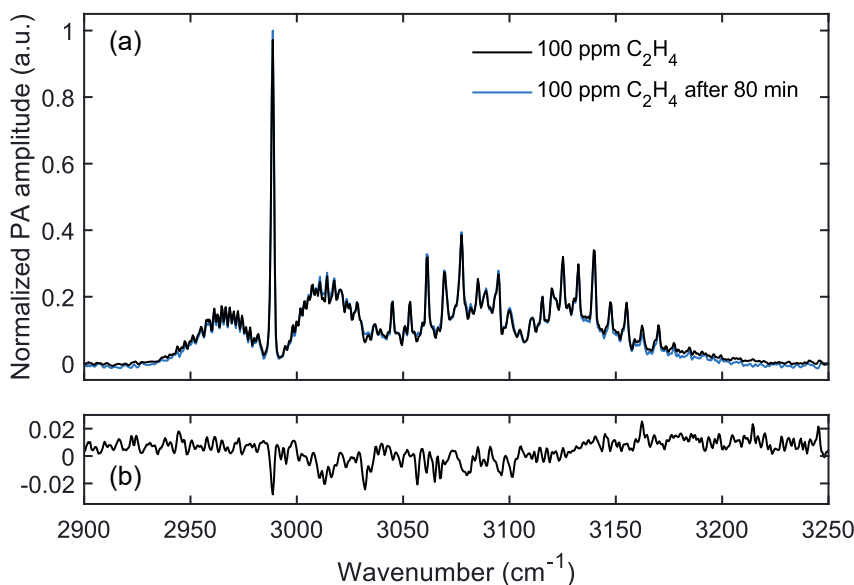


**Figure 5.7** (a) Two water-corrected and normalized C<sub>2</sub>H<sub>4</sub> spectra (100 ppm,  $\Delta\nu = 1 \text{ cm}^{-1}$ , average of 10 scans) with 80 minutes between their acquisition. (b) The residual of the two spectra.

tions in its spectrum, which calls for more frequent acquisition of the H<sub>2</sub>O reference measurement. In Fig. 5.7, the same reference was used for both spectra. Parallel acquisition of the source spectrum eliminates this problem [Publication II].

## 5.5 Multi-species detection

Detecting multiple species within the bandwidth of the light source is fairly simple in FT-PAS, thanks to the spectrally broadband and high-resolution nature of the technique and a simple contribution of each species on the total absorption coefficient (Eq. 2.3). Correct analysis of gas mixtures is the most effortless with high spectral resolution and well separated absorption bands, as shown in Fig. 5.8 for CH<sub>4</sub> and acetylene (C<sub>2</sub>H<sub>2</sub>). However, the situation remains manageable even at lower spectral resolutions and with spectrally overlapping absorption bands [Publication IV].

The spectral analysis of complex gas mixtures involves constructing a spectral library of all relevant substances and fitting this library to the investigated spectrum. The spectral library can be modelled or experimentally acquired, which is typically more accurate but laborious for a large number of species. In the linear region of

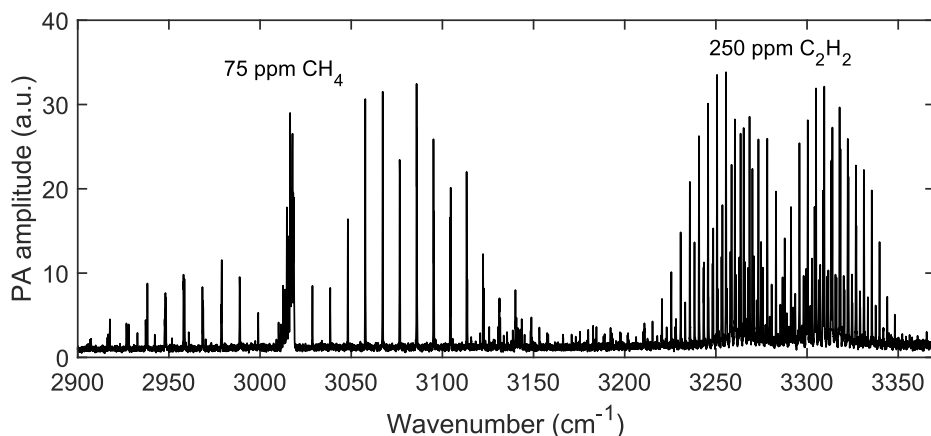


**Figure 5.8** A recorded FT-PAS spectrum (average of ten scans) of a gas mixture containing 75 ppm of  $\text{CH}_4$  and 250 ppm of  $\text{C}_2\text{H}_2$  using the SC (70 kHz repetition rate), SI2 ( $\Delta\nu = 0.033 \text{ cm}^{-1}$ ) and PAA2 (optical enhancement of 1.8). Fundamental asymmetric C–H stretching bands are clearly visible and separable,  $\text{CH}_4$  on the left and  $\text{C}_2\text{H}_2$  on the right.

the Beer-Lambert law, the fit routine can simply be a linear least squares fit implemented by solving a matrix equation  $Ax = B$ , where  $A$  is the spectral library (spectra in separate columns) and  $B$  is the spectrum under investigation (a column vector). When the concentrations in the spectral library are known (a column vector  $c$ ), the concentrations in the gas mixture can be retrieved from the element-by-element multiplication  $c \times x$ .

Fig. 5.9 illustrates the analysis of a gas mixture containing 26 ppm of ethane ( $\text{C}_2\text{H}_6$ ), 120 ppm of  $\text{C}_2\text{H}_4$  and 8 ppm of propane ( $\text{C}_3\text{H}_8$ ). The spectral library was experimentally acquired by measuring  $\text{C}_2\text{H}_6$ ,  $\text{C}_2\text{H}_4$ ,  $\text{C}_3\text{H}_8$  and  $\text{H}_2\text{O}$  at concentrations of 30 ppm, 100 ppm, 20 ppm and  $\sim 7000$  ppm respectively, and subtracting the water residual from the hydrocarbon references. Moreover, the absorption feature from the window absorption was included in the library. All spectra (including the spectral library and the analysed spectrum) were corrected for the elevated baseline of the spectrum resulting from the positively-valued noise (Fig. 4.4a). As seen in Fig. 5.9c, the concentrations in the mixture are accurately retrieved within the measurement uncertainty.

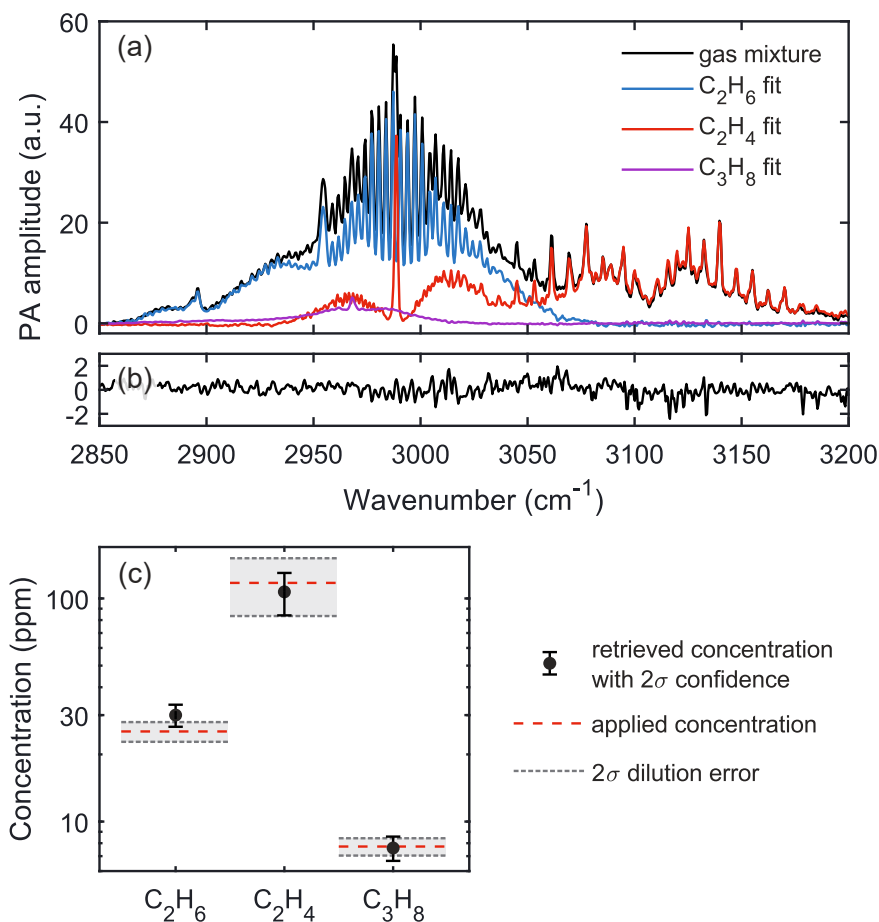


**Figure 5.9** The analysis of a gas mixture containing three hydrocarbons (C<sub>2</sub>H<sub>6</sub>, C<sub>2</sub>H<sub>4</sub> and C<sub>3</sub>H<sub>8</sub>) at concentrations ranging 8–120 ppm using a system comprised of the SC source (70 kHz repetition rate), SI1 ( $\Delta\nu = 1 \text{ cm}^{-1}$ ) and PAA2 (optical enhancement of 6.3). (a) Investigated spectra of the gas mixture (black) and reference spectra of the hydrocarbon species (blue, red, magenta), weighted according to the spectral fitting. (b) The residual of the spectral fit. (c) Retrieved concentrations (black dots) with respect to the applied concentrations (dashed red lines). Dashed grey lines indicate dilution error.



## 6 APPLICATIONS

The combination of a small sample volume, low detection limits, a wide dynamic range and the possibility for selective multi-species detection are the main advantages of cantilever-enhanced FT-PAS compared with other absorption spectroscopy techniques. This holds especially when implementing the technique with a high-power light source. Among other broadband techniques, the low gas consumption of FT-PAS is especially attractive as it speeds up the gas exchange process in continuous monitoring and enables the analysis of samples with limited quantity. As an example, an OFC-based FT-PAS system has been applied in an academic setting for the detection of radiocarbon  $\text{CH}_4$  requiring an extreme combination of high spectral resolution, a low detection limit and a small sample volume [67]. In this chapter, potential industrial application areas for FT-PAS are discussed. The focus is on compounds that can be efficiently detected with the most recent SC-based system [**Publication IV**], but general applicability of FT-PAS and its future potential is also considered.

### 6.1 Hydrocarbons and volatile organic compounds

Hydrocarbons and volatile organic compounds (VOCs, room temperature vapor pressure above 10 Pa [178]) are present in countless occasions in industry and our daily lives [179]. These substances contain C–H bonds enabling efficient detection in a spectral region around  $3000\text{ cm}^{-1}$ , which is often very congested. Therefore, broadband optical sensors in particular benefit from probing more unique vibrational bending bands around  $1000\text{ cm}^{-1}$  [63, 75], but reliable operation around  $3000\text{ cm}^{-1}$  has been demonstrated using sensors with sufficient spectral resolution and bandwidth [94, 180] [**Publication IV**]. The detection of hydrocarbons ( $\text{CH}_4$ ,  $\text{C}_2\text{H}_2$ ,  $\text{C}_2\text{H}_4$ ,  $\text{C}_2\text{H}_6$  and  $\text{C}_3\text{H}_8$ ) using FT-PAS is demonstrated throughout this thesis [**Publications I–IV**], and the analysis of organophosphorus compounds in **Publica-**

**tion V** illustrates the applicability for VOCs. However, there has been little discussion about the specific application areas of these substances, and therefore a few special applications requiring high-performance detection (e.g., low detection limits for multiple species simultaneously) are reviewed here.

The first application sector is automotive industry, since exhaust emissions from vehicles are a major source of air pollution [181]. Depending on the fuel type, several hydrocarbons and VOCs (e.g., ethanol and formaldehyde) are emitted in the burning process, and monitoring down to ppb-level is required to comply with current and future legislation and to optimize the burning process [9]. Exhaust gases also contain numerous other compounds such as nitrous oxide and sulfur dioxide that cannot be detected with a reasonable sensitivity using the current FT-PAS system. However, this issue could be overcome in the future by new light sources.

Another industrial application with a strong safety aspect is occupational health monitoring in coal mines. Coal mines are hazardous environments where coal combustion may cause fire due to oxidization of residue coal [22]. Besides oxygen, carbon monoxide (CO) and carbon dioxide (CO<sub>2</sub>), the oxidization process is characterized by monitoring hydrocarbons (CH<sub>4</sub>, C<sub>2</sub>H<sub>2</sub> and C<sub>2</sub>H<sub>4</sub>) with a required detection limit of 10 ppb [22]. While the detection sensitivity of FT-PAS is close to the requirement, a typically high CH<sub>4</sub> concentration could compromise the accessible detection limits by increasing the noise level.

The examination of power transformers is an established application for optical gas sensing. The decomposition of electrical insulating oil in power transformers generates various hydrocarbons (CH<sub>4</sub>, C<sub>2</sub>H<sub>2</sub>, C<sub>2</sub>H<sub>4</sub> and C<sub>2</sub>H<sub>6</sub>) whose concentrations indicate malfunctions (overheating, partial discharge and arcing in oil) and their severity [8]. Dissolved gas analysis (DGA) typically performed from the headspace of an oil container is a standard method to monitor the gases dissolved in the transformer oil due to oil decomposition. Compared with current optical measurement technologies in DGA such as NDIR, PAS and FTIR, FT-PAS provides lower detection limits and wider dynamic ranges [182]. However, it should be noted that many existing instruments can monitor other important molecules such as CO and CO<sub>2</sub>, which cannot be detected using current SC-based FT-PAS systems with decent sensitivity.

One potential medical application concerns surgeries carried out with an electrical knife. Such operations are potentially hazardous for the health professionals

due to the released smoke that contains hydrocarbons and VOCs at concentrations ranging 0.05–10 ppm [183, 184]. Moreover, the detection and analysis of surgical plume enables intraoperative tissue identification providing fast removal of tumors with a maximal conservation of healthy tissue [25]. The discrimination between malignant and benign tissue results from different composition of lipids [185, 186], whose ro-vibrational absorption bands potentially possess identifiable features. The detection of surgical smoke using FT-PAS is attractive due to the technique's small sample volume, fast response time and sufficient sensitivity.

## 6.2 Chemical warfare agents

Chemical warfare agents (CWAs) comprise a variety of toxic substances that are deployed with a purpose to injure or kill people in military operations. CWAs are classified according to their effect mechanism on a human body, well-known categories being blister agents (e.g., mustard gas), blood agents (e.g., arsine), choking agents (e.g., phosgene) and nerve agents (e.g., sarin). Although reportedly deployed already in ancient Greece and China [187], the widespread use of CWAs was initiated in World War I and continued in the Iran–Iraq war [188] and the Syrian civil war [189, 190]. CWAs have also found usage outside warfare, most notoriously in the terrorist attack to the Tokyo subway [191, 192] and in the assassination attempts of Sergei Skripal [193, 194] and Alexei Navalny [195].

Despite legislative effort to ban the use of CWAs, they clearly pose a persistent threat to both military operatives and civilians. Extensive research effort has therefore been focused towards high-performance detectors for reliable identification of CWAs for screening, the diagnosis and treatment of poisoning, occupational health monitoring and forensic investigation [20, 196–208]. The detection of a large pool of CWA compounds is complicated by the fast degradation of many agents and their varying room-temperature properties. As a result, a single system is unlikely capable of covering all substances. Optical methods are an exceptional option to detect gaseous (blood and choking) agents and volatile G-type nerve agents [208]. The large molecular size of CWAs lead to very broad IR absorption bands, and thus broadband techniques such as QCL-based PAS [204, 205], OPO-based remote detection [206] and FTS have been reported [207, 208] [**Publication V**].

For safety purposes, experimental demonstrations of CWA detectors are typi-

cally carried out using simulant compounds whose molecular structure resembles the relevant agent(s) [198, 203–205]. Accepted simulants for gaseous G-series nerve agents are organophosphorous compounds, which were analysed with the SC-based FT-PAS system [**Publication V**]. Fig. 6.1 shows the recorded ro-vibrational absorption spectra of the fundamental asymmetric C–H stretches of four simulant substances. These results are in agreement with reference FTIR spectra [209]. Despite similar broad spectral features, high selectivity between the simulant compounds was demonstrated [**Publication V**].

Fig. 6.2 shows the spectrum of diisopropyl methylphosphonate (DIMP) at a concentration of 130 ppb, which is the lowest experimentally recorded quantity of any species in this thesis. The LOD of DIMP was estimated to be 64 ppb in one minute of averaging, although the detection limit achieved for external samples was about three times higher due to sampling losses [**Publication V**]. However, the sampling efficiency of the FT-PAS system was significantly higher compared to a conventional FTIR system due to the smaller sample volume [208]. The LOD for sarin was estimated to be 180 ppb in one minute for an external sample. The demonstrated performance is exceptional considering the sample volume of about 7 ml, which would aid in the analysis of field samples with limited quantity. Besides G-series nerve agents, other CWAs such as mustard gas and lewisite could also be detected with the developed FT-PAS system [210].

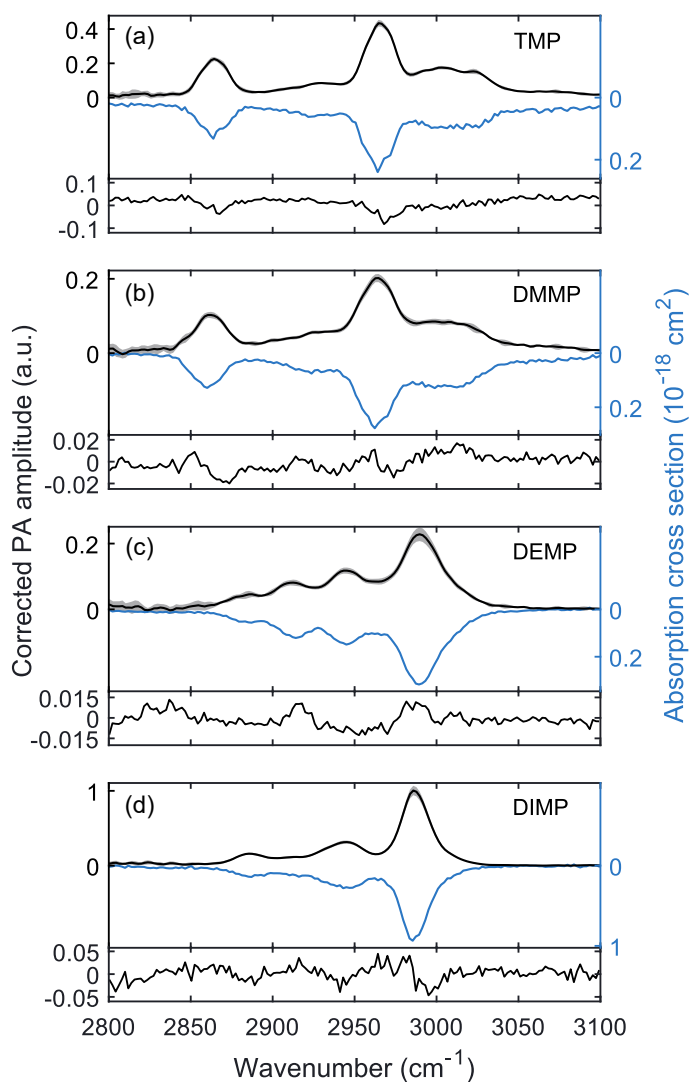


**Figure 6.1** Experimentally recorded, background-corrected and power-normalized FT-PAS spectra (black lines, left axis) of (a) trimethyl phosphate (TMP), (b) dimethyl methylphosphonate (DMMP), (c) diethyl methylphosphonate (DEMP) and (d) diisopropyl methylphosphonate (DIMP), and the corresponding FTIR reference spectra (blue lines, inverted, right axis) [209]. The differences between the experiments and the references are shown at the bottom panels in each plot. The simulant samples were prepared with concentrations ranging 120–310 ppm, and the FT-PAS spectra were acquired at  $4\text{ cm}^{-1}$  spectral resolution and averaged over 12 scans (the standard deviation is shown in grey). [Publication V]

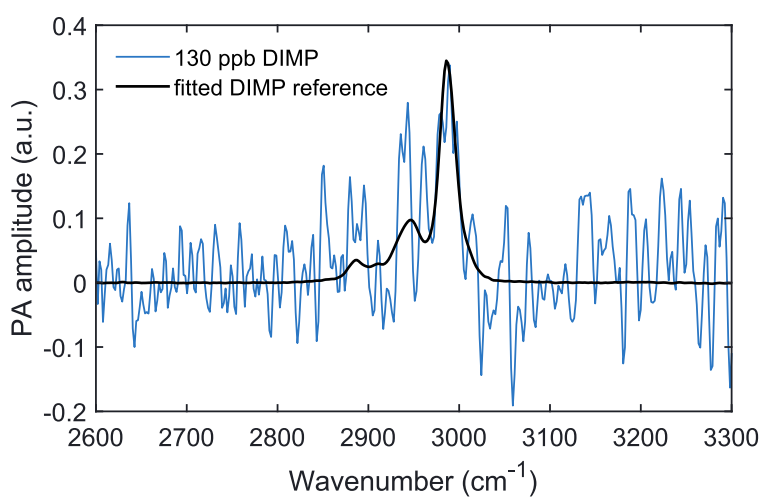


**Figure 6.2** A measured and background-corrected FT-PAS spectrum of 130 ppb DIMP (blue line) at  $\Delta\nu = 4 \text{ cm}^{-1}$  and 15 s of averaging, and a fitted DIMP reference (black line) that was experimentally recorded at a high concentration.

## 7 CONCLUSIONS

Increased awareness in environmental and health hazards has boosted the importance of gas sensing in atmospheric science, industrial process control and the safety of urban environments. Optical gas detection methods based on the absorption of light by gas molecules are attractive for many applications due to their real-time and field-portable operation with high sensitivity and selectivity. This thesis introduces a new optical gas sensing technique, Fourier transform photoacoustic spectroscopy (FT-PAS) with broadband mid-infrared (mid-IR) lasers and a cantilever microphone. The technique proved experimentally realizable [**Publication I**], combining the fast and spectrally high-resolution detection of Fourier transform spectroscopy (FTS), the sensitive and broadband operation of cantilever-enhanced photoacoustic spectroscopy (PAS), and the high sensitivity of mid-IR supercontinuum (SC) and optical frequency comb (OFC) spectroscopy.

The performance of the technique was demonstrated to be excellent and predictable. Wide spectral bandwidths of the SC and OFC-based systems were  $400\text{ cm}^{-1}$  and  $200\text{ cm}^{-1}$  respectively, centered around  $3050\text{ cm}^{-1}$  and only limited by the light source. However, the operational spectral range of the SC-based sensor could be extended to near-IR wavelengths. Thanks to the high spatial coherence of the SC and OFC light sources, spectral resolution is only limited by the scanning range of the interferometer with no compromise on the sensitivity. Most experiments were conducted at spectral resolutions of  $1\text{--}4\text{ cm}^{-1}$ , but an extremely low resolution of  $0.013\text{ cm}^{-1}$  limited by pressure broadening was also demonstrated [**Publication II**]. Experimental systems were also shown to be extremely linear over three orders of magnitude and only limited by the Beer-Lambert law, sufficiently stable over minutes and even hours, and capable for multi-species detection of gas mixtures with a significant spectral overlap. Furthermore, acquired results were in agreement with simulations.

A detection limit of 90 parts per billion in volume (ppb) for methane was obtained

in a single 5 s scan ( $4\text{ cm}^{-1}$  resolution), which could be lowered down to 26 ppb or 3.4 ppb by averaging for one minute or one hour respectively [**Publication IV**]. Besides the high-power SC source and the cantilever microphone, high sensitivity was provided by a custom-built optical multipass cell. Detection limits were originally expected to be limited by the short-term intensity fluctuations of the employed SC source [**Publication I**], but this misconception was later corrected [**Publication III**]. It was found that in FT-PAS, the source-induced noise is proportional to the gas concentrations. As a result, in single-species detection the source-induced noise vanishes at the detection limit, and Brownian noise becomes the limiting noise source. However, absorption from interfering species increases this noise contribution, and thus the detection limits in multi-species detection may be compromised by the intensity fluctuations of the light source.

The performance of the technique is competitive with other sensitive and broadband optical techniques that have a significantly higher gas consumption. Table 7.1 shows a comparison between SC-based FT-PAS [**Publication IV**] and selected recent implementations of a few competing techniques. Although the comparison is not complete, it is clear that the main advantage of FT-PAS is a remarkable, two orders of magnitude smaller sample volume beneficial for example in the analysis of volatile substances and limited samples [67] [**Publication V**]. Wavelength-independent detection and direct proportionality between the recorded signal and optical power are other benefits relevant when extending the performance of FT-PAS with new light sources. The disadvantages of cantilever-enhanced FT-PAS are its relatively slow detection, sensitivity to strong external acoustic and mechanical vibrations, and the requirement of a closed gas cell which obstructs in situ measurements of gas flows. Furthermore, the technique is not absolute but calibration is required for an accurate concentration retrieval.

Looking forward, the most significant performance enhancement of FT-PAS is expected through better SC and OFC light sources available already at the moment and especially in the future. Higher power spectral densities (PSDs) and wider spectral bandwidths of these sources provide more sensitive detection of a larger number of species. Designing the spectrum of the light source for specific target gases is especially important in FT-PAS due to the source-induced noise component from excess absorption. In theory, it would be further possible to eliminate the source-induced noise component for a specific gas matrix by designing the intensity correlation of



**Table 7.1** A comparison of the FT-PAS system in **Publication IV** with selected systems based on other detection principles. Systems are compared in terms of limit of detection (LOD,  $3\sigma$ , 100 s) of  $\text{CH}_4$ , spectral resolution ( $\Delta\nu$ ) and sample volume ( $V_{\text{sample}}$ ). \*Two orders of magnitude weaker absorption features were analysed.

Technique	Light source	LOD (ppb)	$\Delta\nu$ ( $\text{cm}^{-1}$ )	$V_{\text{sample}}$ (ml)	Reference
FT-PAS	SC	20	4	7	<b>Publication IV</b>
DAS	SC	30	2.5	850	[94]
DCS	ICL	1500*	0.32	500	[107]
FTS	Thermal	16	0.5	200	[211]

the source appropriately. Further improvement in sensitivity can be achieved with a better multipass cell. More transparent windows provide a simple approach to increase the total PSD inside the gas cell, which can be fully optimized by redesigning the photoacoustic cell considering the multipass configuration. The footprint of the system can be significantly reduced by miniaturizing the scanning interferometer, because light sources with high spatial coherence can propagate through a significantly smaller instrument. As an example, a large variety of microelectromechanical interferometers have been recently developed [212–217], but high spectral resolutions ( $<4 \text{ cm}^{-1}$ ) have been difficult to achieve so far. Moreover, the interferometer could be replaced by a dual-comb approach already demonstrated with other microphones [68–70]. An implementation with the cantilever microphone is possible with precisely controlled combs, but the major advantage of a fast acquisition cannot be fully realized due to the limited frequency range of the cantilever.

The exploration of FT-PAS with broadband laser sources is still in its infancy, and the full potential and applicability of the technique remains to be seen. The uniqueness of the technique lies in the high-performance optical detection in small sample volumes, and in the potential to progress through the development of new light sources. The specific systems developed in this thesis are most suitable for analysing hydrocarbons and volatile organic compounds which have a variety of industrial, environmental and medical applications, but the technique can relatively easily be implemented for new species. Currently, one of the most promising applications for FT-PAS is the detection of volatile chemical warfare agents deployed in assassinations, terrorist attacks and warfare [**Publication V**]. As such, the technique provides a valuable and complementary tool for the analysis of field samples with limited quantity, contributing to the diagnosis of poisoning and forensic investigation.



## REFERENCES

- [1] P. Bauer, A. Thorpe and G. Brunet. The quiet revolution of numerical weather prediction. *Nature* 525.7567 (2015), 47–55.
- [2] J. Fenger. Urban air quality. *Atmospheric Environment* 33.29 (1999), 4877–4900.
- [3] C.-I. Chang. *Hyperspectral imaging: techniques for spectral detection and classification*. Vol. 1. Springer Science & Business Media, 2003.
- [4] H. Wang, B. Wang, B. Liu, X. Meng and G. Yang. Pedestrian recognition and tracking using 3D LiDAR for autonomous vehicle. *Robotics and Autonomous Systems* 88 (2017), 71–78.
- [5] R. O. Dubayah and J. B. Drake. Lidar remote sensing for forestry. *Journal of Forestry* 98.6 (2000), 44–46.
- [6] W. Den, H. Bai and Y. Kang. Organic airborne molecular contamination in semiconductor fabrication clean rooms: a review. *Journal of The Electrochemical Society* 153.2 (2006), G149.
- [7] T. Schmid. Photoacoustic spectroscopy for process analysis. *Analytical and Bioanalytical Chemistry* 384.5 (2006), 1071–1086.
- [8] N. A. Bakar, A. Abu-Siada and S. Islam. A review of dissolved gas analysis measurement and interpretation techniques. *IEEE Electrical Insulation Magazine* 30.3 (2014), 39–49.
- [9] P. Aakko-Saksa, P. Roslund and P. Koponen. Development and validation of comprehensive emission measurement methods for alternative fuels at VTT. *VTT: Helsinki, Finland* (2017), 102.

- [10] K. Eslami Jahromi, Q. Pan, A. Khodabakhsh, C. Sikkens, P. Assman, S. M. Cristescu, P. M. Moselund, M. Janssens, B. E. Verlinden and F. J. Harren. A broadband mid-infrared trace gas sensor using supercontinuum light source: applications for real-time quality control for fruit storage. *Sensors* 19.10 (2019), 2334.
- [11] N. Docquier and S. Candel. Combustion control and sensors: a review. *Progress in Energy and Combustion Science* 28.2 (2002), 107–150.
- [12] J. Schalwig, G. Müller, M. Eickhoff, O. Ambacher and M. Stutzmann. Group III-nitride-based gas sensors for combustion monitoring. *Materials Science and Engineering: B* 93.1-3 (2002), 207–214.
- [13] S. H. Pyun, J. Cho, D. F. Davidson and R. K. Hanson. Interference-free mid-IR laser absorption detection of methane. *Measurement Science and Technology* 22.2 (2011), 025303.
- [14] L. Scholz, A. O. Perez, B. Bierer, J. Wöllenstein and S. Palzer. Gas sensors for climate research. *Sensors and Measuring Systems; 19th ITG/GMA-Symposium*. VDE. 2018, 1–4.
- [15] A. Khan, D. Schaefer, L. Tao, D. J. Miller, K. Sun, M. A. Zondlo, W. A. Harrison, B. Roscoe and D. J. Lary. Low power greenhouse gas sensors for unmanned aerial vehicles. *Remote Sensing* 4.5 (2012), 1355–1368.
- [16] C. A. Reber, C. E. Trevathan, R. J. McNeal and M. R. Luther. The upper atmosphere research satellite (UARS) mission. *Journal of Geophysical Research: Atmospheres* 98.D6 (1993), 10643–10647.
- [17] R. Binions and A. Naik. Metal oxide semiconductor gas sensors in environmental monitoring. *Semiconductor gas sensors*. Elsevier, 2013, 433–466.
- [18] P.-S. Murvay and I. Silea. A survey on gas leak detection and localization techniques. *Journal of Loss Prevention in the Process Industries* 25.6 (2012), 966–973.
- [19] K. S. Yoo. Gas Sensors for Monitoring Air Pollution. *Monitoring, Control and Effects of Air Pollution*. Ed. by A. G. Chmielewski. Rijeka: IntechOpen, 2011. Chap. 3. DOI: 10.5772/19967. URL: <https://doi.org/10.5772/19967>.
- [20] K. Kim, O. G. Tsay, D. A. Atwood and D. G. Churchill. Destruction and detection of chemical warfare agents. *Chemical Reviews* 111.9 (2011), 5345–5403.

- [21] D. Levy and E. G. Diken. Field Identification of Unknown Gases and Vapors Via IR Spectroscopy for Homeland Security and Defense. *IEEE Sensors Journal* 10 (2010), 564–571.
- [22] T. Liu, Y. Wei, G. Song, B. Hu, L. Li, G. Jin, J. Wang, Y. Li, C. Song, Z. Shi et al. Fibre optic sensors for coal mine hazard detection. *Measurement* 124 (2018), 211–223.
- [23] R. V. Martin. Satellite remote sensing of surface air quality. *Atmospheric Environment* 42.34 (2008), 7823–7843.
- [24] C. Wang and P. Sahay. Breath analysis using laser spectroscopic techniques: breath biomarkers, spectral fingerprints, and detection limits. *Sensors* 9.10 (2009), 8230–8262.
- [25] M. Sutinen, A. Kontunen, M. Karjalainen, J. Kiiski, J. Hannus, T. Tolonen, A. Roine and N. Oksala. Identification of breast tumors from diathermy smoke by differential ion mobility spectrometry. *European Journal of Surgical Oncology* 45.2 (2019), 141–146.
- [26] J. Hodgkinson and R. D. Pride. Methane-specific gas detectors: the effect of natural gas composition. *Measurement Science and Technology* 21.10 (2010), 105103.
- [27] IPCC. Summary for Policymakers. *Climate Change 2013: The Physical Science Basis. Contribution of Working Group I to the Fifth Assessment Report of the Intergovernmental Panel on Climate Change*. Ed. by T. Stocker, D. Qin, G.-K. Plattner, M. Tignor, S. Allen, J. Boschung, A. Nauels, Y. Xia, V. Bex and P. Midgley. Cambridge, United Kingdom and New York, NY, USA: Cambridge University Press, 2013. Chap. SPM, 1–30. ISBN: 978-1-107-66182-0. URL: [www.climatechange2013.org](http://www.climatechange2013.org).
- [28] European Commission. *Emissions monitoring & reporting*. Accessed: 23 September 2022. URL: [https://climate.ec.europa.eu/eu-action/climate-strategies-targets/progress-made-cutting-emissions/emissions-monitoring-reporting\\_en](https://climate.ec.europa.eu/eu-action/climate-strategies-targets/progress-made-cutting-emissions/emissions-monitoring-reporting_en).
- [29] United Nations. *Paris Agreement*. Accessed: 4 June 2019. 2015. URL: <https://unfccc.int/process-and-meetings/the-paris-agreement>.

- [30] J. Hodgkinson and R. P. Tatam. Optical gas sensing: a review. *Measurement Science and Technology* 24.1 (2012), 012004.
- [31] X. Liu, S. Cheng, H. Liu, S. Hu, D. Zhang and H. Ning. A survey on gas sensing technology. *Sensors* 12.7 (2012), 9635–9665.
- [32] S. Feng, F. Farha, Q. Li, Y. Wan, Y. Xu, T. Zhang and H. Ning. Review on smart gas sensing technology. *Sensors* 19.17 (2019), 3760.
- [33] S. R. Morrison. Semiconductor gas sensors. *Sensors and Actuators* 2 (1981), 329–341.
- [34] J. Zhang, Z. Qin, D. Zeng and C. Xie. Metal-oxide-semiconductor based gas sensors: screening, preparation, and integration. *Physical Chemistry Chemical Physics* 19.9 (2017), 6313–6329.
- [35] H. Ji, W. Zeng and Y. Li. Gas sensing mechanisms of metal oxide semiconductors: a focus review. *Nanoscale* 11.47 (2019), 22664–22684.
- [36] H. Bai and G. Shi. Gas sensors based on conducting polymers. *Sensors* 7.3 (2007), 267–307.
- [37] E. Llobet. Gas sensors using carbon nanomaterials: A review. *Sensors and Actuators B: Chemical* 179 (2013), 32–45.
- [38] J. Cheeke and Z. Wang. Acoustic wave gas sensors. *Sensors and Actuators B: Chemical* 59.2-3 (1999), 146–153.
- [39] N.-H. Park, T. Akamatsu, T. Itoh, N. Izu and W. Shin. Calorimetric thermoelectric gas sensor for the detection of hydrogen, methane and mixed gases. *Sensors* 14.5 (2014), 8350–8362.
- [40] H. M. McNair and J. M. Miller. *Basic gas chromatography*. John Wiley & Sons, 2011.
- [41] W. W. Parson. *Modern optical spectroscopy*. Vol. 2. Springer, 2007.
- [42] G. A. West, J. J. Barrett, D. R. Siebert and K. V. Reddy. Photoacoustic spectroscopy. *Review of Scientific Instruments* 54.7 (1983), 797–817.
- [43] J. Kauppinen, K. Wilcken, I. Kauppinen and V. Koskinen. High sensitivity in gas analysis with photoacoustic detection. *Microchemical Journal* 76.1-2 (2004), 151–159.

- [44] T. Tomberg, M. Vainio, T. Hieta and L. Halonen. Sub-parts-per-trillion level sensitivity in trace gas detection by cantilever-enhanced photo-acoustic spectroscopy. *Scientific Reports* 8.1 (2018), 1848.
- [45] B. C. Smith. *Fundamentals of Fourier transform infrared spectroscopy*. CRC press, 2011.
- [46] C. A. Michaels, T. Masiello and P. M. Chu. Fourier transform spectrometry with a near-infrared supercontinuum source. *Applied Spectroscopy* 63.5 (2009), 538–543.
- [47] V. V. Goncharov and G. E. Hall. Supercontinuum Fourier transform spectrometry with balanced detection on a single photodiode. *The Journal of Chemical Physics* 145.8 (2016), 084201.
- [48] I. Zorin, J. Kilgus, K. Duswald, B. Lendl, B. Heise and M. Brandstetter. Sensitivity-enhanced fourier transform mid-infrared spectroscopy using a supercontinuum laser source. *Applied Spectroscopy* 74.4 (2020), 485–493.
- [49] M. Abbas, K. Jahromi, M. Nematollahi, R. Krebbers, N. Liu, G. Woyessa, O. Bang, L. Huot, F. Harren and A. Khodabakhsh. Fourier transform spectrometer based on high-repetition-rate mid-infrared supercontinuum sources for trace gas detection. *Optics Express* 29.14 (2021), 22315–22330.
- [50] J. Mandon, G. Guelachvili and N. Picqué. Fourier transform spectroscopy with a laser frequency comb. *Nature Photonics* 3.2 (2009), 99–102.
- [51] A. Foltynowicz, P. Maśłowski, T. Ban, F. Adler, K. Cossel, T. Briles and J. Ye. Optical frequency comb spectroscopy. *Faraday Discussions* 150 (2011), 23–31.
- [52] F. Adler, P. Maśłowski, A. Foltynowicz, K. C. Cossel, T. C. Briles, I. Hartl and J. Ye. Mid-infrared Fourier transform spectroscopy with a broadband frequency comb. *Optics Express* 18.21 (2010), 21861–21872.
- [53] I. Zorin, P. Gattinger, A. Ebner and M. Brandstetter. Advances in mid-infrared spectroscopy enabled by supercontinuum laser sources. *Optics Express* 30.4 (2022), 5222–5254.
- [54] N. Picqué and T. W. Hänsch. Frequency comb spectroscopy. *Nature Photonics* 13.3 (2019), 146–157.
- [55] J. M. Dudley, G. Genty and S. Coen. Supercontinuum generation in photonic crystal fiber. *Reviews of Modern Physics* 78.4 (2006), 1135.

- [56] S. A. Diddams. The evolving optical frequency comb. *JOSA B* 27.11 (2010), B51–B62.
- [57] N. Sharma, I. Arnold, H. Moosmüller, W. Arnott and C. Mazzoleni. Photoacoustic and nephelometric spectroscopy of aerosol optical properties with a supercontinuum light source. *Atmospheric Measurement Techniques* 6.12 (2013), 3501.
- [58] J. G. Radney and C. D. Zangmeister. Measurement of gas and aerosol phase absorption spectra across the visible and near-IR using supercontinuum photoacoustic spectroscopy. *Analytical Chemistry* 87.14 (2015), 7356–7363.
- [59] R. Selvaraj, N. J. Vasa and S. Shiva Nagendra. Off-resonance photoacoustic spectroscopy technique for multi-gas sensing in biogas plants. *Analytical Chemistry* 91.22 (2019), 14239–14246.
- [60] G. Busse and B. Bullemer. Use of the opto-acoustic effect for rapid scan Fourier spectroscopy. *Infrared Physics* 18.5-6 (1978), 631–634.
- [61] R. S. Wright, G. B. Howe and R. Jayanty. Evaluation of a portable Fourier transform infrared gas analyzer for measurements of air toxics in pollution prevention research. *Journal of the Air & Waste Management Association* 48.11 (1998), 1077–1084.
- [62] J. Uotila and J. Kauppinen. Fourier transform infrared measurement of solid-, liquid-, and gas-phase samples with a single photoacoustic cell. *Applied Spectroscopy* 62.6 (2008), 655–660.
- [63] C. B. Hirschmann, J. Uotila, S. Ojala, J. Tenhunen and R. L. Keiski. Fourier transform infrared photoacoustic multicomponent gas spectroscopy with optical cantilever detection. *Applied Spectroscopy* 64.3 (2010), 293–297.
- [64] C. B. Hirschmann, N. S. Koivikko, J. Raittila, J. Tenhunen, S. Ojala, K. Rahkamaa-Tolonen, R. Marbach, S. Hirschmann and R. L. Keiski. FT-IR-cPAS—new photoacoustic measurement technique for analysis of hot gases: a case study on VOCs. *Sensors* 11.5 (2011), 5270–5289.
- [65] L. Liu, A. Mandelis, A. Melnikov, K. Michaelian, H. Huan and C. Haisch. Step-scan T-cell Fourier transform infrared photoacoustic spectroscopy (FTIR-PAS) for monitoring environmental air pollutants. *International Journal of Thermophysics* 37.7 (2016), 1–9.



- [66] L. Liu, H. Huan, W. Li, A. Mandelis, Y. Wang, L. Zhang, X. Zhang, X. Yin, Y. Wu and X. Shao. Highly sensitive broadband differential infrared photoacoustic spectroscopy with wavelet denoising algorithm for trace gas detection. *Photoacoustics* 21 (2021), 100228.
- [67] J. Karhu, T. Tomberg, F. S. Vieira, G. Genoud, V. Hänninen, M. Vainio and L. Halonen. Broadband photoacoustic spectroscopy of  $^{14}\text{CH}_4$  with a high-power mid-infrared optical frequency comb. *Optics Letters* 44.2 (2019), 1142–1145.
- [68] T. Wildi, T. Voumard, V. Brasch, G. Yilmaz and T. Herr. Photo-acoustic dual-frequency comb spectroscopy. *Nature Communications* 11.1 (2020), 1–6.
- [69] M. Ruiz-Llata, Y. M. Sanoyan, O. E. Bonilla-Manrique, P. Acedo and P. Martin-Mateos. Dual-comb Photoacoustic detection of Ammonia using a resonant acoustic gas cell. *Optical Sensors*. Optica Publishing Group. 2022, SM1E–2.
- [70] X. Ren, M. Yan, Z. Wen, H. Ma, R. Li, K. Huang and H. Zeng. Dual-comb quartz-enhanced photoacoustic spectroscopy. *Photoacoustics* 28 (2022), 100403.
- [71] S. Larnimaa, M. Roiz and M. Vainio. Photoacoustic phase-controlled Fourier-transform infrared spectroscopy. *arXiv preprint arXiv:2212.10084* (2022).
- [72] P. A. Tipler and R. A. Llewellyn. *Modern physics*. WH Freeman and Co., 2012.
- [73] J. M. Hollas. *Modern spectroscopy*. John Wiley & Sons, 2004.
- [74] O. Svelto and D. C. Hanna. *Principles of lasers*. Vol. 4. Springer, 1998.
- [75] L. S. Rothman, I. E. Gordon, Y. Babikov, A. Barbe, D. C. Benner, P. F. Bernath, M. Birk, L. Bizzocchi, V. Boudon, L. R. Brown et al. The HITRAN2012 molecular spectroscopic database. *Journal of Quantitative Spectroscopy and Radiative Transfer* 130 (2013), 4–50.
- [76] A. Shrivastava, V. B. Gupta et al. Methods for the determination of limit of detection and limit of quantitation of the analytical methods. *Chronicles of Young Scientists* 2.1 (2011), 21–25.
- [77] M. Lackner. Tunable diode laser absorption spectroscopy (TDLAS) in the process industries—a review. *Reviews in Chemical Engineering* 23.2 (2007), 65–147.
- [78] P. Werle. A review of recent advances in semiconductor laser based gas monitors. *Spectrochimica Acta Part A: Molecular and Biomolecular Spectroscopy* 54.2 (1998), 197–236.

- [79] D. S. Bomse, A. C. Stanton and J. A. Silver. Frequency modulation and wavelength modulation spectroscopies: comparison of experimental methods using a lead-salt diode laser. *Applied Optics* 31.6 (1992), 718–731.
- [80] M. Vainio and L. Halonen. Mid-infrared optical parametric oscillators and frequency combs for molecular spectroscopy. *Physical Chemistry Chemical Physics* 18.6 (2016), 4266–4294.
- [81] T.-V. Dinh, I.-Y. Choi, Y.-S. Son and J.-C. Kim. A review on non-dispersive infrared gas sensors: Improvement of sensor detection limit and interference correction. *Sensors and Actuators B: Chemical* 231 (2016), 529–538.
- [82] N. Neumann, M. Ebermann, S. Kurth and K. Hiller. Tunable infrared detector with integrated micromachined Fabry-Perot filter. *Journal of Micro/Nanolithography, MEMS, and MOEMS* 7.2 (2008), 021004.
- [83] R. Mukhopadhyay. *Product review: portable FTIR spectrometers get moving*. 2004.
- [84] S. Albert, K. K. Albert and M. Quack. High-resolution Fourier transform infrared spectroscopy. *Handbook of High-resolution Spectroscopy* (2011).
- [85] J. Kauppinen, J. Heinonen and I. Kauppinen. Interferometers based on the rotational motion. *Applied Spectroscopy Reviews* 39.1 (2004), 99–130.
- [86] T.-H. Chao, T. T. Lu, S. R. Davis, S. D. Rommel, G. Farca, B. Luey, A. Martin and M. H. Anderson. Compact liquid crystal waveguide based Fourier transform spectrometer for in-situ and remote gas and chemical sensing. *Optical Pattern Recognition XIX*. Vol. 6977. International Society for Optics and Photonics. 2008, 69770P.
- [87] J. R. Birch. Dispersive Fourier transform spectroscopy. *Microchimica Acta* 93.1-6 (1987), 105–122.
- [88] D. Herriott, H. Kogelnik and R. Kompfner. Off-axis paths in spherical mirror interferometers. *Applied Optics* 3.4 (1964), 523–526.
- [89] C. G. Tarsitano and C. R. Webster. Multilaser Herriott cell for planetary tunable laser spectrometers. *Applied Optics* 46.28 (2007), 6923–6935.
- [90] B. A. Paldus and A. A. Kachanov. An historical overview of cavity-enhanced methods. *Canadian Journal of Physics* 83.10 (2005), 975–999.

- [91] A. Foltynowicz, F. M. Schmidt, W. Ma and O. Axner. Noise-immune cavity-enhanced optical heterodyne molecular spectroscopy: Current status and future potential. *Applied Physics B* 92.3 (2008), 313.
- [92] A. Schliesser, N. Picqué and T. W. Hänsch. Mid-infrared frequency combs. *Nature Photonics* 6.7 (2012), 440–449.
- [93] C. Amiot, A. Aalto, P. Ryczkowski, J. Toivonen and G. Genty. Cavity enhanced absorption spectroscopy in the mid-infrared using a supercontinuum source. *Applied Physics Letters* 111.6 (2017), 061103.
- [94] K. E. Jahromi, M. Nematollahi, Q. Pan, M. A. Abbas, S. M. Cristescu, F. J. Harren and A. Khodabakhsh. Sensitive multi-species trace gas sensor based on a high repetition rate mid-infrared supercontinuum source. *Optics Express* 28.18 (2020), 26091–26101.
- [95] A. Libert, X. Urbain, B. Fabre, M. Daman and C. Lauzin. Design and characteristics of a cavity-enhanced Fourier-transform spectrometer based on a supercontinuum source. *Review of Scientific Instruments* 91.11 (2020), 113104.
- [96] A. Foltynowicz, P. Masłowski, A. J. Fleisher, B. J. Bjork and J. Ye. Cavity-enhanced optical frequency comb spectroscopy in the mid-infrared application to trace detection of hydrogen peroxide. *Applied Physics B* 110.2 (2013), 163–175.
- [97] M. J. Thorpe, K. D. Moll, R. J. Jones, B. Safdi and J. Ye. Broadband cavity ringdown spectroscopy for sensitive and rapid molecular detection. *Science* 311.5767 (2006), 1595–1599.
- [98] M. J. Thorpe, D. Balslev-Clausen, M. S. Kirchner and J. Ye. Cavity-enhanced optical frequency comb spectroscopy: application to human breath analysis. *Optics Express* 16.4 (2008), 2387–2397.
- [99] I. Coddington, N. Newbury and W. Swann. Dual-comb spectroscopy. *Optica* 3.4 (2016), 414–426.
- [100] S. Alexandrov, G. A. Gavrilov, A. Kapralov, S. A. Karandashev, B. A. Matveev, G. Y. Sotnikova and N. M. Stus. Portable optoelectronic gas sensors operating in the mid-IR spectral range ( $\lambda = 3.5 \mu\text{m}$ ). *Second International Conference on Lasers for Measurement and Information Transfer*. Vol. 4680. International Society for Optics and Photonics. 2002, 188–194.

- [101] R. W. Boyd. *Nonlinear optics*. Academic press, 2003.
- [102] C. Kaminski, R. Watt, A. Elder, J. Frank and J. Hult. Supercontinuum radiation for applications in chemical sensing and microscopy. *Applied Physics B* 92.3 (2008), 367–378.
- [103] G. Genty, S. Coen and J. M. Dudley. Fiber supercontinuum sources. *JOSA B* 24.8 (2007), 1771–1785.
- [104] M. A. Solodyankin, E. D. Obraztsova, A. S. Lobach, A. I. Chernov, A. V. Tausenev, V. I. Konov and E. M. Dianov. Mode-locked 1.93  $\mu\text{m}$  thulium fiber laser with a carbon nanotube absorber. *Optics Letters* 33.12 (2008), 1336–1338.
- [105] S. B. Mirov, V. Fedorov, D. Martyshkin, I. Moskalev, M. Mirov and V. Gaponsev. Progress in mid-IR Cr 2+ and Fe 2+ doped II-VI materials and lasers. *Optical Materials Express* 1.5 (2011), 898–910.
- [106] A. Hugi, G. Villares, S. Blaser, H. Liu and J. Faist. Mid-infrared frequency comb based on a quantum cascade laser. *Nature* 492.7428 (2012), 229–233.
- [107] L. A. Sterczewski, J. Westberg, M. Bagheri, C. Frez, I. Vurgaftman, C. L. Canedy, W. W. Bewley, C. D. Merritt, C. S. Kim, M. Kim et al. Mid-infrared dual-comb spectroscopy with interband cascade lasers. *Optics Letters* 44.8 (2019), 2113–2116.
- [108] A. G. Griffith, R. K. Lau, J. Cardenas, Y. Okawachi, A. Mohanty, R. Fain, Y. H. D. Lee, M. Yu, C. T. Phare, C. B. Poitras et al. Silicon-chip mid-infrared frequency comb generation. *Nature Communications* 6.1 (2015), 1–5.
- [109] F. J. M. Harren, G. Cotti, J. Oomens and S. te Lintel Hekkert. Photoacoustic spectroscopy in trace gas monitoring. *Encyclopedia of Analytical Chemistry* 3 (2000), 2203–2226.
- [110] A. G. Bell. Upon the production of sound by radiant energy. *The London, Edinburgh, and Dublin Philosophical Magazine and Journal of Science* 11.71 (1881), 510–528. URL: <https://doi.org/10.1080/14786448108627053>.
- [111] M. L. Viegrov. Eine Methode der Gasanalyse, Beruhend auf der Optisch-Akustischen Tyndall-Röntgenerscheinung. German. *Dokl. Akad. Nauk SSSR* 19 (1938), 687–688.

- [112] Z. Bozóki, A. Pogány and G. Szabó. Photoacoustic instruments for practical applications: present, potentials, and future challenges. *Applied Spectroscopy Reviews* 46.1 (2011), 1–37.
- [113] M. Xu and L. V. Wang. Photoacoustic imaging in biomedicine. *Review of Scientific Instruments* 77.4 (2006), 041101.
- [114] J. Li, W. Chen and B. Yu. Recent Progress on Infrared Photoacoustic Spectroscopy Techniques. *Applied Spectroscopy Reviews* 46.6 (2011), 440–471.
- [115] M. Müller, T. Rück, S. Jobst, J. Pangerl, S. Weigl, R. Bierl and F.-M. Matysik. An algorithmic approach to compute the effect of non-radiative relaxation processes in photoacoustic spectroscopy. *Photoacoustics* (2022), 100371.
- [116] S. D. Russo, A. Sampaolo, P. Patimisco, G. Menduni, M. Giglio, C. Hoelzl, V. M. Passaro, H. Wu, L. Dong and V. Spagnolo. Quartz-enhanced photoacoustic spectroscopy exploiting low-frequency tuning forks as a tool to measure the vibrational relaxation rate in gas species. *Photoacoustics* 21 (2021), 100227.
- [117] J. Peltola, T. Hieta and M. Vainio. Parts-per-trillion-level detection of nitrogen dioxide by cantilever-enhanced photo-acoustic spectroscopy. *Optics Letters* 40.13 (2015), 2933–2936.
- [118] T. Laurila, H. Cattaneo, T. Pöyhönen, V. Koskinen, J. Kauppinen and R. Hernberg. Cantilever-based photoacoustic detection of carbon dioxide using a fiber-amplified diode laser. *Applied Physics B* 83.2 (2006), 285–288.
- [119] T. Kuusela and J. Kauppinen. Photoacoustic gas analysis using interferometric cantilever microphone. *Applied Spectroscopy Reviews* 42.5 (2007), 443–474.
- [120] J. Peltola, M. Vainio, T. Hieta, J. Uotila, S. Sinisalo, M. Metsälä, M. Siltanen and L. Halonen. High sensitivity trace gas detection by cantilever-enhanced photoacoustic spectroscopy using a mid-infrared continuous-wave optical parametric oscillator. *Optics Express* 21.8 (2013), 10240–10250.
- [121] A. Elia, P. M. Lugarà, C. Di Franco and V. Spagnolo. Photoacoustic techniques for trace gas sensing based on semiconductor laser sources. *Sensors* 9.12 (2009), 9616–9628.

- [122] V. Spagnolo, P. Patimisco, S. Borri, G. Scamarcio, B. E. Bernacki and J. Kriesel. Part-per-trillion level SF<sub>6</sub> detection using a quartz enhanced photoacoustic spectroscopy-based sensor with single-mode fiber-coupled quantum cascade laser excitation. *Optics Letters* 37.21 (2012), 4461–4463.
- [123] A. Manninen, B. Tuzson, H. Looser, Y. Bonetti and L. Emmenegger. Versatile multipass cell for laser spectroscopic trace gas analysis. *Applied Physics B* 109.3 (2012), 461–466.
- [124] A. Miklós, S.-C. Pei and A. Kung. Multipass acoustically open photoacoustic detector for trace gas measurements. *Applied Optics* 45.11 (2006), 2529–2534.
- [125] K. Krzempek, A. Hudzikowski, A. Głuszek, G. Dudzik, K. Abramski, G. Wysocki and M. Nikodem. Multi-pass cell-assisted photoacoustic/photothermal spectroscopy of gases using quantum cascade laser excitation and heterodyne interferometric signal detection. *Applied Physics B* 124.5 (2018), 74.
- [126] B. Zhang, K. Chen, Y. Chen, B. Yang, M. Guo, H. Deng, F. Ma, F. Zhu, Z. Gong, W. Peng and Q. Yu. High-sensitivity photoacoustic gas detector by employing multi-pass cell and fiber-optic microphone. *Optics Express* 28.5 (2020), 6618–6630.
- [127] S. Borri, P. Patimisco, I. Galli, D. Mazzotti, G. Giusfredi, N. Akikusa, M. Yamanishi, G. Scamarcio, P. De Natale and V. Spagnolo. Intracavity quartz-enhanced photoacoustic sensor. *Applied Physics Letters* 104.9 (2014), 091114.
- [128] T. Tomberg, T. Hieta, M. Vainio and L. Halonen. Cavity-enhanced cantilever-enhanced photo-acoustic spectroscopy. *Analyst* (2019).
- [129] J. B. Mehl and M. R. Moldover. Precision acoustic measurements with a spherical resonator: Ar and C<sub>2</sub>H<sub>4</sub>. *The Journal of Chemical Physics* 74.7 (1981), 4062–4077.
- [130] S. L. Firebaugh, K. F. Jensen and M. A. Schmidt. Miniaturization and integration of photoacoustic detection. *Journal of Applied Physics* 92.3 (2002), 1555–1563.
- [131] R. Lindley, A. Parkes, K. Keen, E. McNaghten and A. Orr-Ewing. A sensitivity comparison of three photoacoustic cells containing a single microphone, a differential dual microphone or a cantilever pressure sensor. *Applied Physics B* 86.4 (2007), 707–713.

- [132] T. Laurila, H. Cattaneo, V. Koskinen, J. Kauppinen and R. Hernberg. Diode laser-based photoacoustic spectroscopy with interferometrically-enhanced cantilever detection. *Optics Express* 13.7 (2005), 2453–2458.
- [133] Y. Ma, S. Qiao, Y. He, Y. Li, Z. Zhang, X. Yu and F. K. Tittel. Highly sensitive acetylene detection based on multi-pass retro-reflection-cavity-enhanced photoacoustic spectroscopy and a fiber amplified diode laser. *Optics Express* 27.10 (2019), 14163–14172.
- [134] F. Harren, F. Bijnen, J. Reuss, L. Voesenek and C. Blom. Sensitive intracavity photoacoustic measurements with a CO<sub>2</sub> waveguide laser. *Applied Physics B* 50.2 (1990), 137–144.
- [135] L. Zhang, L. Liu, Y. Liu, X. Zhang, H. Huan, X. Yin, T. Xi and X. Shao. Advances in differential photoacoustic spectroscopy for trace gas detection. *Microwave and Optical Technology Letters* (2022).
- [136] A. Miklós, P. Hess and Z. Bozóki. Application of acoustic resonators in photoacoustic trace gas analysis and metrology. *Review of Scientific Instruments* 72.4 (2001), 1937–1955.
- [137] A. Miklós, P. Hess, A. Mohácsi, J. Sneider, S. Kamm and S. Schäfer. Photoacoustic and Photothermal Phenomena: 10th International Conference, edited by F. Scudieri and M. Bertolotti AIP, Woodbury, NY (1999), 126.
- [138] S. Alahmari, X.-W. Kang and M. Hippler. Diode laser photoacoustic spectroscopy of CO<sub>2</sub>, H<sub>2</sub>S and O<sub>2</sub> in a differential Helmholtz resonator for trace gas analysis in the biosciences and petrochemistry. *Analytical and Bioanalytical Chemistry* 411.17 (2019), 3777–3787.
- [139] J. Uotila, V. Koskinen and J. Kauppinen. Selective differential photoacoustic method for trace gas analysis. *Vibrational Spectroscopy* 38.1-2 (2005), 3–9.
- [140] K. Song, H. Cha, V. Kapitanov, Y. N. Ponomarev, A. Rostov, D. Courtois, B. Parvitte and V. Zeninari. Differential Helmholtz resonant photoacoustic cell for spectroscopy and gas analysis with room-temperature diode lasers. *Applied Physics B* 75.2 (2002), 215–227.
- [141] V. Zeninari, V. Kapitanov, D. Courtois and Y. N. Ponomarev. Design and characteristics of a differential Helmholtz resonant photoacoustic cell for infrared gas detection. *Infrared Physics & Technology* 40.1 (1999), 1–23.

- [142] J. Rey and M. Sigrist. Differential mode excitation photoacoustic spectroscopy: A new photoacoustic detection scheme. *Review of Scientific Instruments* 78.6 (2007), 063104.
- [143] S. S. Choi, A. Mandelis, X. Guo, B. Lashkari, S. Kellnberger and V. Ntziachristos. Wavelength-Modulated Differential Photoacoustic Spectroscopy (WM-DPAS) for noninvasive early cancer detection and tissue hypoxia monitoring. *Spectrochimica Acta Part A: Molecular and Biomolecular Spectroscopy* 168.2 (2016), 29–36.
- [144] S. Park and G. Diebold. Interferometric microphone for optoacoustic spectroscopy. *Review of Scientific Instruments* 58.5 (1987), 772–775.
- [145] M. H. De Paula, A. R. Omido, D. F. d. Q. Schumacher and H. H. Da Gama. Optical microphone: New results. *Review of Scientific Instruments* 75.9 (2004), 2863–2864.
- [146] A. A. Kosterev, Y. A. Bakirkin, R. F. Curl and F. K. Tittel. Quartz-enhanced photoacoustic spectroscopy. *Optics Letters* 27.21 (2002), 1902–1904.
- [147] S. D. Russo, S. Zhou, A. Zifarelli, P. Patimisco, A. Sampaolo, M. Giglio, D. Iannuzzi and V. Spagnolo. Photoacoustic spectroscopy for gas sensing: A comparison between piezoelectric and interferometric readout in custom quartz tuning forks. *Photoacoustics* 17 (2020), 100155.
- [148] N. Ledermann, J. Baborowski, A. Seifert, B. Willing, S. Hiboux, P. Muralt, N. Setter and M. Forster. Piezoelectric cantilever microphone for photoacoustic gas detector. *Integrated Ferroelectrics* 35.1-4 (2001), 177–184.
- [149] K. Wilcken and J. Kauppinen. Optimization of a microphone for photoacoustic spectroscopy. *Applied Spectroscopy* 57.9 (2003), 1087–1092.
- [150] K. Liu, Y. Cao, G. Wang, W. Zhang, W. Chen and X. Gao. A novel photoacoustic spectroscopy gas sensor using a low cost polyvinylidene fluoride film. *Sensors and Actuators B: Chemical* 277 (2018), 571–575.
- [151] T. Yang, W. Chen and P. Wang. A review of all-optical photoacoustic spectroscopy as a gas sensing method. *Applied Spectroscopy Reviews* 56.2 (2021), 143–170.



- [152] A. Manninen, J. Sand, J. Saarela, T. Sorvajärvi, J. Toivonen and R. Hernberg. Electromechanical film as a photoacoustic transducer. *Optics Express* 17.19 (2009), 16994–16999.
- [153] P. Patimisco, A. Sampaolo, H. Zheng, L. Dong, F. K. Tittel and V. Spagnolo. Quartz-enhanced photoacoustic spectrophones exploiting custom tuning forks: a review. *Advances in Physics: X* 2.1 (2017), 169–187.
- [154] V. Koskinen, J. Fonsen, K. Roth and J. Kauppinen. Progress in cantilever enhanced photoacoustic spectroscopy. *Vibrational Spectroscopy* 48.1 (2008), 16–21.
- [155] M. Giglio, P. Patimisco, A. Sampaolo, A. Zifarelli, R. Blanchard, C. Pfluegl, M. F. Witinski, D. Vakhshoori, F. K. Tittel and V. Spagnolo. Nitrous oxide quartz-enhanced photoacoustic detection employing a broadband distributed-feedback quantum cascade laser array. *Applied Physics Letters* 113.17 (2018), 171101.
- [156] T. Kuusela, J. Peura, B. Matveev, M. Remennyy et al. Photoacoustic gas detection using a cantilever microphone and III–V mid-IR LEDs. *Vibrational Spectroscopy* 51.2 (2009), 289–293.
- [157] J. Fonsen, V. Koskinen, K. Roth and J. Kauppinen. Dual cantilever enhanced photoacoustic detector with pulsed broadband IR-source. *Vibrational Spectroscopy* 50.2 (2009), 214–217.
- [158] J. Kopaczek, S. Zelewski and R. Kudrawiec. Supercontinuum source as a probing beam in photoreflectance and photoacoustic spectroscopy. *Measurement* 146 (2019), 879–884.
- [159] H. Wu, X. Yin, L. Dong, K. Pei, A. Sampaolo, P. Patimisco, H. Zheng, W. Ma, L. Zhang, W. Yin et al. Simultaneous dual-gas QEPAS detection based on a fundamental and overtone combined vibration of quartz tuning fork. *Applied Physics Letters* 110.12 (2017), 121104.
- [160] K. Liu, J. Mei, W. Zhang, W. Chen and X. Gao. Multi-resonator photoacoustic spectroscopy. *Sensors and Actuators B: Chemical* 251.7 (2017), 632–636.
- [161] M. M. Farrow, R. K. Burnham and E. M. Eyring. Fourier-transform photoacoustic spectroscopy. *Applied Physics Letters* 33.8 (1978), 735–737.

- [162] M. G. Rockley. Fourier-transformed infrared photoacoustic spectroscopy of polystyrene film. *Chemical Physics Letters* 68.2-3 (1979), 455–456.
- [163] G. Zachmann. FT-IR spectroscopy of solid surfaces. *Journal of Molecular Structure* 115 (1984), 465–468.
- [164] J. Irudayaraj, H. Yang and S. Sakhamuri. Differentiation and detection of microorganisms using Fourier transform infrared photoacoustic spectroscopy. *Journal of Molecular Structure* 606.1-3 (2002), 181–188.
- [165] C. Du, J. Zhou, H. Wang, X. Chen, A. Zhu and J. Zhang. Determination of soil properties using Fourier transform mid-infrared photoacoustic spectroscopy. *Vibrational Spectroscopy* 49.1 (2009), 32–37.
- [166] G. Bekiaris, C. Peltre, L. S. Jensen and S. Bruun. Using FTIR-photoacoustic spectroscopy for phosphorus speciation analysis of biochars. *Spectrochimica Acta Part A: Molecular and Biomolecular Spectroscopy* 168.2 (2016), 29–36.
- [167] J. J. Mikkonen, J. Raittila, L. Rieppo, R. Lappalainen, A. M. Kullaa and S. Myllymaa. Fourier transform infrared spectroscopy and photoacoustic spectroscopy for saliva analysis. *Applied Spectroscopy* 70.9 (2016), 1502–1510.
- [168] J. Kauppinen and J. Partanen. *Fourier transforms in spectroscopy*. John Wiley & Sons, 2001.
- [169] D. A. Naylor and M. K. Tahic. Apodizing functions for Fourier transform spectroscopy. *JOSA A* 24.11 (2007), 3644–3648.
- [170] A. Khodabakhsh, V. Ramaiah-Badarla, L. Rutkowski, A. C. Johansson, K. F. Lee, J. Jiang, C. Mohr, M. E. Fermann and A. Foltynowicz. Fourier transform and Vernier spectroscopy using an optical frequency comb at 3–5.4  $\mu\text{m}$ . *Optics Letters* 41.11 (2016), 2541–2544.
- [171] M. Szakáll, J. Csikós, Z. Bozóki and G. Szabó. On the temperature dependent characteristics of a photoacoustic water vapor detector for airborne application. *Infrared Physics & Technology* 51.2 (2007), 113–121.
- [172] F. Plankey, T. Glenn, L. Hart and J. Winefordner. Hadamard spectrometer for ultraviolet-visible spectrometry. *Analytical Chemistry* 46.8 (1974), 1000–1005.
- [173] T. Hirschfeld. The implications of fluctuation noise in multiplex spectroscopy. *Applied Spectroscopy* 30.2 (1976), 234–236.

- [174] A. Foltynowicz, T. Ban, P. Masłowski, F. Adler and J. Ye. Quantum-noise-limited optical frequency comb spectroscopy. *Physical Review Letters* 107.23 (2011), 233002.
- [175] J. Karhu, H. Philip, A. Baranov, R. Teissier and T. Hieta. Sub-ppb detection of benzene using cantilever-enhanced photoacoustic spectroscopy with a long-wavelength infrared quantum cascade laser. *Optics Letters* 45.21 (2020), 5962–5965.
- [176] C. Hill, I. E. Gordon, R. V. Kochanov, L. Barrett, J. S. Wilzewski and L. S. Rothman. HITRANOnline: An online interface and the flexible representation of spectroscopic data in the HITRAN database. *Journal of Quantitative Spectroscopy and Radiative Transfer* 177 (2016), 4–14.
- [177] P. Werle, R. Mücke and F. Slemr. The limits of signal averaging in atmospheric trace-gas monitoring by tunable diode-laser absorption spectroscopy (TDLAS). *Applied Physics B* 57.2 (1993), 131–139.
- [178] Official Journal of the European Communities. *Council Directive 1999/13/EC of 11 March 1999 on the limitation of emissions of volatile organic compounds due to the use of organic solvents in certain activities and installations*. (Accessed 3 August 2022). 1999. URL: <https://eur-lex.europa.eu/legal-content/EN/TXT/?uri=CELEX:31999L0013>.
- [179] G. A. Olah and Á. Molnár. *Hydrocarbon chemistry*. John Wiley & Sons, 2003.
- [180] J. M. Rey, M. Fill, F. Felder and M. W. Sigrist. Broadly tunable mid-infrared VECSEL for multiple components hydrocarbon gas sensing. *Applied Physics B* 117.3 (2014), 935–939.
- [181] K. Zhang and S. Batterman. Air pollution and health risks due to vehicle traffic. *Science of the Total Environment* 450 (2013), 307–316.
- [182] S. Bustamante, M. Manana, A. Arroyo, P. Castro, A. Laso and R. Martinez. Dissolved gas analysis equipment for online monitoring of transformer oil: A review. *Sensors* 19.19 (2019), 4057.
- [183] A. R. Moot, K. M. Ledingham, P. F. Wilson, S. T. Senthilmohan, D. R. Lewis, J. Roake and R. Allardyce. Composition of volatile organic compounds

- in diathermy plume as detected by selected ion flow tube mass spectrometry. *ANZ Journal of Surgery* 77.1-2 (2007), 20–23.
- [184] Y.-W. Lin, S.-Z. Fan, K.-H. Chang, C.-S. Huang and C.-S. Tang. A novel inspection protocol to detect volatile compounds in breast surgery electrocautery smoke. *Journal of the Formosan Medical Association* 109.7 (2010), 511–516.
  - [185] J. Balog, L. Sasi-Szabó, J. Kinross, M. R. Lewis, L. J. Muirhead, K. Veselkov, R. Mirnezami, B. Dezső, L. Damjanovich, A. Darzi et al. Intraoperative tissue identification using rapid evaporative ionization mass spectrometry. *Science Translational Medicine* 5.194 (2013), 194ra93–194ra93.
  - [186] A. Kontunen, M. Karjalainen, A. Anttalainen, O. Anttalainen, M. Koskenranta, A. Vehkaoja, N. Oksala and A. Roine. Real time tissue identification from diathermy smoke by differential mobility spectrometry. *IEEE Sensors Journal* 21.1 (2020), 717–724.
  - [187] S. Chauhan, R. D’cruz, S. Faruqi, K. Singh, S. Varma, M. Singh and V. Karthik. Chemical warfare agents. *Environmental Toxicology and Pharmacology* 26.2 (2008), 113–122.
  - [188] D. D. Haines and S. C. Fox. Acute and long-term impact of chemical weapons: lessons from the Iran-Iraq war. *Forensic Science Review* 26.2 (2014), 97–114.
  - [189] United Nations. *Report of the United Nations Mission to Investigate Allegations of the Use of Chemical Weapons in the Syrian Arab Republic on the alleged use of chemical weapons in the Ghouta area of Damascus on 21 August 2013*. (Accessed 22 September 2021). 2013. URL: <https://www.un.org/zh/focus/northafrica/cwinvestigation.pdf>.
  - [190] R. Pita and J. Domingo. The use of chemical weapons in the Syrian conflict. *Toxics* 2.3 (2014), 391–402.
  - [191] Y. Seto, N. Tsunoda, M. Kataoka, K. Tsuge and T. Nagano. Toxicological analysis of victims’ blood and crime scene evidence samples in the sarin gas attack caused by the Aum Shinrikyo cult. ACS Publications, 2000. Chap. 21, 318–332.

- [192] T. Okumura, N. Takasu, S. Ishimatsu, S. Miyanoki, A. Mitsuhashi, K. Kumada, K. Tanaka and S. Hinohara. Report on 640 victims of the Tokyo subway sarin attack. *Annals of Emergency Medicine* 28.2 (1996), 129–135.
- [193] Organisation for the Prohibition of Chemical Weapons. *Summary of the report on activities carried out in support of a request for technical assistance by the United Kingdom of Great Britain and Northern Ireland*. (Accessed 23 September 2021). 2018. URL: [https://www.opcw.org/sites/default/files/documents/S\\_series/2018/en/s-1612-2018\\_e\\_\\_1\\_.pdf](https://www.opcw.org/sites/default/files/documents/S_series/2018/en/s-1612-2018_e__1_.pdf).
- [194] J. A. Vale, T. C. Marrs and R. L. Maynard. Novichok: a murderous nerve agent attack in the UK. *Clinical Toxicology* 56.11 (2018), 1093–1097.
- [195] Organisation for the Prohibition of Chemical Weapons. *Summary of the report on activities carried out in support of a request for technical assistance by Germany*. (Accessed 23 September 2021). 2018. URL: <https://www.opcw.org/documents/2020/10/s19062020/note-technical-secretariat-summary-report-activities-carried-out>.
- [196] G. Liu and Y. Lin. Electrochemical sensor for organophosphate pesticides and nerve agents using zirconia nanoparticles as selective sorbents. *Analytical Chemistry* 77.18 (2005), 5894–5901.
- [197] C. E. Davidson, M. M. Dixon, B. R. Williams, G. K. Kilper, S. H. Lim, R. A. Martino, P. Rhodes, M. S. Hulet, R. W. Miles, A. C. Samuels et al. Detection of chemical warfare agents by colorimetric sensor arrays. *ACS Sensors* 5.4 (2020), 1102–1109.
- [198] M. S. J. Khan, Y.-W. Wang, M. O. Senge and Y. Peng. Sensitive fluorescence on-off probes for the fast detection of a chemical warfare agent mimic. *Journal of Hazardous Materials* 342 (2018), 10–19.
- [199] W. Meng, Z. Pei, Y. Wang, M. Sun, Q. Xu, J. Cen, K. Guo, K. Xiao and Z. Li. Two birds with one stone: The detection of nerve agents and AChE activity with an ICT-ESIPT-based fluorescence sensor. *Journal of Hazardous Materials* 410 (2021), 124811.
- [200] J. Kim, E. Kim, J. Kim, J.-H. Kim, S. Ha, C. Song, W. J. Jang and J. Yun. Four-Channel Monitoring System with Surface Acoustic Wave Sensors for Detection of Chemical Warfare Agents. *Journal of Nanoscience and Nanotechnology* 20.11 (2020), 7151–7157.

- [201] J. Puton and J. Namieśnik. Ion mobility spectrometry: Current status and application for chemical warfare agents detection. *TrAC Trends in Analytical Chemistry* 85 (2016), 10–20.
- [202] P. A. Smith, D. Koch, G. L. Hook, R. P. Erickson, C. R. J. Lepage, H. D. Wyatt, G. Betsinger and B. A. Eckenrode. Detection of gas-phase chemical warfare agents using field-portable gas chromatography–mass spectrometry systems: instrument and sampling strategy considerations. *TrAC Trends in Analytical Chemistry* 23.4 (2004), 296–306.
- [203] M. Lafuente, D. Sanz, M. Urbiztondo, J. Santamaria, M. P. Pina and R. Malada. Gas phase detection of chemical warfare agents CWAs with portable Raman. *Journal of Hazardous Materials* 384 (2020), 121279.
- [204] A. Mukherjee, I. Dunayevskiy, M. Prasanna, R. Go, A. Tsekoun, X. Wang, J. Fan and C. K. N. Patel. Sub-parts-per-billion level detection of dimethyl methyl phosphonate (DMMP) by quantum cascade laser photoacoustic spectroscopy. *Applied Optics* 47.10 (2008), 1543–1548.
- [205] K. P. Gurton, M. Felton and R. Tober. Selective real-time detection of gaseous nerve agent simulants using multiwavelength photoacoustics. *Optics Letters* 37.16 (2012), 3474–3476.
- [206] J.-M. Melkonian, J. Armougom, M. Raybaut, J.-B. Dherbecourt, G. Gorju, N. Cézard, A. Godard, V. Pašiškevičius, R. Coetzee and J. Kadlčák. Long-wave infrared multi-wavelength optical source for standoff detection of chemical warfare agents. *Applied Optics* 59.35 (2020), 11156–11166.
- [207] D. Levy. Advances in portable FTIR spectrometers for the field: the HazMatID Ranger. *Next-Generation Spectroscopic Technologies II*. Vol. 7319. International Society for Optics and Photonics. 2009, 73190E.
- [208] Y. Ohru, R. Hashimoto, T. Ohmori, Y. Seto, H. Inoue, H. Nakagaki, K. Yoshikawa and L. McDermott. Continuous monitoring of chemical warfare agents in vapor using a Fourier transform infra-red spectroscopy instrument with multi pass gas cell, mercury cadmium telluride detector and rolling background algorithm. *Forensic Chemistry* 21 (2020), 100292.
- [209] S. Neupane, R. Peale and S. Vasu. Infrared absorption cross sections of several organo-phosphorous chemical-weapon simulants. *Journal of Molecular Spectroscopy* 355 (2019), 59–65.

- [210] S. W. Sharpe, T. J. Johnson, P. M. Chu, J. Kleimeyer and B. Rowland. Quantitative infrared spectra of vapor phase chemical agents. *Chemical and Biological Sensing IV*. Vol. 5085. International Society for Optics and Photonics. 2003, 19–27.
- [211] MKS Instruments. *MultiGas<sup>TM</sup> FTIR Gas Analyzer, Model 2031*. (Accessed 22 September 2022). 2021. URL: <https://www.mks.com/p/MULTIGAS-2031>.
- [212] H.-J. Quenzer, S. Gu-Stoppel, F. Stoppel, J. Janes, U. Hofmann and W. Bencke. Piezoelectrically driven translatory optical MEMS actuator with 7mm apertures and large displacements. *MOEMS and Miniaturized Systems XIV*. Vol. 9375. SPIE. 2015, 156–162.
- [213] A. Kenda, M. Kraft, A. Tortschanoff, W. Scherf, T. Sandner, H. Schenk, S. Luetjohann and A. Simon. Development, characterization and application of compact spectrometers based on MEMS with in-plane capacitive drives. *Next-Generation Spectroscopic Technologies VII*. Vol. 9101. SPIE. 2014, 910102.
- [214] H. R. Seren, S. Holmstrom, N. P. Ayerden, J. Sharma and H. Urey. Lamellar-grating-based MEMS Fourier transform spectrometer. *Journal of Microelectromechanical Systems* 21.2 (2012), 331–339.
- [215] T. Tanahashi, M. Toda, H. Miyashita and T. Ono. Miniature Fourier transform infrared spectrometer for middle infrared wavelength range. *2013 Transducers & Eurosensors XXVII: The 17th International Conference on Solid-State Sensors, Actuators and Microsystems (TRANSDUCERS & EUROSENSORS XXVII)*. IEEE. 2013, 2509–2512.
- [216] F. Han, W. Wang, X. Zhang and H. Xie. Miniature Fourier transform spectrometer with a dual closed-loop controlled electrothermal micromirror. *Optics Express* 24.20 (2016), 22650–22660.
- [217] W. Wang, J. Chen, A. S. Zivkovic and H. Xie. A Fourier Transform Spectrometer based on an electrothermal MEMS mirror with improved linear scan range. *Sensors* 16.10 (2016), 1611.





## PUBLICATIONS



# PUBLICATION

I

## **Broadband cantilever-enhanced photoacoustic spectroscopy in the mid-IR using a supercontinuum**

T. Mikkonen, C. Amiot, A. Aalto, K. Patokoski, G. Genty and J. Toivonen

*Optics Letters* 43.20 (2018), 5094–5097

**Publication reprinted with the permission of the copyright holders**



# Broadband cantilever-enhanced photoacoustic spectroscopy in the mid-IR using a supercontinuum

TOMMI MIKKONEN<sup>1,\*</sup>, CAROLINE AMIOT<sup>1,2</sup>, ANTTI AALTO<sup>1</sup>, KIM PATOKOSKI<sup>1</sup>, GOËRY GENTY<sup>1</sup>, AND JUHA TOIVONEN<sup>1</sup>

<sup>1</sup>Laboratory of Photonics, Tampere University of Technology, Tampere, Finland

<sup>2</sup>Institut FEMTO-ST, UMR 6174 CNRS, Université de Bourgogne Franche-Comté, Besançon, France

\*Corresponding author: [tommi.j.mikkonen@tut.fi](mailto:tommi.j.mikkonen@tut.fi)

Compiled August 30, 2018

**We demonstrate cantilever-enhanced photoacoustic spectroscopy in the mid-infrared using a supercontinuum source. The approach is broadband and allows for higher photoacoustic signal intensity and enhanced signal-to-noise ratio as compared to systems employing conventional black body radiation sources. Using this technique, we perform spectroscopic measurements of the full ro-vibrational band structure of water vapor at 1900 nm and methane at 3300 nm with relative signal enhancement factors of 70 and 19, respectively, when compared to measurements that use a black body radiation source. Our results offer novel perspective for photoacoustic detection opening the door to sensitive broadband analyzers in the mid-infrared spectral region.**

© 2018 Optical Society of America

**OCIS codes:** (320.6629) Supercontinuum generation; (110.5125) Photoacoustics.

<http://dx.doi.org/10.1364/ol.XX.XXXXXX>

Photoacoustic spectroscopy (PAS) is an optical sensing technique that detects the pressure wave resulting from local heating and thermal expansion when light is absorbed by a gas sample placed inside an acoustic cell. Photoacoustic spectroscopy with high-power lasers is particularly attractive as the signal detected by a pressure-sensitive detector is directly proportional to the absorbed light power, resulting in highly sensitive background-free measurements. Another significant advantage of PAS is the small volume of gas sample required which makes it generally more compact than e.g. conventional Fourier transform infrared spectrometers (FTIRs) [1]. Microphones with electrical readout are commonly used as detectors in PAS, however their sensitivity is limited by the electrical noise. Resonant acoustic cells are therefore often needed for high sensitivity measurements, which limits the detection to a single modulation frequency. By replacing the microphone with a micromechanical cantilever whose mechanical oscillations are detected with an optical interferometer, acoustic resonance enhancement is not required, either from the cell or from the cantilever, allowing for broadband detection with similar sensitivities [2] and indeed sub-ppt sensitivities have been reported using such a cantilever enhanced photoa-

coustic spectroscopy approach (CEPAS) [3].

Various types of light sources have been used in laser based PAS systems, including distributed feedback diode lasers [4, 5] and external cavity diode lasers [6] in the near-infrared, or quantum cascade laser [7, 8] and optical parametric oscillators [9] in the mid-infrared. These sources are inherently narrowband or they have a limited wavelength-tuning range. Broadband detection may be achieved using thermal emitters or black body radiators [1, 10] but their low brightness limits the sensitivity in this case. Supercontinuum (SC) sources on the other hand can exhibit extremely broad bandwidth with brightness exceeding by orders of magnitude that of thermal emitters and the unique properties of SC sources have made them ideal light sources candidates for many sensing and imaging applications including spectroscopy, microscopy or optical coherence tomography [11–15]. In this Letter, combining a broadband supercontinuum source with FTIR CEPAS, we demonstrate sensitive, broadband photoacoustic detection of water vapor and methane in the mid-infrared spectral region. Our results show a significant increase in the signal intensity as compared to when using a thermal emitter. A significant advantage of the fiber-based SC source is its high spatial coherence allowing for (1) a much larger power spectral density in the FTIR as compared to blackbody radiators and (2) adjustment of the FTIR beam path and tuning the resolution of the measurement. Our results open up new perspectives for gas sensing and, more generally, spectroscopic applications using broadband photoacoustic detection.

Our experimental setup is shown in Fig. 1. The supercontinuum source is generated by injecting 0.6 ns pulses at 1547 nm from a gain-switched fiber laser (Keopsys-PEFL-K09) with tunable repetition rate into the anomalous dispersion regime of a 4-m-long silica dispersion-shifted fiber (DSF, Corning Inc LEAF) followed by an 8 m long fluoride fiber (ZBLAN) as described in [12]. Here, depending on the gas sample to be characterized, we used different repetition rate for the pump laser so as to optimize the power spectral density of the SC in the spectral range of interest. Specifically, for a repetition rate of 70 kHz, the 10 kW peak power of the pump laser pulses leads to the generation of a broadband SC extending from c.a. 1500 nm up to c.a. 3700 nm as the result of multiple cascaded nonlinear dynamics including modulation instability, soliton formation and Raman self-frequency shift [16]. When the repetition rate is increased

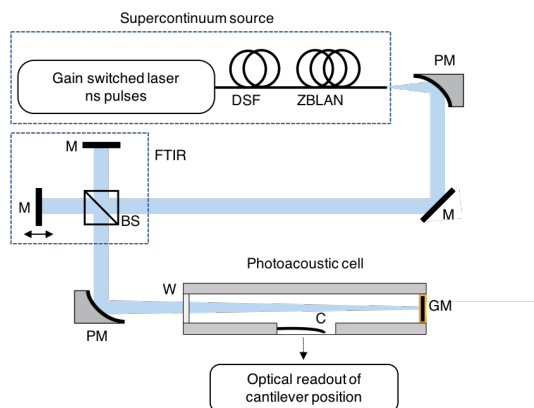


**Fig. 1.** Experimental setup. PM, off-axis parabolic mirror; M, mirror; BS, beam splitter; W, window; GM, gold mirror; C, cantilever.

to 400 kHz, the peak power of the pump pulses is reduced to less than 2 kW and the spectrum extends from 1500 nm up to 2400 nm. The average SC spectra measured with a scanning monochromator and corresponding to 70 kHz and 400 kHz repetition rates for the pump laser are shown in Fig. 2 as the blue and red solid lines, respectively. Note that in the 70 kHz repetition rate case, the short wavelengths side of the SC spectrum was limited using a long-pass filter (Northumbria Optical Coating, SLWP-2337) with a cut-on wavelength of 2300 nm. The spectral filter was used to remove the excess noise of the SC source in the 1900 nm band at a lower repetition rate. Note that the sharp features observed at around 2600 nm in the average spectrum obtained for a 70 kHz repetition rate are caused by water vapor absorption present in air. A half-a-meter monochromator (Spectral Products DK480 1/2) was used to measure the SC spectra with a maximal resolution of 1 nm, and a lock-in amplifier (PerkinElmer 7225) was used to increase the signal-to-noise ratio (SNR).

Light from the SC is collimated into a 2 mm (diameter) beam using a silver reflective collimator and sent to a scanning FTIR interferometer (Bruker IRCube) modulating the spectrum of the light source. For comparison, we also perform reference measurements that use a black body source having a beam diameter of 25 mm are performed with the same FTIR instrument. The order of magnitude smaller beam size of the collimated SC source demonstrates the future potential in miniaturizing the FTIR scanning instrument when used with a spatially coherent light source. At the FTIR output the beam is focused with a parabolic mirror ( $f = 76.2$  mm) into a non-resonant photoacoustic cell (Gaser) that contains the gas sample to be measured. The cell is gold-coated, 10 cm long and 4.5 mm diameter corresponding to a sample volume smaller than 8 mL. The windows of the cell are made of BaF<sub>2</sub> and a gold coated mirror is placed right after the back window enabling the optical path length to be increased by a factor of two. Note that the same dual-path cell arrangement was used in all the measurements presented below. The temperature and pressure of the cell were set to 50 °C and 1 bar, respectively. The pressure changes inside the cell caused by light absorption in the gas sample are read optically

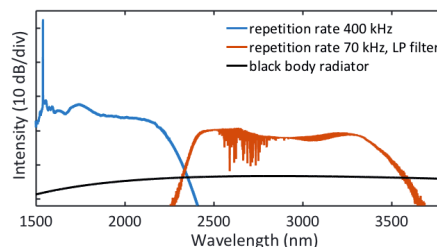


**Fig. 2.** Supercontinuum spectra corresponding to pump laser repetition rates of 70 kHz (solid red line) and 400 kHz (solid blue line) and used for the photoacoustic spectroscopic measurements of methane and water vapor, respectively. Note that the SC spectrum corresponding to 70 kHz has been spectrally filtered with a long-pass filter with cut-on wavelength of 2300 nm. The spectrum of the black body radiation source is theoretically estimated based on the temperature of the IR radiator (solid black line)

via interferometric detection where a cantilever acts as a moving mirror whose mechanical oscillations change the period of the interference fringes (see Ref.[17] for details on the readout procedure). The cantilever is gold-coated with dimensions of 6 mm, 10  $\mu$ m, and 1.5 mm (length, thickness, and width, respectively). The FTIR scanning mirror velocity was 1.6 kHz monitored by a HeNe laser. The modulation frequencies for the considered mid-infrared wavelength range of 1.7–3.5  $\mu$ m correspond to 600–290 Hz at the optimal frequency range for the CEPAS cell. The gas sample absorption spectrum is obtained by the Fourier transform of the recorded interferogram. The minimum wavelength resolution of the instrument is determined by the FTIR maximum optical path difference of 1 cm.

The experimentally recorded absorption spectrum of normal room air (20 °C, RH 30 %) water vapor with 7000 ppm concentration in the PAS cell and using the SC source with a repetition of 400 kHz as described above is shown in Fig. 3 (solid blue line). The total SC average power was 414 mW with a power spectral density of 275  $\mu$ W/nm in the water vapor absorption band, out of which 40 % was inserted into the CEPAS cell after the FTIR. The spectrum was measured with 1.4 nm resolution and averaged over 10 scans for a total measurement time of 50 s. We observe excellent correspondence with the theoretical spectrum predicted from the HITRAN database (plotted as a mirror image in the figure). For comparison, we also repeated the experiment using a black body radiation source (see the solid black line in Fig. 2 for an illustration of the spectrum). Note that the photoacoustic signal using the black body source has been magnified 10 times in the figure for visualization purposes, showing that the SC yields far better performance in terms of sensitivity and SNR. More specifically, the signal intensity and SNR are increased by a factor of 70 and 13, respectively, when using the SC source.

We then used the spectrally filtered SC source with 70 kHz repetition rate to measure the mid-infrared ro-vibrational absorption band of methane sampled from a flow of premixed 400 ppm methane in nitrogen carrier gas. The SC total power in this case (after the filter) was 78 mW with a power spectral

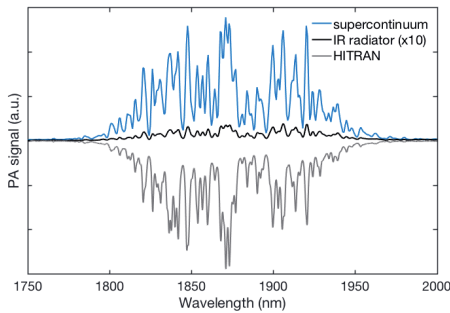


**Fig. 3.** Experimentally measured absorption spectrum of water vapor with the supercontinuum (solid blue line) and black body source (solid black line). The measurement resolution is 1.4 nm and the spectrum averaged over 10 different scans. The theoretical absorption spectrum as predicted from the HITRAN database is shown as the mirror image (solid grey line). Note that the results obtained with the black body have been magnified by 10 for convenient visualization.

density of  $71 \mu\text{W}/\text{nm}$  in the absorption band of methane. Again, 40 % of this power was finally injected into the CEPAS cell. The results are shown in Fig. 4 (red solid line), where we find excellent agreement with the absorption spectrum predicted from HITRAN. The results from the black body radiation source are also shown in the figure (with a 5 times magnification). As in the case of the water vapor, it is clear that the signal measured when using the SC is significantly increased (19 times), as compared to that obtained with the black body source. However, the increase in the SNR is only 1.8 times in this case, which is due to increased noise in the SC source at reduced repetition rate. Indeed, there are significant pulse-to-pulse fluctuations in the SC spectrum caused by the initial stage of modulation instability in the SC generating nonlinear dynamics [16], and a lower repetition rate results in an increase in the noise level as the intensity recorded is then averaged over a reduced number of SC pulses for lower repetition rates.

Besides the increase in the detected signal strength when using the SC source, another significant advantage as compared to a standard black body source lies in the fact that the SC is perfectly spatially coherent and the beam remains collimated independently of the optical path difference used in the FTIR. This means that one can increase the measurement resolution without any line-broadening or shifting effects [18] and still maintain high signal intensity. This is illustrated in Fig. 5 where we show the measured absorption spectrum of methane with different resolutions. The measurement times for resolutions of 1, 2 and 4 nm were 200 s, 100 s, and 50 s, respectively, with corresponding achieved SNRs of 136, 221, and 278. One can see how the lines become sharper and the signal amplitude is increased for higher resolutions. This contrasts with the use of a spatially incoherent black body source which requires reducing the input aperture size to ensure reasonable collimation over larger distances, thus leading to decreased signal intensities when performing measurements at higher resolutions.

We evaluated the concentration detection limits ( $3\sigma$ , 50 s) to be 2.6 ppm and 1.4 ppm for the black body and SC sources, respectively. The noise level was estimated from the non-absorbing

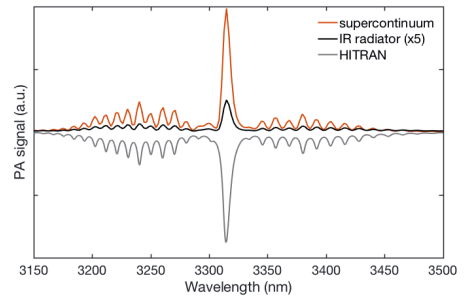


**Fig. 4.** Experimentally measured absorption spectrum of 400 ppm methane with the supercontinuum (solid red line) and black body source (solid black line). The measurement resolution is 4 nm, and the spectrum averaged over 10 different scans. The theoretical absorption spectrum as predicted from the HITRAN database is shown as the mirror image (solid grey line). Note that the results obtained with the black body have been magnified by 5 for convenient visualization.

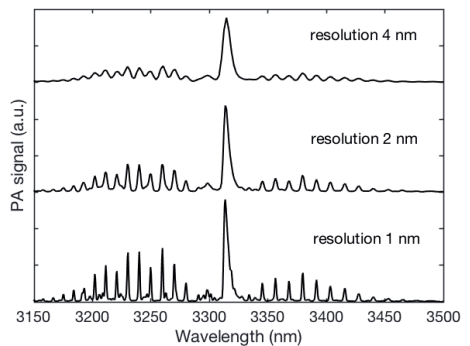


**Fig. 5.** Measured absorption spectrum of methane for different FTIR resolutions as indicated. The measurement time is inversely proportional to the resolution. The measurement times for resolutions of 1, 2, and 4 nm are 200 s, 100 s, and 50 s, respectively, with corresponding achieved SNRs of 136, 221, and 278.

part of the spectrum without methane by dividing the area to 10 blocks each consisting of 10 data points and averaging the standard deviations. The strongest signal value was then compared to the noise level ( $3\sigma$ ). The limit of detection was calculated by dividing the concentration by the SNR. The rather low enhancement in the detection limit when using the SC is caused by the high intensity noise level of the supercontinuum source induced by large pulse-to-pulse fluctuations. We anticipate that lower detection limits can be achieved using e.g., a more stable SC source with even higher power spectral density, a resonant acoustic cell, and single-frequency detection, or with a larger measurement setup. Yet, one should consider the detection limits achieved here in the context of broadband measurement from a small sample volume.

We have performed broadband CEPAS using a supercontin-

uum light source and demonstrated the potential of the technique by measuring the absorption spectrum of water vapor and methane in the mid-infrared spectral region. The approach allows for significant improvement in terms of sensitivity and resolution as compared to the use of a conventional black body radiation source. The spatially coherent and collimated SC beam also enables miniaturization of the Fourier transform spectrometer, as the narrow beam can easily be guided even in a small-form-factor instrument. Furthermore, high spatial coherence, in principle, enables multi-pass arrangements through the PAS cell, which could lead to enhanced sensitivity. Lower detection limits may be reached by reducing the intensity noise of the supercontinuum source using for example pump pulses of shorter durations and/or increasing the power spectral density of the supercontinuum source. The measurement time, on the other hand, is mostly limited by the cantilever frequency response which imposes the use of a low scanning speed FTIR. Yet, using a shot-to-shot stable SC source would allow for single scan measurements and improve the measurement speed by an order of magnitude. Our results open up novel perspectives for the development of cost-effective apparatus for broadband gas sensing.

**Funding.** Academy of Finland (318082); Graduate School of Tampere University of Technology; SPIM Graduate School of University of Burgundy Franche-Comté.

## REFERENCES

1. J. Uotila and J. Kauppinen, *Appl. spectroscopy* **62**, 655 (2008).
2. J. Kauppinen, K. Wilcken, I. Kauppinen, and V. Koskinen, *Microchem. journal* **76**, 151 (2004).
3. T. Tomberg, M. Vainio, T. Hieta, and L. Halonen, *Sci. reports* **8**, 1848 (2018).
4. T. Laurila, H. Cattaneo, V. Koskinen, J. Kauppinen, and R. Hernberg, *Opt. Express* **13**, 2453 (2005).
5. A. A. Kosterev and F. K. Tittel, *Appl. Opt.* **43**, 6213 (2004).
6. A. Veres, Z. Bozókí, Á. Mohácsi, M. Szakáll, and G. Szabó, *Appl. spectroscopy* **57**, 900 (2003).
7. V. Spagnolo, P. Patimisco, S. Borri, G. Scamarcio, B. Bernacki, and J. Kriesel, *Opt. letters* **37**, 4461 (2012).
8. C. B. Hirschmann, J. Lehtinen, J. Uotila, S. Ojala, and R. L. Keiski, *Appl. Phys. B* **111**, 603 (2013).
9. J. Peltola, M. Vainio, T. Hieta, J. Uotila, S. Sinisalo, M. Metsälä, M. Siltanen, and L. Halonen, *Opt. Express* **21**, 10240 (2013).
10. K. Wilcken and J. Kauppinen, *Appl. spectroscopy* **57**, 1087 (2003).
11. D. Wildanger, E. Rittweger, L. Kastrup, and S. W. Hell, *Opt. Express* **16**, 9614 (2008).
12. C. Amiot, A. Aalto, P. Ryczkowski, J. Toivonen, and G. Genty, *Appl. Phys. Lett.* **111**, 061103 (2017).
13. Y. Sych, R. Engelbrecht, B. Schmauss, D. Kozlov, T. Seeger, and A. Leipertz, *Opt. Express* **18**, 22762 (2010).
14. I. Hartl, X. D. Li, C. Chudoba, R. K. Ghanta, T. H. Ko, J. G. Fujimoto, J. K. Ranka, and R. S. Windeler, *Opt. Lett.* **26**, 608 (2001).
15. G. Humbert, W. J. Wadsworth, S. G. Leon-Saval, J. C. Knight, T. A. Birks, P. S. J. Russell, M. J. Lederer, D. Kopf, K. Wiesauer, E. I. Breuer, and D. Stifter, *Opt. Express* **14**, 1596 (2006).
16. J. M. Dudley, G. Genty, and S. Coen, *Rev. modern physics* **78**, 1135 (2006).
17. V. Koskinen, J. Fonsen, K. Roth, and J. Kauppinen, *Vib. Spectrosc.* **48**, 16 (2008). PAPERS PRESENTED AT THE 4TH INTERNATIONAL CONFERENCE ON ADVANCED VIBRATIONAL SPECTROSCOPY, CORFU, GREECE, 10-15 JUNE 2007 - PART I.
18. H. Wang, X. Ma, Y. Wang, D. Chen, W. Chen, and Q. Li, *Opt. Express* **25**, 19077 (2017).



# PUBLICATION

## II

### **Optical frequency comb photoacoustic spectroscopy**

I. Sadiek, T. Mikkonen, M. Vainio, J. Toivonen and A. Foltynowicz

*Physical Chemistry Chemical Physics* 47.44 (2018), 27849–27855

**Publication reprinted with the permission of the copyright holders**





## Optical frequency comb photoacoustic spectroscopy

Cite this: DOI: 10.1039/c8cp05666h

Ibrahim Sadiek,<sup>a</sup> Tommi Mikkonen,<sup>b</sup> Markku Vainio,<sup>bc</sup> Juha Toivonen<sup>b</sup>  
and Aleksandra Foltynowicz<sup>id</sup>\*<sup>a</sup>

We report the first photoacoustic detection scheme using an optical frequency comb—optical frequency comb photoacoustic spectroscopy (OFC-PAS). OFC-PAS combines the broad spectral coverage and the high resolution of OFCs with the small sample volume of cantilever-enhanced PA detection. In OFC-PAS, a Fourier transform spectrometer (FTS) is used to modulate the intensity of the exciting comb source at a frequency determined by its scanning speed. One of the FTS outputs is directed to the PA cell and the other is measured simultaneously with a photodiode and used to normalize the PA signal. The cantilever-enhanced PA detector operates in a non-resonant mode, enabling detection of a broadband frequency response. The broadband and the high-resolution capabilities of OFC-PAS are demonstrated by measuring the rovibrational spectra of the fundamental C–H stretch band of CH<sub>4</sub>, with no instrumental line shape distortions, at total pressures of 1000 mbar, 650 mbar, and 400 mbar. In this first demonstration, a spectral resolution two orders of magnitude better than previously reported with broadband PAS is obtained, limited by the pressure broadening. A limit of detection of 0.8 ppm of methane in N<sub>2</sub> is accomplished in a single interferogram measurement (200 s measurement time, 1000 MHz spectral resolution, 1000 mbar total pressure) for an exciting power spectral density of 42  $\mu\text{W}/\text{cm}^{-1}$ . A normalized noise equivalent absorption of  $8 \times 10^{-10} \text{ W cm}^{-1} \text{ Hz}^{-1/2}$  is obtained, which is only a factor of three higher than the best reported with PAS based on continuous wave lasers. A wide dynamic range of up to four orders of magnitude and a very good linearity (limited by the Beer–Lambert law) over two orders of magnitude are realized. OFC-PAS extends the capability of optical sensors for multispecies trace gas analysis in small sample volumes with high resolution and selectivity.

Received 6th September 2018,  
Accepted 25th October 2018

DOI: 10.1039/c8cp05666h

rsc.li/pccp

## 1 Introduction

Photoacoustic spectroscopy (PAS) is a routine technique in many vital applications including trace gas analysis,<sup>1</sup> and characterization of industrial products.<sup>2</sup> The small sample volume and zero-background are unique advantages over conventional absorption-based techniques (e.g., direct and cavity-enhanced absorption spectroscopy). Since the discovery of the photoacoustic effect by Bell in 1880,<sup>3</sup> and the seminal work of Kerr and Atwood on the first PA detection of infrared absorption in gases,<sup>4</sup> the performance of light sources, modulators, and detectors used for PAS has been significantly improved. High-power continuous wave (cw) laser sources in combination with different PAS detection schemes allow monitoring of trace gases in real time,<sup>1,5</sup> and detection limits down to parts-per-trillion.<sup>6–8</sup> However, cw lasers can be tuned only over a narrow spectral bandwidth, which may limit their usage to single species detection. Attention has also been paid to the development

of new sensing elements, replacing the conventional condenser and electret microphones used to detect the optically-induced acoustic wave.<sup>9–15</sup> In quartz-enhanced PAS,<sup>10–12</sup> a quartz tuning fork with resonance frequency of  $\sim 32 \text{ kHz}$  is used as an extremely sensitive acoustic detector because of its high quality factor ( $Q$ -factor  $> 10^4$ ). However, the commitment to resonance introduces restrictions on light sources because of the need for accurate control of modulation frequency. In contrast, cantilever-enhanced detectors<sup>13–16</sup> can be operated in a non-resonant mode, enabling detection of a wide range of audio frequencies,<sup>13</sup> and thus broadband detection schemes. In addition, they offer better mechanical stability and larger movement range than the flexible membranes in capacitive microphone detectors.<sup>13</sup>

Broadband detection of PA signals has so far been performed mostly with incoherent infrared radiators (e.g., lamps, blackbodies, etc.) modulated by conventional Fourier transform infrared (FT-IR) spectrometers.<sup>15,17</sup> When broadband radiation is passing through a scanning Michelson interferometer, each wavenumber component,  $\nu$  (in  $\text{cm}^{-1}$ ), is modulated at its characteristic Fourier frequency,  $f = V \times \nu$  (in Hz), where  $V$  is the optical path difference (OPD) scan velocity (in  $\text{cm s}^{-1}$ ). Absorption at each  $\nu$  is manifested as an acoustic wave at the

<sup>a</sup> Department of Physics, Umeå University, 901 87, Umeå, Sweden.

E-mail: aleksandra.foltynowicz@umu.se

<sup>b</sup> Laboratory of Photonics, Tampere University of Technology, Tampere, Finland<sup>c</sup> Department of Chemistry, University of Helsinki, Finland

corresponding modulation frequency that can be measured with the microphone. First broadband FT-IR-PAS instruments used electret microphones and were not widely applied because of the low spectral irradiance of broadband IR sources and the low sensitivity of the microphones.<sup>12,13,15</sup> The implementation of cantilever-enhanced detectors significantly increased the detection sensitivity and FT-IR-PAS setups with detection limits of methane of 1.5 ppm ( $3\sigma$ , 100 s, spectral resolution  $4\text{ cm}^{-1}$ ),<sup>18</sup> and 3 ppm ( $2\sigma$ , 168 s, spectral resolution  $8\text{ cm}^{-1}$ )<sup>15</sup> have been reported. In a very recent demonstration, Mikkonen *et al.*<sup>19</sup> used a super-continuum (SC) light source for broadband cantilever-enhanced PA detection and reported a limit of detection for methane of 1.4 ppm ( $3\sigma$ , 50 s, spectral resolution  $4\text{ cm}^{-1}$ ). Although the brightness of SC sources exceeds that of thermal emitters by orders of magnitude, the noise level is also increased, which is the reason for the relatively small improvement of the detection limit.

The spectral resolution of all broadband PAS demonstrations has so far been limited by the nominal resolution of the FT-IR spectrometer, given by the inverse of the maximum delay range.<sup>20</sup> Conventional FT-IR spectrometers provide a resolution of  $0.1\text{ cm}^{-1}$  (i.e., 3 GHz), and higher resolutions, up to  $0.002\text{ cm}^{-1}$ , have been achieved with large instruments (OPD = 4.5 m) and long measurement times (30 min).<sup>21</sup> In addition, care has to be taken to select a proper apodization function in order to minimize the instrumental line shape (ILS) distortions. Using an optical frequency comb (OFC) as a light source for Fourier transform spectrometers (FTS), in the so-called comb-based FTS, allows much faster acquisition (of the order of seconds) of spectra with high signal-to-noise ratio (S/N),<sup>22</sup> and resolution down to kHz range with no ILS contribution.<sup>23</sup>

Here, we report the first demonstration of photoacoustic spectroscopy using an optical frequency comb. We call the technique: optical frequency comb photoacoustic spectroscopy (OFC-PAS). OFC-PAS combines the wide spectral coverage and high resolution of comb-based FTS with the small sample volume and wide dynamic range of photoacoustic detection. In this first demonstration, we measured high resolution PA spectra of the fundamental C–H stretch band of methane,  $\text{CH}_4$ , in nitrogen,  $\text{N}_2$ , at different pressures, in good agreement with simulations based on the HITRAN database.<sup>24</sup> Spectral resolution up to 400 MHz, limited by the pressure broadening and 75 times better than the best reported using a SC source (30 GHz),<sup>19</sup> has been accomplished. These capabilities open up for new insights for high resolution multicomponent trace gas analysis in small sample volumes.

## 2 Photoacoustic signal

The PA signal is produced by the non-radiative collisional relaxation in periodically excited molecules, producing periodic local heating at the modulation frequency, which can be detected by means of microphones. The PA signal,  $S(\nu)_{\text{PA}}$ , measured in volts, is related to the absorption coefficient,  $\alpha(\nu)$  (in  $\text{cm}^{-1}$ ), as:

$$S(\nu)_{\text{PA}} = \alpha(\nu) \times \phi(S_{\text{m}}C_{\text{cell}}P(\nu)\eta) \quad (1)$$

where the scaling factor,  $\phi$  (in  $\text{V}/\text{cm}^{-1}$ ), is a function of the cantilever sensitivity,  $S_{\text{m}}$  (in  $\text{V Pa}^{-1}$ ), the PA cell response constant,  $C_{\text{cell}}$  (in  $\text{Pa cm W}^{-1}$ ), the exciting light power,  $P(\nu)$  (in W), and the efficiency of the conversion of light energy into heat,  $\eta$ . Since the power of the comb source is a function of frequency,  $\nu$ , it should be monitored and used to normalize the PA signal. The absorption coefficient is related to the temperature-dependent line strength,  $S(T)$  [in  $\text{cm}^{-1} (\text{molecule cm}^{-2})^{-1}$ ], gas density,  $[C]$  (in  $\text{molecule cm}^{-3}$ ) and the normalized line shape function,  $g(\nu)$  (in  $1/\text{cm}^{-1}$ ) as  $\alpha(\nu) = S(T)g(\nu)$ , where the line parameters can be found in the HITRAN database.<sup>24</sup>

The intensity of the measured PA signal at a given total pressure changes linearly with gas density under the assumption that (i) the density of the absorbing gas is relatively low, so that Beer-Lambert law is linear, (ii) the input laser power is not high, so that absorption saturation effects can be neglected, and (iii) the relaxation rate from absorbed energy to heat is much faster than the rate of heating/cooling of the gas sample. However, the measured signal is also proportional to the scaling factor,  $\phi$ , which is a function of the sample pressure, composition, and temperature. Therefore, the measurement conditions of pressure and gas matrix have to be optimized to accomplish the highest S/N according to the application requirements (*vide infra*).

## 3 Experimental

A schematic of the OFC-PAS setup is shown in Fig. 1. The mid-IR optical frequency comb is based on a doubly-resonant optical parametric oscillator (DROPO) with an orientation-patterned GaAs (OP-GaAs) crystal. The DROPO is pumped by a Tm:fibre femtosecond laser (IMRA America) emitting at  $\sim 1.95\text{ }\mu\text{m}$  with a repetition rate of 125 MHz and up to 2.5 W output power. The DROPO can be operated in both degenerate and non-degenerate modes. In the non-degenerate mode, the DROPO output consists of a signal comb with  $\sim 250\text{ nm}$  bandwidth and tunable between  $3.1\text{--}3.6\text{ }\mu\text{m}$ , and an idler comb with  $\sim 350\text{ nm}$  bandwidth tunable between  $4.6\text{--}5.4\text{ }\mu\text{m}$ . Here we use the signal comb light around  $3.3\text{ }\mu\text{m}$  ( $3000\text{ cm}^{-1}$ ) to excite the fundamental C–H stretch band of  $\text{CH}_4$ . A detailed description of the DROPO operation is given in ref. 25. Compared to that work, the

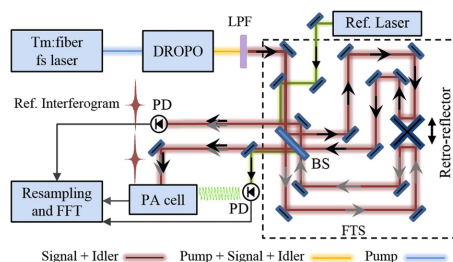


Fig. 1 Schematic of the experimental setup: DROPO – doubly resonant optical parametric oscillator; LPF – long-pass filter; BS – beam splitter; PD – photodetector; PA – photoacoustic; FTS – Fourier transform spectrometer.

coupling efficiency of the pump laser power into the DROPO cavity has been optimized by better choice of mode-matching lenses, providing up to 60 mW of signal and idler power compared to 48 mW obtained before. Moreover, the bandwidth of the dither lock used for stabilizing the DROPO cavity length has been increased to decrease the intensity noise. This has been achieved by mounting one of the DROPO cavity mirrors on a fast (70 kHz bandwidth) piezoelectric transducer (PZT). The fast PZT is used to dither the cavity length at 77 kHz, while both the fast and the slow (12 kHz bandwidth) PZTs are used for locking. The synchronous demodulation of the output of a PbSe detector, placed after the input coupler, yields an error signal that is fed back to the PZTs via two servo controllers.

The output of the DROPO, after long-pass filter in order to block the remainder of the pump power, is coupled into a home-built fast-scanning FTS. A general schematic of the tilt-compensated interferometer is shown in Fig. 1 (dashed box). A stable cw reference diode laser ( $\lambda_{\text{ref}} = 1563 \text{ nm}$ ) is also coupled to the FTS and is used for the calibration of the OPD. The two retro-reflectors, mounted back-to-back, provide easier alignment and larger OPD range compared to conventional interferometers with one moving mirror. The maximum OPD range is 2.8 m, corresponding to a nominal resolution of  $0.0037 \text{ cm}^{-1}$ , or 110 MHz. The OPD is scanned at  $V = 0.16 \text{ cm s}^{-1}$ , which implies that the signal comb is modulated at Fourier frequencies in the 470–510 Hz range. Two out-of-phase intensity interferograms are constructed at the two outputs of the FTS, with total power of 31.5% of the input power (16.5% in one output and 15% in the other). One of the output beams is directed to a cantilever-enhanced photoacoustic cell, while the other is directly measured with a HgCdTe detector (VIGO System) and used for normalization of the PA signal. For a typical input power of 50 mW, 8 mW out of the FTS is guided to the PA cell, of which 4.8 mW and 3.2 mW are contained in the signal and idler combs, respectively.

The photoacoustic cell (Gasera, PA201) with a cantilever-enhanced detector is used. The output beam of the FTS has a diameter of 5 mm and the PA cell has an input inner diameter of 4 mm. Therefore, a focusing lens ( $f = 50 \text{ cm}$ ) was placed 25 cm in front of the PA cell to reduce the beam diameter to 2.5 mm. The PA cell is made of gold-coated aluminium with a length of 100 mm and a sample volume of 8 mL. A double-path configuration is implemented using a gold-coated mirror on the back side of the cell resulting in power spectral density of the signal comb of  $42 \mu\text{W}/\text{cm}^{-1}$ . The displacement of the cantilever as a result of pressure changes due to absorption is measured via an integrated spatial-type interferometer in the photoacoustic cell.<sup>13,16</sup> The PA cell is also equipped with a vibrational noise damper to attenuate external acoustic noise.

Two mass flow controllers (Bronkhorst, F-201CV) and a pressure regulator (Bronkhorst, P-702CV) are used to flow the gas sample and regulate the pressure in the line leading to the PA cell. The PA cell has an internal pumping and gas exchange system that draws the sample from the supply line using micro pumps and automatic valve system. This gas supply system allows for changing the pressure inside the PA cell in the range between 300–1000 mbar. All measurements were performed at

23 °C, as controlled by the PA cell thermostat. The test gas methane ( $100 \pm 10 \text{ ppm CH}_4$  in  $\text{N}_2$ , air liquide) was used. Pure  $\text{N}_2$  was available for flushing the cell and diluting the methane sample.

To obtain broadband OFC-PAS spectra, three interferograms are acquired simultaneously using a National Instruments hardware (PCI-6221, 250 kS/s, 16 bit) and home-written LabVIEW<sup>TM</sup> program: the PA and the comb interferograms, as well as the cw laser interferogram for OPD calibration. Afterwards, the PA and the comb interferograms are resampled at the zero-crossings and extrema of the cw laser interferogram using home-written MATLAB<sup>®</sup> program. The absolute value of the Fourier transform of the OPD-calibrated interferograms yields the frequency-calibrated PA spectrum and the comb intensity envelope. Finally, the PA spectrum is divided by the comb intensity envelope to yield a normalized PA spectrum. The spectra of the C–H stretch band of  $\text{CH}_4$  were measured at different working pressures of 1000 mbar, 650 mbar, and 400 mbar. At each pressure, the nominal resolution of the FTS was adjusted to yield 3 points per full width at half maximum (FWHM) of the methane lines, which resulted in a resolution of 1000 MHz, 650 MHz, and 400 MHz for the three pressures, respectively. The acquisition times of single interferograms with these resolutions were 200 s, 308 s, and 500 s, respectively.

## 4 Results and discussion

### Noise considerations

Fig. 2 presents the FFT of a typical OFC-PAS interferogram in the Fourier frequency domain for frequencies from DC to 1 kHz. The red trace was recorded with 100 ppm  $\text{CH}_4$  in  $\text{N}_2$  at a total cell pressure of 1000 mbar and a resolution of 1000 MHz, while the blue trace is the background noise of the cantilever measured with no light into the PA cell. The  $\text{CH}_4$  absorption appears in the Fourier frequency domain at  $\sim 485 \text{ Hz}$ , which is determined by the OPD scan velocity. The broad peak at  $\sim 650 \text{ Hz}$  is the background noise amplified by the cantilever resonance. The cantilever resonance amplifies both the signal and the noise levels equally, leaving the resulting S/N unchanged.<sup>13–15</sup> The peaks at frequencies below 200 Hz are the intensity noise of the

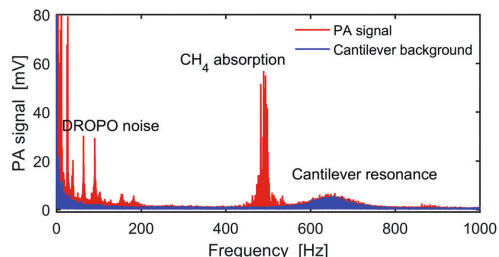


Fig. 2 The OFC-PAS spectrum in the radio/Fourier frequency domain. Red: the PA signal of 100 ppm  $\text{CH}_4$  in  $\text{N}_2$  (cell pressure: 1000 mbar, resolution: 1000 MHz). Blue: cantilever background measured with no light to the PA cell.

DROPO, which remains after stabilization of the DROPO cavity length. Therefore, the working range of the FTS modulation frequency that can be utilized for PAS measurements with constant cantilever noise level and high S/N is 200–600 Hz. Note that this allows also the measurement of absorption at the idler comb frequencies, which would appear at  $\sim 300$  Hz. Further improvements of the locking stability could minimize the DROPO intensity noise, extending the working frequency range below 200 Hz.

### Proof-of-concept measurement

Fig. 3 shows the OFC-PAS spectrum of the C–H stretch band of 100 ppm of  $\text{CH}_4$  in  $\text{N}_2$  at 1000 mbar total pressure and 1000 MHz resolution (*i.e.*, a zoom of Fig. 2 with frequency scale expressed in wavenumbers). Panel a presents the normalized PA spectrum (red, left axis) of the *P*, *R*, and *Q* rovibrational structures of the band together with simulated absorption coefficient,  $\alpha$  (blue, right axis), based on the parameters from the HITRAN database,<sup>24</sup> indicating the broadband coverage of the signal comb. A scaling factor  $\phi = 10.5 \text{ V/cm}^{-1}$  was used in the simulations (see eqn (1)) to reproduce the measured spectrum. Panel (b) is a zoom in around the *Q*-branch region,

showing the high spectral resolution capability with no ILS distortion. Panel c shows the spectral envelope of the comb at 1000 MHz resolution (black), and a smoothing of the spectral envelope with 100 times lower resolution (10 GHz). The latter, interpolated to 1000 MHz, was used to normalize the acquired PA spectrum. Panels a and b show a very good agreement in the relative line intensities between the measured PA spectrum and the simulated absorption spectrum based on the HITRAN database.<sup>24</sup> The slight offset of the baseline in panels a and b is caused by taking the absolute value of the FFT.

We have observed that the entire C–H stretch band is imaged with a much smaller amplitude at the lower and higher frequency sides symmetrically around the band origin. Such “ghost” imaging might be caused by modulation of the intensity of the light source or sampling errors of the interferogram in the PA cell, since the cantilever displacement is measured interferometrically. These artefacts account for the slight intensity mismatch between the measurements and the simulations in the higher frequency side and the unassigned lines in the lower frequency side. It should also be noted that the normalization of the PA signal by the comb envelope may introduce a slight intensity mismatch with respect to the simulations due to the absorption of molecular species (mainly interfering water lines) in the non-common beam path.

### Resolution and limit of detection

Methane absorption features under the available pressure range of the PA cell (hundreds of millibars) have FWHM of hundreds of MHz. Thus, the nominal resolution of our FTS is sufficient to record the pressure broadened absorption features with negligible ILS contribution. Fig. 4 shows (red, left axis) the PA spectra of the C–H stretch band around the *Q*-branch region for 100 ppm  $\text{CH}_4$  in  $\text{N}_2$  at different total cell pressures and spectral resolutions: panel (a) – 1000 mbar and 1000 MHz resolution; panel (b) – 650 mbar and 650 MHz resolution; panel (c) – 400 mbar and 400 MHz resolution. A very good agreement between the experiment and the simulated absorption coefficient,  $\alpha$  (blue, right axis), has been obtained at all working pressures. Scaling factors ( $\phi$  in eqn (1)) were  $10.5 \text{ V/cm}^{-1}$ ,  $9.20 \text{ V/cm}^{-1}$ , and  $15.0 \text{ V/cm}^{-1}$  in the simulations for 1000 mbar, 650 mbar, and 400 mbar, respectively.

Since the three measurements shown in Fig. 4 were performed with the same input laser power, PA cell, and gas matrix (*i.e.*,  $P$ ,  $C_{\text{cell}}$  and  $\eta$  are constants), the change of the scaling factor is a direct measure of the change of cantilever sensitivity with pressure, attributed to the so-called gas spring and the effective mass that depend on the pressure and the molecular mass of the gas.

Table 1 summarizes the scaling factors, signal and noise levels as well as the S/N observed at the three different pressures. The noise,  $\sigma(\text{CH}_4)$ , is estimated as the standard deviation of the baseline of the  $\text{CH}_4$  spectra around  $3021 \text{ cm}^{-1}$ . We note that the noise in the presence of  $\text{CH}_4$  absorption is higher than the noise level measured with pure  $\text{N}_2$  in the PA cell [ $\sigma(\text{N}_2)$ , also listed in Table 1]. This difference might originate from the small structures that exist on the baseline of the  $\text{CH}_4$  measurements due to the aforementioned sampling problems.

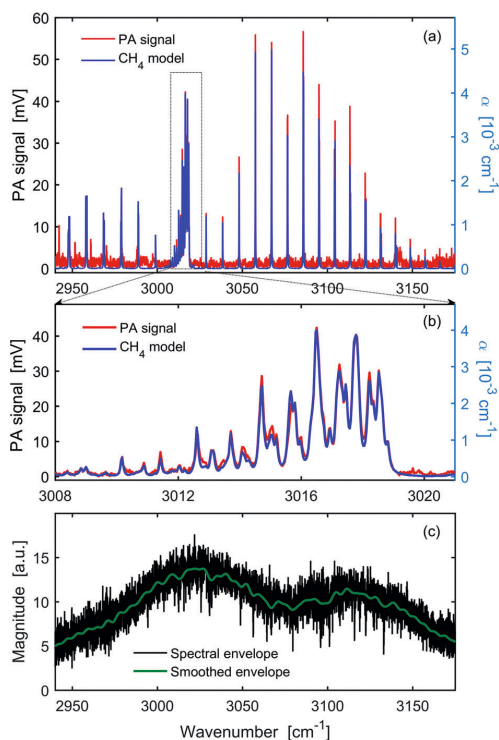


Fig. 3 (a) PA rovibrational spectrum of the C–H stretch band of 100 ppm of methane (red, left axis: 1000 mbar cell pressure, 1000 MHz resolution, 200 s measurement time) compared to the simulated absorption coefficient,  $\alpha$ , based on the HITRAN database (blue, right axis), (b) zoom of the *Q*-branch region, and (c) the spectral envelope of the comb.

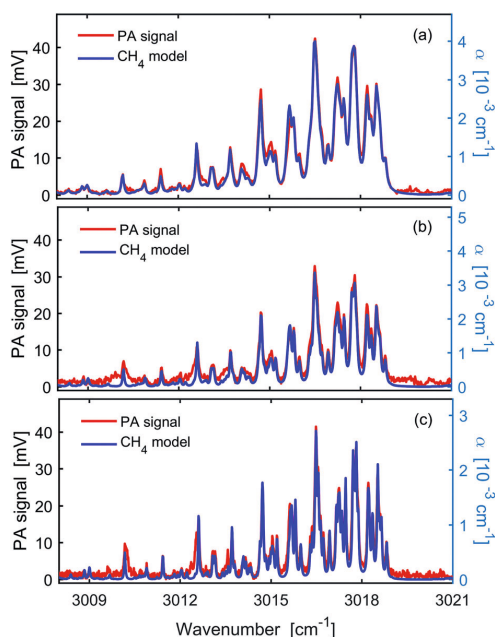


Fig. 4 PA spectra of the Q-branch of the C–H stretch band of 100 ppm methane (red, left axis) at (a) 1000 mbar and 1000 MHz resolution, (b) 650 mbar and 650 MHz resolution, and (c) 400 mbar and 400 MHz resolution, compared to models based on the HITRAN database (blue, right axis). Scaling factors of 10.5 V/cm<sup>−1</sup>, 9.20 V/cm<sup>−1</sup>, and 15.0 V/cm<sup>−1</sup> were used in the simulations for panels (a, b, and c), respectively.

We also note that background noise measurements with light on and off yielded similar levels. The S/N is calculated as the ratio of the line-centre PA signal at 3016.5 cm<sup>−1</sup> ( $S_{PA}$ ) and the standard deviation of the noise on the baseline around 3021 cm<sup>−1</sup>.

In conventional FT-IR the S/N decreases with the square root of the increase of the resolution,<sup>26</sup> assuming constant signal and white noise. The change of S/N must also account for the change of the line-centre absorption coefficient with pressure and number density. The line-centre absorption, also listed in Table 1, denoted by  $F_x$  and normalized to 1 at 1000 mbar, is estimated for the line at 3016.5 cm<sup>−1</sup> using the HITRAN database.<sup>24</sup> The last column of Table 1 shows the S/N expected in conventional FT-IR, taking into account the change of resolution and the line-centre absorption coefficient (assuming S/N of 100 at 1000 mbar). The discrepancy between the

measured S/N and that predicted for conventional FT-IR is attributed to the fact that our PA measurements are not purely white noise limited, and that the cantilever signal and noise are enhanced by different factors when the pressure changes.

In general one can conclude that the fundamental trading rule of measurement time, resolution, and sensitivity of conventional FT-IR must be modified to include also the cantilever response and applied according to the application need. For example, high-resolution spectral measurements, which are essential for better selectivity and multicomponent analysis, would preferably be performed at the pressure of 400 mbar rather than 650 mbar, since there is an indication of higher cantilever sensitivity that compensates the decrease in S/N due to increased resolution and lower  $F_x$ .

We evaluated the attainable limit of detection (LOD) based on the S/N of the strongest methane line at 3058 cm<sup>−1</sup> (see Fig. 3) measured at 1000 mbar, equal to 120. This corresponds to a detection limit of 0.8 ppm in 200 s for an exciting signal comb power spectral density of 42  $\mu\text{W}/\text{cm}^{-1}$  in the absorption band of methane. Table 2 compares our LOD with that of previous FT-IR-PAS and the recent SC-PAS experiments using cantilever-enhanced detectors (all normalized to  $1\sigma$  and 100 s measurement time). As shown in Table 2, the LOD is comparable for the three methods, while the resolution of OFC-PAS is more than two orders of magnitude better. Moreover, considering the lower power spectral density and the higher resolution of OFC-PAS compared to SC-PAS,<sup>19</sup> the attainable LOD of OFC-PAS becomes about a factor of five better than that of SC-PAS.

We also evaluated the performance of the system in terms of the normalized noise equivalent absorption,  $\text{NNEA} = \alpha_{\min} P_{\text{sp.el}} \sqrt{t}$ , where  $\alpha_{\min}$  is the minimum detectable absorption, equal to  $4.2 \times 10^{-5} \text{ cm}^{-1}$  at 1000 mbar,  $P_{\text{sp.el}}$  is the power per single spectral component, and  $t$  is the measurement time. At a resolution of 1000 MHz (0.033 cm<sup>−1</sup>), the power spectral density of 42  $\mu\text{W}/\text{cm}^{-1}$  corresponds to  $P_{\text{sp.el}}$  of 1.4  $\mu\text{W}$ . Considering the measurement time of 200 s, we obtained a NNEA of  $8 \times 10^{-10} \text{ W cm}^{-1} \text{ Hz}^{-1/2}$ , which is comparable to values reported with PAS based on cw lasers in the range of  $2.7 \times 10^{-10}$  to  $18 \times 10^{-10} \text{ W cm}^{-1} \text{ Hz}^{-1/2}$ .<sup>7,27</sup> The very low NNEA obtained here confirms that the comb source is not causing significant noise contribution. Moreover, the capability of OFC-PAS to record spectra over thousands of elements simultaneously is not fully reflected in the definition of NNEA.

### Linearity and dynamic range

The linearity of the recorded PA signal for different number density at the same total cell pressure is demonstrated in Fig. 5,

Table 1 Scaling factors, experimental signal and noise levels as well as the S/N at different pressures and spectral resolutions, compared to S/N expected for conventional FT-IR. See text for details

Pressure [mbar]	Resolution [MHz]	$\phi$ [V/cm <sup>−1</sup> ]	$S_{PA}^a$ [mV]	$\sigma(\text{CH}_4)$ [mV]	$\sigma(\text{N}_2)$ [mV]	Measured S/N	$F_x^b$	Expected S/N
1000	1000	10.5	42.8	0.43	0.23	100	1.0	100
650	650	9.20	31.6	0.61	0.32	52	0.85	69
400	400	15.0	41.2	0.74	0.52	56	0.69	44

<sup>a</sup> Line-centre PA signal at 3016.5 cm<sup>−1</sup>. <sup>b</sup> Normalized line-centre absorption coefficient.



**Table 2** The obtained limits of detection, LOD (in ppm, for  $1\sigma$  and 100 s), spectral resolution, and power spectral density,  $P$ , of our experiment compared to that of FT-IR-PAS and the recent SC-PAS using cantilever-enhanced detector

	LOD [ppm]	Res. [GHz]	$\bar{P}$ [ $\mu\text{W}/\text{cm}^{-1}$ ]	Ref.
FT-IR-PAS	0.50	120		18
FT-IR-PAS	1.9	240		15
SC-PAS	0.33	120	61	19
OFC-PAS	1.1	1	42	This work

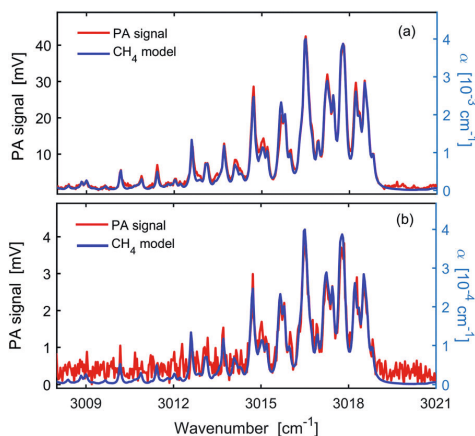


**Fig. 5** PA spectra of the C–H stretch band of methane around the Q-branch region at 1000 MHz resolution for 100 ppm methane in  $\text{N}_2$  (panel a, left axis) and 10 ppm methane in  $\text{N}_2$  (panel b, left axis). Simulations (right axis) are based on HITRAN database using a scaling factor of  $10.5 \text{ V}/\text{cm}^{-1}$ .

which shows spectra of 100 ppm (panel a) and 10 ppm methane (panel b) in  $\text{N}_2$  measured at the same total pressure of 1000 mbar and resolution of 1000 MHz. The same scaling factor of  $10.5 \text{ V}/\text{cm}^{-1}$  has been used in both simulations (blue, right axis), giving a very good agreement with the experiment (red, left axis) in both cases. We also measured the PA spectrum for mixing ratio of 1%  $\text{CH}_4$  in  $\text{N}_2$  (data is not shown). No saturation effects on the measured PA interferogram have been observed (*i.e.*, the centre burst of the interferogram was not cut), indicating a four orders of magnitude dynamic range (*i.e.* from  $10^{-6}$  to  $10^{-2}$ ). However, at this high mixing ratio a non-linearity of the signal has been observed due to non-linearity of the Beer-Lambert law. Therefore, it can be concluded that the presented OFC-PAS is linear over two orders of magnitude within a dynamic range of four orders of magnitude.

## 5 Conclusions

The broadband optical frequency comb photoacoustic spectroscopy (OFC-PAS) technique has been demonstrated for the first time. In OFC-PAS, a Fourier transform spectrometer is used to modulate the comb intensity and a cantilever-enhanced detector is used in a non-resonant mode to record the photoacoustic signal over a wide frequency range in a small sample volume.

The PA spectrum is normalized by the comb intensity envelope that is measured simultaneously at the second output of the FTS. In the first demonstration of OFC-PAS, we measured the PA spectra of the fundamental C–H stretch band of  $\text{CH}_4$  in  $\text{N}_2$  at total pressures between 400–1000 mbar, with no instrumental line shape distortion and in a very good agreement with simulated absorption spectra based on the HITRAN database. While the obtained detection limit of methane of 0.8 ppm in 200 s, with power spectral density of  $42 \mu\text{W}/\text{cm}^{-1}$ , is comparable to that achieved in previous broadband PAS demonstrations based on incoherent and supercontinuum light sources, the resolution is two orders of magnitude better, limited only by the pressure broadening of the methane absorption lines. Moreover, we obtained a normalized noise equivalent absorption of  $8 \times 10^{-10} \text{ W cm}^{-1} \text{ Hz}^{-1/2}$ , which is only a factor of three higher than the best reported with continuous wave laser PAS.

In the measurements presented in the current work, the nominal resolution of the FTS was higher than the repetition rate of the comb source,  $f_{\text{rep}}$ , and sufficient to record the absorption lines with negligible ILS distortion. If needed, spectral features narrower than  $f_{\text{rep}}$  can be measured with no ILS distortion using the method of comb-based FTS with sub-nominal resolution, in which interferograms with length matched precisely to  $c/f_{\text{rep}}$  are measured.<sup>23,28,29</sup> OFC-PAS can also be realized using the dual-comb approach<sup>30–32</sup> rather than the mechanical FTS. However, the main advantage of dual comb spectroscopy, *i.e.* the rapid data acquisition, cannot be utilized in OFC-PAS, since the frequency of the interferogram is limited by the cantilever response to the hundreds of Hz range.

The detection limit of OFC-PAS can be improved by several measures. First of all, a factor of 40 improvement can be expected using available high-power mid-IR OFC sources<sup>33</sup> with an output power of up to 1.5 W, compared to 36 mW of the signal comb used in this work (assuming noise is not introduced). Secondly, using multi-line fitting routines instead of the single point S/N determination would decrease the uncertainty of the fitted concentration and yield improved LOD, where a factor of 11 improvement is expected for the C–H stretch band of methane addressed in our work.<sup>34</sup> Using these two measures combined, a LOD of methane in the lower ppb range should be readily accomplished.

The high fidelity of the high-resolution broadband spectra measured with OFC-PAS holds the potential to extend the capability of optical spectrometers for multispecies trace gas analysis in very small sample volumes.

## Conflicts of interest

There are no conflicts to declare.

## Acknowledgements

The authors thank Amir Khodabakhsh and Chuang Lu for help in optimizing the DROPO performance, Isak Silander for help in setting up the gas supply system, and Francisco Senna Vieira,



Teemu Tomberg and Juho Karhu for useful discussions about OFC-PAS. The work at UmU is financed by the Knut and Alice Wallenberg Foundation (KAW 2015.0159). M. V. and T. M. acknowledge the financial support of the Academy of Finland (Grant 314363).

## References

- 1 F. J. M. Harren, J. Mandon and S. M. Cristescu, *Photoacoustic Spectroscopy in Trace Gas Monitoring: Encyclopedia of Analytical Chemistry*, John Wiley and Sons, Chichester, UK, 2012.
- 2 T. Schmid, *Anal. Bioanal. Chem.*, 2006, **384**, 1071–1086.
- 3 A. G. Bell, *Am. J. Sci.*, 1880, **20**, 305–324.
- 4 E. L. Kerr and J. G. Atwood, *Appl. Opt.*, 1968, **7**, 915–921.
- 5 J. Li, W. Chen and B. Yu, *Appl. Spectrosc. Rev.*, 2011, **46**, 440–471.
- 6 V. Spagnolo, P. Patimisco, S. Borri, G. Scamarcio, B. E. Bernacki and J. Kriesel, *Opt. Lett.*, 2012, **37**, 4461–4463.
- 7 T. Tomberg, M. Vainio, T. Hieta and L. Halonen, *Sci. Rep.*, 2018, **8**, 239–245.
- 8 Y. He, Y. Ma, Y. Tong, X. Yu and F. K. Tittel, *Opt. Express*, 2018, **26**, 9666–9675.
- 9 R. E. Lindley, A. M. Parkes, K. A. Keen, E. D. McNaghten and A. J. Orr-Ewing, *Appl. Phys. B: Lasers Opt.*, 2007, **86**, 707–713.
- 10 A. A. Kosterev, Y. A. Bakhrin, R. F. Curl and F. K. Tittel, *Opt. Lett.*, 2002, **27**, 1902–1904.
- 11 K. Liu, X. Guo, H. Yi, W. Chen, W. Zhang and X. Gao, *Opt. Lett.*, 2009, **34**, 1594–1596.
- 12 P. Patimisco, G. Scamarcio, F. K. Tittel and V. Spagnolo, *Sensors*, 2014, **14**, 6165–6206.
- 13 K. Wilcken and J. Kauppinen, *Appl. Spectrosc.*, 2003, **57**, 1087–1092.
- 14 T. Kuusela and J. Kauppinen, *Appl. Spectrosc. Rev.*, 2007, **42**, 443–474.
- 15 J. Uotila and J. Kauppinen, *Appl. Spectrosc.*, 2008, **62**, 655–660.
- 16 V. Koskinen, J. Fonsen, K. Roth and J. Kauppinen, *Vib. Spectrosc.*, 2008, **48**, 16–21.
- 17 K. H. Michaelian, *Photoacoustic IR spectroscopy. Instrumentation, applications and data analysis*, Wiley-VCH, Weinheim, 2nd edn, 2010.
- 18 C. B. Hirschmann, J. Uotila, S. Ojala, J. Tenhunen and R. L. Keiski, *Appl. Spectrosc.*, 2010, **64**, 293–297.
- 19 T. Mikkonen, C. Amiot, A. Aalto, K. Patokoski, G. Genty and J. Toivonen, *Opt. Lett.*, 2018, **43**, 5094–5097.
- 20 P. R. Griffiths and J. A. de Haseth, *Fourier transform infrared spectrometry*, Wiley-Interscience, Chichester, John Wiley, Hoboken, NJ, 2nd edn, 2007.
- 21 V. Werwein, J. Brunzendorf, A. Serdyukov, O. Werhahn and V. Ebert, *J. Mol. Spectrosc.*, 2016, **323**, 28–42.
- 22 J. Mandon, G. Guelachvili and N. Picqué, *Nat. Photonics*, 2009, **3**, 99–102.
- 23 L. Rutkowski, A. C. Johansson, G. Zhao, T. Hausmaninger, A. Khodabakhsh, O. Axner and A. Foltynowicz, *Opt. Express*, 2017, **25**, 21711–21718.
- 24 L. Rothman, I. Gordon, Y. Babikov, A. Barbe, D. C. Benner, P. Bernath, M. Birk, L. Bizzocchi, V. Boudon, L. Brown, A. Campargue, K. Chance, E. Cohen, L. Coudert, V. Devi, B. Drouin, A. Fayt, J.-M. Flaud, R. Gamache, J. Harrison, J.-M. Hartmann, C. Hill, J. Hodges, D. Jacquemart, A. Jolly, J. Lamouroux, R. L. Roy, G. Li, D. Long, O. Lyulin, C. Mackie, S. Massie, S. Mikhailenko, H. Müller, O. Naumenko, A. Nikitin, J. Orphal, V. Perevalov, A. Perrin, E. Polovtseva, C. Richard, M. Smith, E. Starikova, K. Sung, S. Tashkun, J. Tennyson, G. Toon, V. Tyuterev and G. Wagner, *J. Quant. Spectrosc. Radiat. Transfer*, 2013, **130**, 4–50.
- 25 A. Khodabakhsh, V. Ramaiah-Badarla, L. Rutkowski, A. C. Johansson, K. F. Lee, J. Jiang, C. Mohr, M. E. Fermann and A. Foltynowicz, *Opt. Lett.*, 2016, **41**, 2541–2544.
- 26 N. R. Newbury, I. Coddington and W. Swann, *Opt. Express*, 2010, **18**, 7929–7945.
- 27 J. Peltola, M. Vainio, T. Hieta, J. Uotila, S. Sinisalo, M. Metsälä, M. Siltanen and L. Halonen, *Opt. Express*, 2013, **21**, 10240–10250.
- 28 P. Maslowski, K. F. Lee, A. C. Johansson, A. Khodabakhsh, G. Kowzan, L. Rutkowski, A. A. Mills, C. Mohr, J. Jiang, M. E. Fermann and A. Foltynowicz, *Phys. Rev. A*, 2016, **93**, 021802.
- 29 L. Rutkowski, P. Maslowski, A. C. Johansson, A. Khodabakhsh and A. Foltynowicz, *J. Quant. Spectrosc. Radiat. Transfer*, 2018, **204**, 63–73.
- 30 S. Schiller, *Opt. Lett.*, 2002, **27**, 766–768.
- 31 F. Keilmann, C. Gohle and R. Holzwarth, *Opt. Lett.*, 2004, **29**, 1542–1544.
- 32 A. Schliesser, M. Brehm, F. Keilmann and D. van der Weide, *Opt. Express*, 2005, **13**, 9029–9038.
- 33 F. Adler, K. C. Cossel, M. J. Thorpe, J. Hartl, M. E. Fermann and J. Ye, *Opt. Lett.*, 2009, **34**, 1330–1332.
- 34 F. Adler, P. Maslowski, A. Foltynowicz, K. C. Cossel, T. C. Briles, I. Hartl and J. Ye, *Opt. Express*, 2010, **18**, 21861–21872.



# PUBLICATION

## III

**Supercontinuum intensity noise coupling in Fourier transform photoacoustic spectroscopy**

T. Mikkonen, Z. Eslami, G. Genty and J. Toivonen

*Optics Letters* 47.7 (2022), 1713–1716

**Publication reprinted with the permission of the copyright holders**



## Supercontinuum intensity noise coupling in Fourier transform photoacoustic spectroscopy

TOMMI MIKKONEN,\*  ZAHRA ESLAMI,  GOËRY GENTY,  AND JUHA TOIVONEN 

Photonics Laboratory, Physics Unit, Tampere University, Tampere, Finland

\*Corresponding author: [tommi.mikkonen@tuni.fi](mailto:tommi.mikkonen@tuni.fi)

Received 24 January 2022; revised 18 February 2022; accepted 20 February 2022; posted 22 February 2022; published 25 March 2022

**We investigate the noise transfer mechanism from the light source intensity fluctuations to the acoustic signal in Fourier transform photoacoustic spectroscopy (FT-PAS). This noise coupling is expected to be reduced in FT-PAS compared with conventional Fourier transform spectroscopy, as only the specific spectral components that are absorbed by the probed sample contribute to the noise level. We employ an incoherent supercontinuum (SC) light source in our experiments and observe a linear relation between the sample gas concentration and the detected noise level, which significantly reduces the influence of the SC noise on the detection limit. Based on our experimental results, we derive a model for the noise level, which establishes the foundation for practical sensitive implementation of FT-PAS.**

Published by Optica Publishing Group under the terms of the [Creative Commons Attribution 4.0 License](#). Further distribution of this work must maintain attribution to the author(s) and the published article's title, journal citation, and DOI.

<https://doi.org/10.1364/OL.454461>

Fourier transform spectroscopy (FTS) is a well-established gas sensing technique applied widely in industry and research. In FTS, an absorption spectrum is measured by down-converting the optical frequencies of broadband light to audio frequencies using a scanning interferometer [1]. The absorption of light is conventionally observed through light attenuation in a gas medium, but an attractive alternative is provided by a photoacoustic (PA) detection scheme. PA detection exploits the PA effect to convert absorbed electromagnetic radiation into an acoustic wave using a modulated light source that leads to periodic light absorption and thermal relaxations in a closed gas cell. The technique is background-free, very sensitive, requires only a small sample volume [2], and can be combined with FTS in so-called Fourier transform photoacoustic spectroscopy (FT-PAS) [3]. In FT-PAS, the scanning interferometer acts as the light modulator, which together with a non-resonant gas cell and a suitable microphone enables simultaneous detection of the entire absorption spectrum.

Although allowing for the fast acquisition of hundreds of spectral components, the parallel detection in FTS leads to increased noise sensitivity arising from the intensity fluctuations of the light source, a drawback known as the multiplex disadvantage [4,5]. Specifically, all wavenumber components emitted by the

light source and reaching the detector contribute to the noise level, such that intensity noise at a specific (and detected) spectral component induces noise for all detected frequencies. In FT-PAS, the coupling of the source noise differs significantly from FTS, as only the spectral components which are absorbed in the gas cell contribute to the detected signal, and therefore intensity fluctuations only at the absorbed wavenumbers will lead to noise at frequencies within the detected bandwidth. A direct consequence is that the noise level in FT-PAS is expected to be considerably lower than in FTS when both systems are source noise limited.

This source-induced noise is proportional to the intensity noise of the light source, and thus the multiplex disadvantage is generally not a major problem in the infrared region when employing a thermal or another continuous wave light source when the detector noise dominates over the source noise. However, thermal emitters are spatially incoherent with low power spectral density, which may limit the performance. With the recent development of broadband, spatially coherent light sources especially in the mid-infrared spectral region, there has been significant interest to apply them in FTS and FT-PAS experiments [6–12]. Supercontinuum (SC) sources generated with nanosecond or picosecond pump lasers [13] are often preferred in real-world applications as compared with other broadband coherent sources such as optical frequency combs as they are more compact and cost-effective. A major drawback, however, associated with these sources is their pulse-to-pulse intensity fluctuations, which have been shown to yield increased noise level in FTS [8]. Similar results have also been reported for FT-PAS [10], but the effect of intensity fluctuations of the light source on the detection noise has not been fully investigated.

Here, we fill this gap and study the intensity noise transfer mechanism in an FT-PAS system with an incoherent SC as the light source. We quantify the noise of the SC by measuring the pulse-to-pulse intensity fluctuations in various wavenumber bands and study the dependence between the sample gas concentration and the noise level in a simple case of a single absorber. This dependence is found to be linear, confirming intensity noise coupling from the SC to the acoustic signal via light absorption by gas molecules. We also derive a model for the noise level and demonstrate a simple approach for noise reduction. Our results lead to a better understanding of the noise characteristics in FT-PAS and open novel perspectives for highly sensitive broadband gas sensing applications.

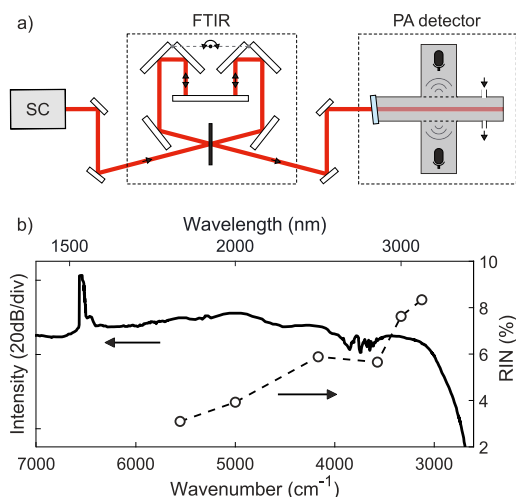


**Fig. 1.** (a) Experimental setup: Fourier transform infrared spectrometer (FTIR). (b) Low wavenumber (long wavelength) part of the SC spectrum (solid line, left-hand axis), and associated relative intensity noise (RIN) (dashed line, right-hand axis).

Our experimental FT-PAS system is illustrated in Fig. 1(a). The SC spectrum extending up to 3700 nm ( $2700\text{ cm}^{-1}$ ) is generated by injecting 10 kW, 0.6 ns pulses at  $1547\text{ nm}$  ( $6464\text{ cm}^{-1}$ ) wavelength and with 70 kHz repetition rate from a gain-switched erbium-doped fiber laser (Keopsys-PEFL-K09) into the anomalous dispersion regime of a 4-m-long silica dispersion shifted fiber connected to a 8-m-long fluoride fiber. The low wavenumber part of the SC spectrum is shown in Fig. 1(b) (solid line). The SC generation process is seeded by modulation instability and soliton dynamics (see Ref. [14] for a more detailed description) resulting in large pulse-to-pulse intensity fluctuations [13].

The intensity noise of the SC source was characterized by measuring 70,000 consecutive pulses in different wavenumber bands between  $3000\text{ cm}^{-1}$  ( $3300\text{ nm}$ ) and  $5600\text{ cm}^{-1}$  ( $1800\text{ nm}$ ). The SC light was attenuated to prevent signal saturation, wavenumber bands of  $10\text{ cm}^{-1}$  were selected using a monochromator (Spectral Products DK480 1/2), and the spectrally filtered light was detected using a HgCdTe amplified detector (Thorlabs PDA10jT-EC, 160 kHz) and a fast oscilloscope (LeCroy WaveRunner 6100A, 1 GHz). For each wavenumber band, we calculated the RIN defined as the ratio of the intensity standard deviation to the mean intensity. The pulse-to-pulse fluctuations in different wavelength bands presented in Fig. 1(b) (dashed line) show characteristic increase farther from the pump residue with values in the range 3.1–8.3%, in agreement with previous studies [15,16]. This increase arises from statistically rare high peak power solitons, which experience more efficient Raman-shift dynamics [15]. The noise spectrum of the SC intensity fluctuations (not shown here) for each wavenumber band and obtained by calculating the fast Fourier transform from the time series of the pulse intensities exhibits white noise characteristics as previously reported in Ref. [17].

In the FT-PAS system, the SC with 230 mW of optical power is collimated into a beam having a diameter of 4 mm using a silver reflective collimator and directed into a scanning FTIR,

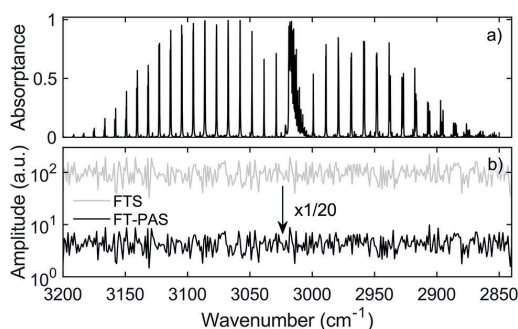


**Fig. 2.** Simulated coupling of light source intensity noise in FTS and FT-PAS. (a) Absorbance spectrum of 2% of  $\text{CH}_4$  in a 5 cm gas cell (according to HITRAN [19]), which acts as a spectral separator between FT-PAS and FTS. (b) Noise spectra for the two detection principles.

where each wavenumber of the source is modulated at a unique Fourier frequency at the output. The optical path difference scan velocity of the FTIR (Pendum interferometer, Gasera) is approximately  $0.2\text{ cm/s}$ , monitored with a reference diode laser ( $14,700\text{ cm}^{-1}$ ,  $680\text{ nm}$ ), which results in modulation frequencies of  $550\text{--}1000\text{ Hz}$  for the wavenumber range  $2700\text{--}5000\text{ cm}^{-1}$ . The spectral resolution of the FTIR is  $13\text{ cm}^{-1}$ , and 30% of the incident radiation is transmitted. The modulated SC light is focused into a non-resonant PA cell (Gasera) using a parabolic mirror ( $f = 4\text{ cm}$ ). The cylindrical cell is gold-coated, 5 cm long with a diameter of 4 mm and sealed with a  $\text{BaF}_2$  window. The temperature inside the cell is  $23^\circ\text{C}$ , and a pump system delivering gases inside the chamber is incorporated into the PA detector. Pressure variations inside the cell are monitored with two sensitive, interferometrically read silicon cantilever microphones [18] located on the opposite walls of the cell. The frequency response of the PA cell allows modulation frequencies up to  $1000\text{ Hz}$ . A single two-sided interferogram is acquired in 2.7 s, from which the absorption spectrum is calculated using a fast Fourier transform algorithm.

To illustrate differences in light source noise coupling between FTS and FT-PAS, we simulated the intensity noise in a simplified system excluding the interferometer part of the spectrometers. Only intensity noise is considered, with pulse-to-pulse fluctuations assumed to be normally distributed, with identical magnitude for each spectral component and positively correlated, as is typically observed for noisy SC sources on the long-wavelength side of the spectrum away from the pump residue. The simulated 5-cm-long gas cell contains 2% of methane ( $\text{CH}_4$ ) with absorption spectrum illustrated in Fig. 2(a). All transmitted light is detected in FTS while only the absorbed part is detected in FT-PAS, yielding a 20-fold decrease in the intensity noise level in FT-PAS compared with FTS as shown in Fig. 2(b). Generally, we found that reduced total absorption results in lower overall intensity noise level in FT-PAS.

Coupling of SC intensity fluctuations to the FT-PAS signal noise was then studied experimentally by characterizing different gases: water vapor ( $\text{H}_2\text{O}$ ) at two concentrations and pure nitrogen ( $\text{N}_2$ ). For reference, we also measured the FT-PAS signal in the absence of light. The recorded spectra averaged over 20 scans (corresponding to a total acquisition time of 54 s) are

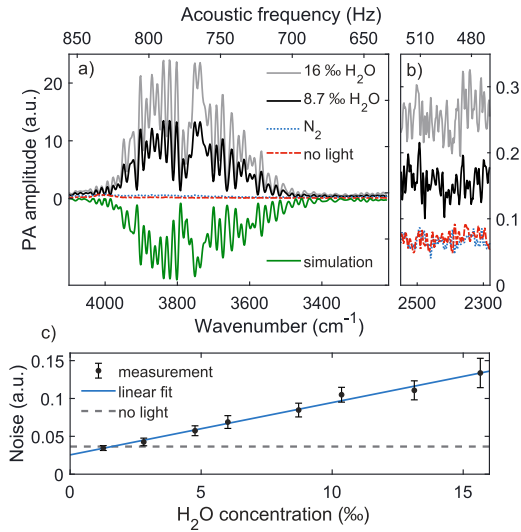


**Fig. 3.** (a) Measured PA spectra of H<sub>2</sub>O (two concentrations) and N<sub>2</sub>, together with the spectrum with no light entering the PA cell, and a simulated absorbance spectrum of H<sub>2</sub>O (reversed). The measurement resolution is 13 cm<sup>-1</sup>, and all spectra were averaged over 20 scans. (b) An enlargement of the noise level in the area of no optical power. Curves are ordered according to the legend. (c) Calculated noise level as a function of H<sub>2</sub>O concentration.

shown in Fig. 3(a). Figure 3(b) highlights the measured PA amplitude outside the SC spectrum where no absorption occurs, therefore illustrating pure noise. The total average power of the SC injected into the PA cell was 69 mW, with 20 mW in the spectral region below 4300 cm<sup>-1</sup> (2325 nm). The concentration (as volume mixing ratio) of H<sub>2</sub>O was varied by mixing air with N<sub>2</sub>. The concentration value was determined afterwards using a single calibration measurement of 400 ppm of CH<sub>4</sub> and simulated reference spectra of CH<sub>4</sub> and H<sub>2</sub>O [green line in Fig. 3(a)] based on the HITRAN database [19], the instrument function and the SC spectrum.

One can see that the noise level increases with H<sub>2</sub>O concentration. This is because a higher concentration results in increased absorption by the H<sub>2</sub>O molecules inside the PA cell, leading to enhanced intensity noise coupling to the PA signal. As the SC exhibits white noise characteristics, the noise is spread across all the detected acoustic frequencies. The baselines in Fig. 3(b) are different, because all the values in the recorded spectra are positive, and averaging noise with only positive values results in a higher baseline for higher noise. The background spectrum (measured with no light) shows the minimum of the noise level, dominated by the random collisions of gas molecules to the cantilevers [18]. A distinct peak in the background at 4000 cm<sup>-1</sup> is attributed to a small background interference of the PA cell. The spectrum with N<sub>2</sub> in the cell shows similar noise level as the case with no light entering the cell, but a small background offset is visible at wavenumbers falling under the SC spectrum. This offset is most likely due to absorption by the PA cell window as suggested in previous studies [12].

Additional measurements for different H<sub>2</sub>O concentrations indicate that the noise–concentration dependence is linear as

illustrated in Fig. 3(c), where the measured noise level is plotted against H<sub>2</sub>O concentration. The noise was calculated separately for 20 different scans as the standard deviation of the PA amplitude over the spectral range from 2200 cm<sup>-1</sup> through 2500 cm<sup>-1</sup>, which is outside the SC spectrum. Figure 3(c) shows the averaged noise level for each concentration and the standard deviation of the noise within these 20 spectra. We note that similar behavior has previously been reported in single-frequency PAS [20,21]. Interestingly, because the PA amplitude also depends linearly on the concentration, the linear dependence of the noise on the concentration leads to a signal-to-noise ratio that is independent of the gas concentration, assuming that no other absorbing gases are present in the cell and the system is limited by the light source noise.

From the experimental findings, we next derive a model for the observed noise level in the general case including several absorbers. The noise  $\sigma$  has two main contributions, the intensity noise of the SC ( $\sigma_{SC}$ ) and the thermal fluctuations of gas molecules ( $\sigma_T$ ):  $\sigma = (\sigma_{SC}^2 + \sigma_T^2)^{1/2}$ . The intensity fluctuations of the SC are coupled to the PA signal through absorption, each absorbed wavenumber  $\nu$  producing its own noise contribution  $\sigma_{SC}(\nu)$  to the total SC-induced noise  $\sigma_{SC} = [\int_{\nu_{min}}^{\nu_{max}} \sigma_{SC}^2(\nu) d\nu]^{1/2}$ . Similar to the linear dependence of the PA amplitude on the optical power and the total absorption coefficient  $\alpha_{tot}$  (assuming a low optical density), each noise component  $\sigma_{SC}(\nu)$  is linearly proportional to the intensity fluctuations  $RIN(\nu)$  and  $\alpha_{tot}(\nu)$ :

$$\sigma_{SC}(\nu) \propto RIN(\nu) \alpha_{tot}(\nu) \propto RIN(\nu) \sum_m [\sigma_m(\nu) c_m], \quad (1)$$

where  $\alpha_{tot}$  has been written in terms of the molecule  $m$  absorption cross sections  $\sigma_m$  and concentrations  $c_m$ . For a single absorbing species in the gas cell,  $\sigma_{SC}$  is directly proportional to the concentration in agreement with the data in Fig. 3(c) where the slight nonlinearity at low concentrations (caused by thermal noise) is not visible. The observed noise  $\sigma$  is expected to decrease with the inverse square root of the averaging time, as both noise contributions are white in a narrow frequency region. We confirmed this by measuring 400 consecutive scans of 1.3% per thousand of H<sub>2</sub>O and calculating the Allan deviation curve (not shown), which displays averaging over 100 s, limited by a drift most likely caused by H<sub>2</sub>O desorption.

The model above suggests two general approaches to decrease the noise level. The first approach is to reduce the intensity fluctuations of the SC source (especially at low frequencies). When using an incoherent SC, this can be realized, e.g., by operating in spectral regions closer to the pump where intensity fluctuations are reduced. Although less practical, one may also employ coherent SC sources which can virtually cut the noise to the minimum level [11,12]. The second approach is to minimize the absorbed radiation in the PA cell. This approach becomes particularly effective when the measurement bandwidth of the system includes unutilized absorption bands from the gases inside the cell. In this case, it is especially important to minimize the contribution of potentially interfering H<sub>2</sub>O, either by modifying the source spectrum, e.g., using spectral filters, or using sample pre-treatment for water removal.

We demonstrated this latter approach for CH<sub>4</sub> detection by spectrally filtering the SC light, as CH<sub>4</sub> and H<sub>2</sub>O have well separated absorption bands. Specifically, we measured the C–H stretch band of CH<sub>4</sub> (400 ppm) in air with the full SC spectrum and a spectrally filtered SC using a long-pass filter with a cutoff at 3346 cm<sup>-1</sup> (Northumbria Optical Coatings, SLWP-2989). After

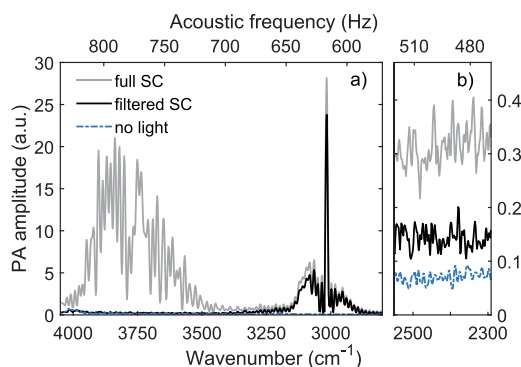


**Fig. 4.** (a) Measured PA spectra of  $\text{CH}_4$  in air with and without long-pass cutoff at  $3346\text{ cm}^{-1}$  filtering of the SC, together with the spectrum with no light entering the PA cell. (b) An enlargement of the noise level in the area of no optical power.

filtering, the SC spectrum corresponds to an average power of 25 mW, 30% of which was again injected to the PA cell. The measurements were averaged over 20 scans for a total acquisition time of 54 s, and the resulting spectra are shown in Fig. 4 together with the background spectrum (corresponding to the case when no light is injected into the FT-PAS system).

One can clearly see that the spectral filtering decreases the noise level by a factor of two compared with the case where the full SC spectrum is used. This decrease arises from the absence of light absorption by  $\text{H}_2\text{O}$  molecules around  $3750\text{ cm}^{-1}$ , in agreement with our noise model above (which also estimates the factor of noise reduction correctly). Moreover, the noise level difference between the filtered SC measurements and the background noise (in the absence of light) is also twofold. We calculated the detection limit as  $3\sigma_c/S$  for  $\text{CH}_4$  both with and without the spectral filter using the strongest spectral peak at  $3016\text{ cm}^{-1}$  as the signal  $S$ . A common practice would be to determine the noise level from a non-absorbing part of the same spectrum. However, the noise level in this case does not reflect the noise level at low target gas concentrations as shown in Fig. 3(c). The target gas couples noise to the signal, and this noise contribution practically vanishes when the target gas concentration is very low, i.e., close to the detection limit. Therefore, for an accurate estimation of the detection limit, the noise level should be calculated from a measurement with no target gas present. The conventional approach using a noise level calculated from the measurement with the target gas present has been used for determining the detection limit in previous FT-PAS studies [10–12], and thus we believe that their performance has been underestimated. We calculated the noise levels from separate methane-free measurements using the procedure described previously and achieved detection limits of 320 ppb and 930 ppb with and without the filter, respectively. While 320 ppb is among the lowest detection limits of  $\text{CH}_4$  reported with FT-PAS [10–12], a reliable comparison between the systems is complicated by different spectral resolutions and the inaccurately estimated noise levels in the previous studies.

We have investigated the noise characteristics in a SC-based FT-PAS system and derived a model describing the increase

of noise observed for higher sample gas concentrations. Our measurements show that the noise increase arises from coupling of the light source intensity fluctuations to the PA signal via light absorption by gas molecules. We have further shown that the noise can be reduced by limiting the amount of excess absorption in the PA cell and which can be in some cases realized by simple spectral filtering of the light source. With this approach, we have demonstrated a detection limit of 320 ppb for  $\text{CH}_4$ , which is among the lowest detection limits of  $\text{CH}_4$  reported with FT-PAS.

**Funding.** Graduate School of Tampere University; Academy of Finland Flagship Programme PREIN (320165).

**Disclosures.** The authors declare no conflicts of interest.

**Data availability.** Data underlying the results presented in this Letter are not publicly available at this time but may be obtained from the authors upon reasonable request.

## REFERENCES

1. R. Bell, *Introductory Fourier Transform Spectroscopy* (Elsevier, 2012).
2. F. J. Harren, J. Mandon, and S. M. Cristescu, in *Encyclopedia of Analytical Chemistry: Applications, Theory and Instrumentation* (Wiley, 2006).
3. M. M. Farrow, R. K. Burnham, and E. M. Eyring, *Appl. Phys. Lett.* **33**, 735 (1978).
4. F. Plankey, T. Glenn, L. Hart, and J. Winefordner, *Anal. Chem.* **46**, 1000 (1974).
5. T. Hirschfeld, *Appl. Spectrosc.* **30**, 234 (1976).
6. J. Mandon, E. Sorokin, I. T. Sorokina, G. Guelachvili, and N. Picqué, *Opt. Lett.* **33**, 285 (2008).
7. J. Mandon, G. Guelachvili, and N. Picqué, *Nat. Photonics* **3**, 99 (2009).
8. C. A. Michaels, T. Masiello, and P. M. Chu, *Appl. Spectrosc.* **63**, 538 (2009).
9. V. V. Goncharov and G. E. Hall, *J. Chem. Phys.* **145**, 084201 (2016).
10. T. Mikkonen, C. Amiot, A. Aalto, K. Patokoski, G. Genty, and J. Toivonen, *Opt. Lett.* **43**, 5094 (2018).
11. I. Sadiek, T. Mikkonen, M. Vainio, J. Toivonen, and A. Foltynowicz, *Phys. Chem. Chem. Phys.* **20**, 27849 (2018).
12. J. Karhu, T. Tomberg, F. S. Vieira, G. Genoud, V. Hänninen, M. Vainio, M. Metsälä, T. Hieta, S. Bell, and L. Halonen, *Opt. Lett.* **44**, 1142 (2019).
13. J. M. Dudley, G. Genty, and S. Coen, *Rev. Mod. Phys.* **78**, 1135 (2006).
14. C. Amiot, A. Aalto, P. Ryczkowski, J. Toivonen, and G. Genty, *Appl. Phys. Lett.* **111**, 061103 (2017).
15. A. Kudlinski, B. Barvau, A. Leray, C. Spriet, L. Hélot, and A. Mussot, *Opt. Express* **18**, 27445 (2010).
16. M. K. Dasa, C. Markos, M. Maria, C. R. Petersen, P. M. Moselund, and O. Bang, *Biomed. Opt. Express* **9**, 1762 (2018).
17. K. L. Corwin, N. R. Newbury, J. M. Dudley, S. Coen, S. A. Diddams, K. Weber, and R. Windeler, *Phys. Rev. Lett.* **90**, 113904 (2003).
18. T. Kuusela and J. Kauppinen, *Appl. Spectrosc. Rev.* **42**, 443 (2007).
19. L. Rothman, I. Gordon, and Y. Babikov, *et al.*, *J. Quant. Spectrosc. Radiat. Transfer* **130**, 4 (2013).
20. C. Hirschmann, J. Lehtinen, J. Uotila, S. Ojala, and R. Keiski, *Appl. Phys. B* **111**, 603 (2013).
21. J. Peltola, M. Vainio, T. Hieta, J. Uotila, S. Sinisalo, M. Metsälä, M. Siltanen, and L. Halonen, *Opt. Express* **21**, 10240 (2013).



# PUBLICATION

## IV

**Sensitive multi-species photoacoustic gas detection based on mid-infrared  
supercontinuum source and miniature multipass cell**

T. Mikkonen, T. Hieta, G. Genty and J. Toivonen

*Physical Chemistry Chemical Physics* 24.(2022), 19481–19487

**Publication reprinted with the permission of the copyright holders**





Cite this: *Phys. Chem. Chem. Phys.*,  
2022, 24, 19481

# Sensitive multi-species photoacoustic gas detection based on mid-infrared supercontinuum source and miniature multipass cell

Tommi Mikkonen,<sup>a</sup> Tuomas Hieta,<sup>b</sup> Goëry Genty<sup>a</sup> and Juha Toivonen<sup>\*a</sup>

We report multipass broadband photoacoustic spectroscopy of trace gases in the mid-infrared. The measurement principle of the sensor relies on supercontinuum-based Fourier transform photoacoustic spectroscopy (FT-PAS), in which a scanning interferometer modulates the intensity of a mid-infrared supercontinuum light source and a cantilever microphone is employed for sensitive photoacoustic detection. With a custom-built external Herriott cell, the supercontinuum beam propagates ten times through a miniature and acoustically non-resonant gas cell. The performance of the FT-PAS system is demonstrated by measuring the fundamental C–H stretch bands of various hydrocarbons. A noise equivalent detection limit of 11 ppb is obtained for methane (40 s averaging time, 15  $\mu\text{W cm}^{-1}$  incident power spectral density, 4  $\text{cm}^{-1}$  resolution), which is an improvement by a factor of 12 compared to the best previous FT-PAS systems. High linearity and good stability of the sensor provide reliable identification of individual species from a gas mixture with strong spectral overlap, laying the foundation for sensitive and selective multi-species detection in small sample volumes.

Received 14th April 2022,  
Accepted 30th July 2022

DOI: 10.1039/d2cp01731h

rsc.li/pccp

## 1 Introduction

Photoacoustic spectroscopy (PAS) is an extensively used technique for trace gas sensing due to its high sensitivity and low gas consumption.<sup>1,2</sup> These properties result from a unique operation principle converting the detection from optical into acoustic domain. Modulated incident radiation induces periodic absorption in a closed gas cell, which leads to periodic pressure variations *via* molecular thermal relaxation. The pressure waves proportional to the gas concentration are typically detected with a capacitive microphone. More recently, detection schemes utilizing pressure transducers with enhanced sensitivity such as piezoelectric quartz tuning forks and optically read cantilevers have been demonstrated.<sup>3–5</sup> The detection of multiple species with high selectivity requires a spectrally broadband system that can be implemented using a Fourier transform photoacoustic spectroscopy (FT-PAS) approach.<sup>6,7</sup> In FT-PAS, a scanning interferometer modulates each wavenumber of a broadband light source at a distinct acoustic frequency, after which all the pressure waves at these frequencies are simultaneously detected in an acoustically non-resonant gas cell. Broadband thermal emitters are typically used as the light source in FT-PAS, but recently supercontinuum (SC) sources

and frequency combs have been shown to yield significantly better performance.<sup>8–12</sup>

The spatial coherence of these light sources enables efficient coupling to an optical cavity, which amplifies optical power inside the gas cell resulting in a proportional enhancement in the photoacoustic (PA) signal and sensitivity. Although non-resonant multipass cavities provide less amplification than resonant cavities,<sup>13,14</sup> they are often preferred due to simpler operation, better mid-infrared (mid-IR) availability and wider spectral bandwidth, which is especially crucial for broadband systems. In single-frequency PAS, various types of multipass cavities have been reported, including simple zigzag configurations,<sup>12,15–17</sup> circular cells,<sup>18</sup> retroreflectors<sup>19</sup> and Herriott cells<sup>20–24</sup> that are especially attractive for conventional cylindrical gas cells. The reflectors in most miniature multipass systems are internal,<sup>15–18,24</sup> *i.e.* in contact with the gas medium, to eliminate optical power losses from windows, and the background signal from these mirrors is minimized by ways of wavelength modulation<sup>17,18,24</sup> or acoustic resonances,<sup>15,16</sup> which however are not applicable to FT-PAS.

Here, we report the first broadband (spectral bandwidth over 100  $\text{cm}^{-1}$ ) multipass PAS system in the mid-IR by employing an external Herriott-type mirror configuration. Radiation from a mid-IR SC source is guided ten times through a miniature gas cell equipped with a cantilever microphone that has been shown to perform exceptionally well in broadband PA detection due to its sensitivity over a wide frequency range.<sup>25</sup> The multipass system provides a sixfold signal enhancement in a

<sup>a</sup> Photonics Laboratory, Physics Unit, Tampere University, FI-33014 Tampere, Finland. E-mail: juha.toivonen@tuni.fi

<sup>b</sup> Gasera Ltd., Lemminkäisenkatu 59, FI-20520 Turku, Finland

bandwidth of  $400\text{ cm}^{-1}$  around  $3000\text{ cm}^{-1}$ , which results in an order of magnitude improvement in sensitivity for FT-PAS systems and detection limits for hydrocarbons in the low parts per billion (ppb) level. We also study the stability of the system and demonstrate its high selectivity showing great promise for multi-species trace gas detection.

## 2 Experimental

The experimental setup is illustrated in Fig. 1. A home-built SC source is generated by injecting sub-nanosecond pulses with 70 kHz repetition rate into a combination of optical fibers, yielding a spectrum that extends from 1547 nm ( $6464\text{ cm}^{-1}$ ) to 3700 nm ( $2700\text{ cm}^{-1}$ ).<sup>8,26</sup> The SC light is collimated into a beam of 2 mm diameter using a reflective fiber collimator, and then spectrally filtered. A long-pass filter with a cut-off at 2989 nm ( $3346\text{ cm}^{-1}$ , Northumbria Optical Coatings SLWP-2989) removes optical power from spectral regions not under interest and thus suppresses excess absorption from water ( $\text{H}_2\text{O}$ ) molecules in the gas cell. As we have shown previously,<sup>9</sup> eliminating unutilized absorption decreases the noise level significantly, as the intensity noise of the SC is coupled to the PA signal *via* light absorption by gas molecules. The filtered SC light with 21 mW of optical power is directed into a Fourier transform spectrometer (FTS, Bruker IRCube), whose maximum spectral resolution is  $1\text{ cm}^{-1}$ . The optical path difference scanning velocity of the FTS is about  $1\text{ mm s}^{-1}$ , which leads to modulation frequencies of 270–340 Hz at the wavenumber range of the filtered SC. At such low modulation frequencies the relaxation processes do not limit the sensitivity of the system and the response is similar for different gas mixtures.

About 30% of the incoming light is transmitted through the FTS and focused towards a commercial PA analyser (Gasera PA201) using a parabolic mirror ( $f = 20\text{ cm}$ ). Within the PA analyser, a miniature non-resonant gas cell is 95 mm long,

4 mm in diameter, about 7 ml by total volume and sealed with anti-reflection coated  $\text{BaF}_2$  windows (Thorlabs WG00530-E). Four mass flow controllers (Brooks Instruments 0154 and three pieces of Bronkhorst F-201CV) and a gas exchange system incorporated into the PA analyser control the gas flow into the cell with pressure and temperature set to 1 bar and  $23\text{ }^\circ\text{C}$ , respectively.

The multipass configuration for this gas cell was designed through careful modelling of the optical system using Matlab. Specifically, we simulated the propagation of a Gaussian beam<sup>27</sup> in different Herriott configurations<sup>28,29</sup> by varying the properties of the mirrors (radius of curvature and separation) and the input beam (radius of curvature and beam waist). The optimum number of passes was found to be ten using mirrors with 200 mm radius of curvature and separated by 138 mm. Such gold-plated spherical mirrors (LBP Optics) with diameters of 12.7 mm were placed outside the gas cell, where the SC radiation is guided off-axially through a small aperture (1 mm in diameter, displaced 1.1 mm from the mirror center) in the front mirror. A simulated intensity pattern at the front mirror is shown at the bottom-right corner in Fig. 1. A theoretical signal enhancement (dashed black line in Fig. 2(b)) for this multipass system is slightly wavenumber dependent around 6.2, considering the transmittance curve of the windows (96% on average) reported by the manufacturer and a constant 98% mirror reflectance.

An integrated microphone placed on the side of the gas cell is a thin (a few  $\mu\text{m}$ ) silicon slab with an area of a few  $\text{mm}^2$

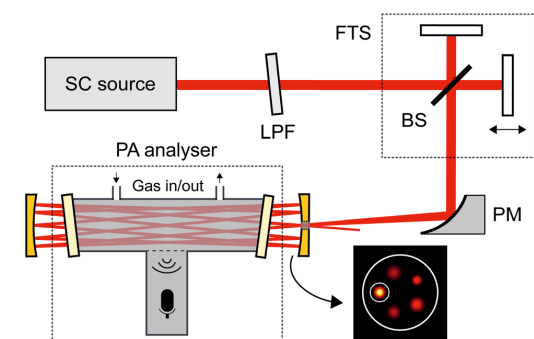


Fig. 1 A schematic of the experimental setup: SC – supercontinuum; LPF – long-pass filter; FTS – Fourier transform spectrometer; BS – beam splitter; PM – parabolic mirror; PA – photoacoustic. The simulation on the bottom-right corner shows the theoretical intensity pattern at the front mirror. The smaller white ring represents the input aperture and the larger ring illustrates the gas cell.

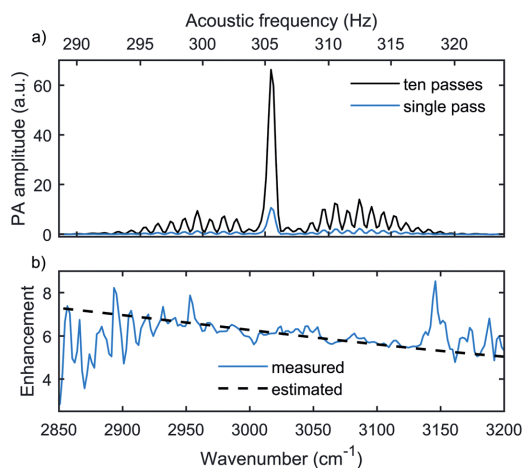


Fig. 2 (a) Measured FT-PAS spectra of 36 ppm  $\text{CH}_4$  in  $\text{N}_2$  using the multipass enhancement (black line) and allowing only one beam pass through the gas cell (blue line). Both spectra were averaged over 40 s (eight scans) at a spectral resolution of  $4\text{ cm}^{-1}$ . We note that the maximum resolution of the FTS ( $1\text{ cm}^{-1}$ ) was not utilized here. In addition to the optical domain on the bottom, the corresponding modulation frequencies in the acoustic domain are shown on the top. (b) Signal enhancement using the multipass arrangement, evaluated from the measured spectra (solid blue line) and estimated from the window transmittance and mirror reflectance (dashed black line).

attached to its frame only from one side.<sup>30</sup> Pressure variations displace the free end of the cantilever whose position is monitored with a spatial-type interferometer.<sup>31,32</sup> The microphone with a bandwidth of about 700 Hz records an interferogram containing information on all the excited acoustic waves whose frequencies are directly proportional to specific absorbed wavenumbers. A three-term Blackman–Harris apodization function is applied for the resampled (reference HeNe laser) interferogram, and the absorption spectrum is obtained by Fourier transform.

### 3 Results and discussion

#### Multipass enhancement and system performance

We measured the rovibrational absorption spectra of the fundamental C–H stretch band of methane (CH<sub>4</sub>) around 3000 cm<sup>−1</sup> to demonstrate multipass enhancement and to compare the performance of the system with previous studies. Fig. 2 shows the absorption spectrum of 36 parts per million (ppm, volume mixing ratio) of CH<sub>4</sub> in nitrogen (N<sub>2</sub>), measured both with a single and ten beam-pass through the gas cell. Single pass was realized by blocking the beam before the back spherical mirror. Each spectrum was averaged over eight scans at a spectral resolution of 4 cm<sup>−1</sup> resulting in a total averaging time of 40 s. A small H<sub>2</sub>O residual was subtracted from both spectra using a methane-free spectral region with water absorption around 3200 cm<sup>−1</sup> and a separate pure H<sub>2</sub>O measurement. We calculated the detection enhancement arising from the multipass configuration by comparing the raw spectra with and without the multipass enhancement. This division shown in Fig. 2(b) (solid blue line) is in excellent agreement with the theoretical prediction of a signal enhancement of 5–8 at 2800–3200 cm<sup>−1</sup>, especially in a region with a high signal-to-noise ratio.

For the multipass enhanced system, we estimated the limit of detection as  $LOD = 3\sigma c/S$ , where  $c$  is the gas concentration (36 ppm),  $S$  is the strongest spectral peak evaluated at 3017 cm<sup>−1</sup> and  $\sigma$  is the noise level calculated from a separate 40 seconds long recording with only N<sub>2</sub> in the gas cell, as this represents the noise level at low CH<sub>4</sub> concentrations.<sup>9</sup> Due to a small H<sub>2</sub>O residual in the N<sub>2</sub> measurement, the noise level was calculated as the standard deviation of the baseline at 2200–2800 cm<sup>−1</sup>. As will be shown later, this choice is justified by the flat noise level across the investigated wavenumber region. Based on this calculation, a detection limit of 32 ppb in 40 s for CH<sub>4</sub> was obtained.

The performance of our system is compared to that of previous FT-PAS studies in Table 1. Note that the power spectral density is reported without any multipass enhancement (a double-pass arrangement was used in ref. 8, 10 and 11). Significantly, our system shows a factor of 12 improvement in the time-normalized detection limit compared to the best previous FT-PAS system<sup>9</sup> due to the multipass enhancement and a more sensitive PA analyser. In general, the differences between the LODs in Table 1 also result from the power spectral densities, spectral resolutions and from the procedures for estimating the noise level at the detection limit. The LOD

**Table 1** A summary of recent FT-PAS experiments using supercontinuum (SC) or optical frequency comb (OFC) light sources in terms of CH<sub>4</sub> limit of detection (LOD, 3 $\sigma$ , 100 s), spectral resolution and incident power spectral density (PSD)

Source	LOD (ppb)	Res. (cm <sup>−1</sup> )	PSD ( $\mu$ W cm <sup>−1</sup> )	Ref.
SC	990	4	31	8
OFC	3300	0.033	21	10
OFC	660	0.02	240	11
SC	240	13	19	9
SC	20	4	18	This work

obtained here is comparable with other relatively simple broadband mid-IR techniques such as SC-based direct absorption spectroscopy and dual-comb spectroscopy with achieved CH<sub>4</sub> detection limits of 47 ppb and 2.4 ppm (for ~100 times weaker absorption cross sections), respectively.<sup>33,34</sup> However, both of these techniques require two orders of magnitude larger sample volumes compared to our approach.

The performance of the system was further characterized by measuring the C–H stretch bands of 30 ppm ethane (C<sub>2</sub>H<sub>6</sub>) and 100 ppm ethene (C<sub>2</sub>H<sub>4</sub>) separately at 1 cm<sup>−1</sup> spectral resolution. The raw spectra were averaged over 200 s (ten scans), corrected for H<sub>2</sub>O absorption using the procedure described for CH<sub>4</sub> and normalized by the spectral envelope of the SC measured with a monochromator (Spectral Products DK480 1/2) and numerically corrected by the transmittance of the filter and the windows. The raw C<sub>2</sub>H<sub>4</sub> spectrum and the H<sub>2</sub>O residual are shown in Fig. 3(a). The corrected spectra in Fig. 3(b) are in excellent agreement with simulations based on the HITRAN database<sup>35</sup> and the instrument lineshape function. The increase in the baseline at the low wavenumber part of the C<sub>2</sub>H<sub>6</sub> spectrum is due to low power spectral density of the SC in this region, which amplifies the background noise in the normalization process.

#### Calibration and noise characterization

We studied the effect of the gas concentration on the amplitude of the measured photoacoustic signal and the noise level. The concentration–amplitude dependence is used for calibration, which is always required in PAS, and the noise relation gives insight into the unique noise mechanism of FT-PAS studied in more detail elsewhere.<sup>9</sup> Samples of C<sub>2</sub>H<sub>4</sub> with varying concentration between 6 and 900 ppm were prepared by diluting C<sub>2</sub>H<sub>4</sub> from a 1% gas bottle to N<sub>2</sub>. The measured spectra for the different concentrations with 1 cm<sup>−1</sup> resolution and averaged over 100 s (5 scans) are shown in Fig. 4(a) on a logarithmic scale. One can see how both the signal amplitude and noise level increase with the concentration. We also observe that within a single measurement, the noise level remains constant across the characterized wavenumber range, which justifies the use of the noise value in a specific region (red area in Fig. 4(a)) to assess the detection limit. For each spectrum, the amplitude was calculated from the strongest spectral peak of C<sub>2</sub>H<sub>4</sub> after H<sub>2</sub>O subtraction, and the noise level was estimated as the standard deviation of the raw PA amplitude in an absorption-free region at 2600–2800 cm<sup>−1</sup>.

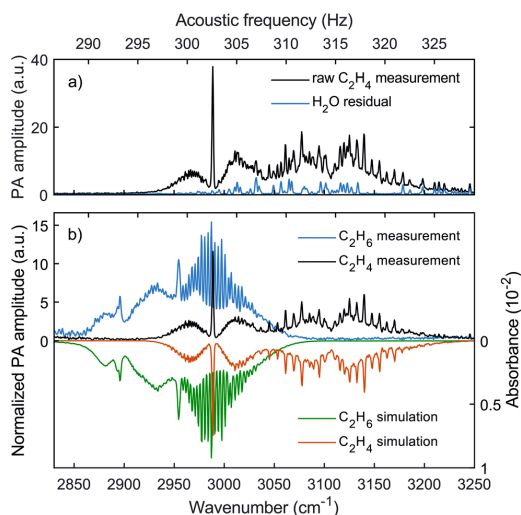


Fig. 3 (a) A raw FT-PAS spectrum of 30 ppm  $\text{C}_2\text{H}_6$  and residual  $\text{H}_2\text{O}$ . (b) Absorption spectra of 30 ppm  $\text{C}_2\text{H}_6$  and 100 ppm  $\text{C}_2\text{H}_4$  at  $1\text{ cm}^{-1}$  spectral resolution, obtained experimentally (left axis) by subtracting the  $\text{H}_2\text{O}$  residual from the raw spectra and normalizing by the envelope of the SC spectrum, and modelled (right axis, inverted) using the HITRAN database and the instrument lineshape function.

Fig. 4(b) and (c) illustrate quantitatively the dependence of the signal amplitude and noise as a function of  $\text{C}_2\text{H}_4$  concentration up to 200 ppm. Uncertainties in the  $\text{C}_2\text{H}_4$  concentrations result from dilution errors caused by the gas bottle uncertainty (2%) and the errors in the mass flow controllers (1–17% depending on the concentration and corresponding to absolute errors of 1–5 ppm). Uncertainties in the peak amplitudes and the noise levels are mainly caused by the fluctuation in the SC power, which was estimated from a long-term stability measurement. As can be expected, the amplitude of the acoustic signal scales linearly with the concentration ( $R^2 = 0.9997$ ). At  $\text{C}_2\text{H}_4$  concentrations beyond 200 ppm, the amplitude begins to saturate in accordance with the Beer–Lambert law. This observed amplitude nonlinearity at high concentrations was compared to a theoretical nonlinearity of the  $\text{C}_2\text{H}_4$  amplitude to retrieve the effective optical path length. This simulation, based on a reference spectrum from the HITRAN database,<sup>36</sup> the Beer–Lambert law and the instrument lineshape function, yields an optical path length of  $58 \pm 10\text{ cm}$  corresponding to a path length enhancement of  $6.1 \pm 1.1$  and matching well to our achieved signal enhancement in the  $\text{CH}_4$  demonstration.

The noise level exhibits similar dependence with the  $\text{C}_2\text{H}_4$  concentration as the amplitude, because the intensity noise of the SC couples to the PA signal *via* light absorption by gas molecules. Higher concentration yields more absorption and therefore both higher amplitude and noise. This concentration dependent noise component is shown as a dotted green line in Fig. 4(c), extracted from the fit. However, the noise has another contribution from the thermal fluctuations of gas molecules

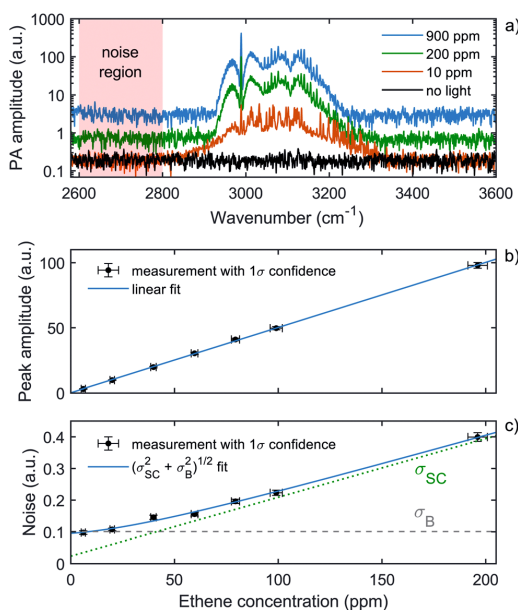


Fig. 4 (a) Measured absorption spectra of  $\text{C}_2\text{H}_4$  at three concentrations and a background spectrum (no light entering the cell), all averaged over 100 s (5 scans) at a spectral resolution of  $1\text{ cm}^{-1}$ . The spectra of  $\text{C}_2\text{H}_4$  include  $\text{H}_2\text{O}$  residual, which is especially visible at the lowest concentration. Red area shows the noise region used in estimating the detection limits, which is justified by the flat noise level across the wavenumber region. (b) Peak amplitude and (c) noise level with respect to the applied  $\text{C}_2\text{H}_4$  concentration. Noise has two contributions: Brownian noise ( $\sigma_B$ ) from the thermal fluctuations of gas molecules corresponding to the background spectrum in (a), and a concentration dependent component from the light source ( $\sigma_{SC}$ ).

(Brownian noise), which begins to dominate below 50 ppm, causing the noise level to approach the fundamental limit. This background noise level (dashed grey line in Fig. 4(c)) was calculated from the measurement with no light entering the cell (black line in Fig. 4(a)) and is consistent with the fitting result. As the noise at low concentrations equals the fundamental noise level, light absorption by the cell windows is expected to be small, which supports our choice for the external multipass system.

### Long-term stability

To evaluate the long-term stability of the SC-based FT-PAS system, we measured 100 ppm of  $\text{C}_2\text{H}_4$  every 40 s for 8320 s. Due to the limitations in the FTS, each 20 s scan followed by a 20 s break, cutting the averaging time in half. Furthermore, distorted measurements (30%) due to external vibrations were removed using Hampel's outlier test for average amplitudes in the frequency range of 710–870 Hz ( $7030\text{--}8610\text{ cm}^{-1}$ ) resulting in an effective averaging time of 2880 s. Water was again subtracted from each spectrum by spectrally fitting pure  $\text{H}_2\text{O}$  and  $\text{C}_2\text{H}_4$  spectra to each raw spectrum with an algorithm (linsolve function in Matlab) that solves a linear least squares

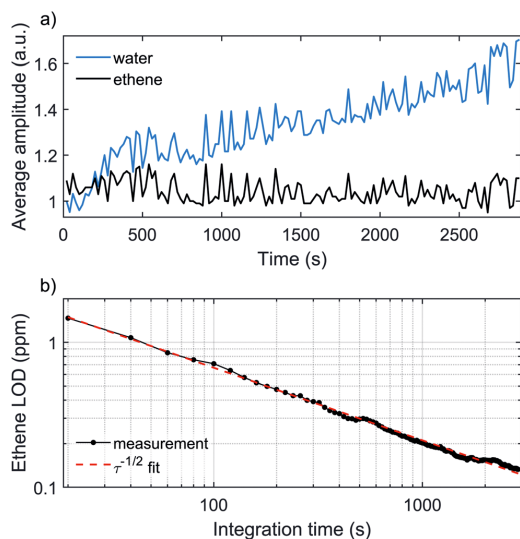


Fig. 5 (a) Separated average amplitudes of  $\text{H}_2\text{O}$  and  $\text{C}_2\text{H}_4$  during the stability measurement, in which a 20 s scan was recorded every 40 s for 5760 s. Due to this dead time, in reality the drifts and variations in the amplitudes occur twice as slow as shown in the plot. (b) Calculated limit of detection (LOD) of  $\text{C}_2\text{H}_4$  for different effective integration times. Water absorption was subtracted from each spectrum to account for the increase of  $\text{H}_2\text{O}$  concentration during the measurement.

problem using QR factorization with column pivoting. The result of this fitting routine is shown in Fig. 5(a), which displays the separated water and ethene traces during the measurement. A significant and slow increase in the  $\text{H}_2\text{O}$  amplitude is due to desorption from the cell walls. The  $\text{C}_2\text{H}_4$  amplitude, on the other hand, stays constant on average but exhibits variations most likely due to SC instability. Corresponding variations are also visible in the  $\text{H}_2\text{O}$  trace. The relative precision of the system (4.8%) was estimated from the standard deviation of the ethene trace relative to its mean. The minimum precision of the system (at  $1\text{ cm}^{-1}$  spectral resolution and for a single scan) is 200 ppb, set by the Brownian noise.

Using a water corrected ethene amplitude at  $2980\text{ cm}^{-1}$  and noise from the raw spectrum (estimated as described previously), we calculated  $\text{C}_2\text{H}_4$  LODs for various integration times. The result of this averaging process shown in Fig. 5(b) displays high stability of the system and a detection limit of 130 ppb in 2880 s for  $\text{C}_2\text{H}_4$ . However, as previously discussed, the correct noise level for the detection limit calculation should be from the  $\text{N}_2$  measurement, and thus a practical  $\text{C}_2\text{H}_4$  detection limit is expected to be about two times smaller. The curve in Fig. 5(b) follows the inverse square root law well on average, as the main noise contributions (pulse-to-pulse SC fluctuations and Brownian noise) exhibit white noise characteristics in this spectral region. Deviations from the theoretical line are caused by the long-term variations of the SC power spectral density and the increase of  $\text{H}_2\text{O}$  inside the cell, which raises the noise level during the measurement.

## Multi-species detection

We demonstrated the advantage of the high system linearity and spectral resolution with the wide spectral bandwidth in retrieving the concentrations of three species from a complex gas mixture. We first measured the reference spectra of ethane (30 ppm), ethene (100 ppm) and propane (20 ppm) by diluting each from a 1% gas bottle to  $\text{N}_2$ . We then prepared a gas mixture containing 20 ppm ethane, 69 ppm ethene and 23 ppm propane, injected the mix to the gas cell and measured the spectrum. Water residual was removed from all spectra. The same least squares spectral fitting routine was used to match the weighted reference spectra to the spectrum of the gas mixture. The resulting scaled spectra of the individual species and the measured gas mixture spectrum are shown in Fig. 6(a) and the residual of the spectral fit in Fig. 6(b).

The concentration of each species in the gas mixture was calculated by multiplying the concentration of the reference measurement with the optimum weight from the fitting routine. Fig. 6(c) illustrates the correspondence between the applied and the retrieved concentrations and shows that the linear spectral fitting is able to retrieve concentrations within the measurement uncertainty. Uncertainties in the applied concentrations result from the dilutions errors caused by the four mass flow controllers, which produce uncertainty also in the retrieved concentrations (*via* reference measurements) together with the system precision estimated previously.

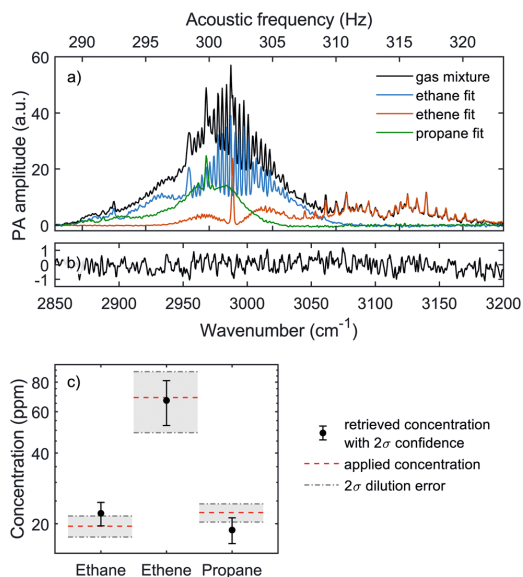


Fig. 6 (a) Measured FT-PAS spectra of a gas mixture (black) and individual species (blue, red and green), whose magnitudes were retrieved from a simple least squares fitting routine. (b) Residual of the spectral fitting. (c) Concentrations retrieved from the gas mixture (black dots), in comparison with the applied concentrations (red dashed lines). The spectral resolution and the total gas pressure of the measurement were  $1\text{ cm}^{-1}$  and 1 bar, respectively.

## 4 Conclusions

A broadband mid-infrared optical gas sensing technique, Fourier transform photoacoustic spectroscopy (FT-PAS) with an external and compact Herriott-type multipass configuration has been demonstrated. Our FT-PAS system incorporates a home-built supercontinuum (SC) source with a high power spectral density and a cantilever enhanced photoacoustic analyser with a small sample volume. We characterized the fundamental C–H stretch bands of four hydrocarbons, methane, ethane, ethene and propane in nitrogen, at spectral resolutions of  $1\text{ cm}^{-1}$  and  $4\text{ cm}^{-1}$  with an excellent agreement with simulated absorption spectra. The Herriott cell for ten beam passes provides a sixfold broadband signal enhancement, resulting in a detection limit of 32 ppb in 40 s for methane. This is a factor of 12 lower compared to the best previous FT-PAS demonstrations and on the same scale with other broadband optical sensors with significantly higher gas consumption,<sup>33,34</sup> when normalized by the averaging time. Moreover, we demonstrated high linearity and good stability of the system, which was shown to provide a simple and accurate spectral analysis of complex gas mixtures.

The detection limit of SC-based FT-PAS can be improved with more transparent windows and further optimization of the multipass arrangement. Ideally, the PA analyser should be redesigned with the multipass enhancement in mind, as increasing the diameter of the gas cell allows more beam passes but decreases the sensitivity of PA detection. The detection limit can be further lowered with commercial SC sources, which currently provide three times higher power spectral density around  $3000\text{ cm}^{-1}$  compared to our device. Such sources would also enhance the precision of the system, which can be further improved by recording the optical power of the exiting radiation for each scan. As this light has propagated through a scanning Fourier transform spectrometer (FTS), an entire SC spectrum could also be continuously acquired for better spectral correction. The selectivity of the current system is limited by the maximum spectral resolution of the FTS. However, complex samples could benefit from higher spectral resolution provided by FTS with a longer optical path difference, which have been reported to reach isotopic selectivity with the cost of significantly increased footprint and lower sensitivity.<sup>11</sup> Dual-comb approach could decrease the size of a high-resolution instrument, but the only system reported so far has limited sensitivity and spectral bandwidth.<sup>12</sup> Lower gas pressures would further improve the selectivity of a high-resolution system.<sup>10</sup>

## Conflicts of interest

There are no conflicts of interest to declare.

## Acknowledgements

This work was supported by the Graduate School of Tampere University and the Academy of Finland Flagship Programme PREIN (320165).

## References

- 1 F. J. Harren and S. M. Cristescu, *Encyclopedia of Analytical Chemistry: Applications, Theory and Instrumentation*, 2006, pp.1–29.
- 2 Z. Bozókí, A. Pogány and G. Szabó, *Appl. Spectrosc. Rev.*, 2011, **46**, 1–37.
- 3 P. Patimisco, G. Scamarcio, F. K. Tittel and V. Spagnolo, *Sensors*, 2014, **14**, 6165–6206.
- 4 K. Wilcken and J. Kauppinen, *Appl. Spectrosc.*, 2003, **57**, 1087–1092.
- 5 T. Tomberg, M. Vainio, T. Hietä and L. Halonen, *Sci. Rep.*, 2018, **8**, 1–7.
- 6 G. Busse and B. Bullemer, *Infrared Phys.*, 1978, **18**, 631–634.
- 7 M. M. Farrow, R. K. Burnham and E. M. Eyring, *Appl. Phys. Lett.*, 1978, **33**, 735–737.
- 8 T. Mikkonen, C. Amiot, A. Aalto, K. Patokoski, G. Genty and J. Toivonen, *Opt. Lett.*, 2018, **43**, 5094–5097.
- 9 T. Mikkonen, Z. Eslami, G. Genty and J. Toivonen, *Opt. Lett.*, 2022, **47**, 1713–1716.
- 10 I. Sadiq, T. Mikkonen, M. Vainio, J. Toivonen and A. Foltynowicz, *Phys. Chem. Chem. Phys.*, 2018, **20**, 27849–27855.
- 11 J. Karhu, T. Tomberg, F. S. Vieira, G. Genoud, V. Hänninen, M. Vainio, M. Metsälä, T. Hietä, S. Bell and L. Halonen, *Opt. Lett.*, 2019, **44**, 1142–1145.
- 12 T. Wildi, T. Voumard, V. Brasch, G. Yilmaz and T. Herr, *Nat. Commun.*, 2020, **11**, 1–6.
- 13 S. Borri, P. Patimisco, I. Galli, D. Mazzotti, G. Giusfredi, N. Akikusa, M. Yamanishi, G. Scamarcio, P. De Natale and V. Spagnolo, *Appl. Phys. Lett.*, 2014, **104**, 091114.
- 14 T. Tomberg, T. Hietä, M. Vainio and L. Halonen, *Analyst*, 2019, **144**, 2291–2296.
- 15 A. Miklós, S.-C. Pei and A. Kung, *Appl. Opt.*, 2006, **45**, 2529–2534.
- 16 J. Saarela, J. Sand, T. Sorvajärvi, A. Manninen and J. Toivonen, *Sensors*, 2010, **10**, 5294–5307.
- 17 K. Chen, B. Zhang, S. Liu, F. Jin, M. Guo, Y. Chen and Q. Yu, *Sens. Actuators, A*, 2019, **290**, 119–124.
- 18 A. Manninen, B. Tuzson, H. Looser, Y. Bonetti and L. Emmenegger, *Appl. Phys. B: Lasers Opt.*, 2012, **109**, 461–466.
- 19 Y. Ma, S. Qiao, Y. He, Y. Li, Z. Zhang, X. Yu and F. K. Tittel, *Opt. Express*, 2019, **27**, 14163–14172.
- 20 C. Hornberger, M. König, S. Rai and W. Demtröder, *Chem. Phys.*, 1995, **190**, 171–177.
- 21 M. Nägele and M. Sigrist, *Appl. Phys. B: Lasers Opt.*, 2000, **70**, 895–901.
- 22 M. Nägele, D. Hofstetter, J. Faist and M. W. Sigrist, *Analytical Sciences/Supplements Proceedings of 11th International Conference of Photoacoustic and Photothermal Phenomena*, 2002, pp. s497–s499.
- 23 K. Krzempek, A. Hudzikowski, A. Gluszek, G. Dudzik, K. Abramski, G. Wysocki and M. Nikodem, *Appl. Phys. B: Lasers Opt.*, 2018, **124**, 74.
- 24 B. Zhang, K. Chen, Y. Chen, B. Yang, M. Guo, H. Deng, F. Ma, F. Zhu, Z. Gong, W. Peng and Q. Yu, *Opt. Express*, 2020, **28**, 6618–6630.
- 25 C. B. Hirschmann, J. Uotila, S. Ojala, J. Tenhunen and R. L. Keiski, *Appl. Spectrosc.*, 2010, **64**, 293–297.



- 26 C. Amiot, A. Aalto, P. Ryczkowski, J. Toivonen and G. Genty, *Appl. Phys. Lett.*, 2017, **111**, 061103.
- 27 A. A. Tovar and L. W. Casperson, *J. Opt. Soc. Am. A*, 1995, **12**, 1522–1533.
- 28 C. G. Tarsitano and C. R. Webster, *Appl. Opt.*, 2007, **46**, 6923–6935.
- 29 J. Altmann, R. Baumgart and C. Weitkamp, *Appl. Opt.*, 1981, **20**, 995–999.
- 30 P. Sievilä, N. Chekurov, J. Raittila and I. Tittonen, *Sens. Actuators, A*, 2013, **190**, 90–95.
- 31 J. Kauppinen, K. Wilcken, I. Kauppinen and V. Koskinen, *Microchem. J.*, 2004, **76**, 151–159.
- 32 T. Kuusela and J. Kauppinen, *Appl. Spectrosc. Rev.*, 2007, **42**, 443–474.
- 33 K. E. Jahromi, M. Nematollahi, Q. Pan, M. A. Abbas, S. M. Cristescu, F. J. Harren and A. Khodabakhsh, *Opt. Express*, 2020, **28**, 26091–26101.
- 34 L. A. Sterczewski, J. Westberg, M. Bagheri, C. Frez, I. Vurgaftman, C. L. Canedy, W. W. Bewley, C. D. Merritt, C. S. Kim, M. Kim, J. R. Meyer and G. Wysocki, *Opt. Lett.*, 2019, **44**, 2113–2116.
- 35 C. Hill, I. E. Gordon, R. V. Kochanov, L. Barrett, J. S. Wilzewski and L. S. Rothman, *J. Quant. Spectrosc. Radiat. Transfer*, 2016, **177**, 4–14.
- 36 L. Rothman, I. Gordon, Y. Babikov, A. Barbe, D. C. Benner, P. Bernath, M. Birk, L. Bizzocchi, V. Boudon, L. Brown, A. Campargue, K. Chance, E. Cohen, L. Coudert, V. Devi, B. Drouin, A. Fayt, J.-M. Flaud, R. Gamache, J. Harrison, J.-M. Hartmann, C. Hill, J. Hodges, D. Jacquemart, A. Jolly, J. Lamouroux, R. L. Roy, G. Li, D. Long, O. Lyulin, C. Mackie, S. Massie, S. Mikhailenko, H. Müller, O. Naumenko, A. Nikitin, J. Orphal, V. Perevalov, A. Perrin, E. Polovtseva, C. Richard, M. Smith, E. Starikova, K. Sung, S. Tashkun, J. Tennyson, G. Toon, V. Tyuterev and G. Wagner, *J. Quant. Spectrosc. Radiat. Transfer*, 2013, **130**, 4–50.



# PUBLICATION

## V

**Detection of gaseous nerve agent simulants with broadband photoacoustic spectroscopy**

T. Mikkonen, D. Luoma, H. Hakulinen, G. Genty, P. Vanninen and J. Toivonen

*Journal of Hazardous Materials* 440.(2022), 129851

**Publication reprinted with the permission of the copyright holders**





Contents lists available at ScienceDirect

## Journal of Hazardous Materials

journal homepage: [www.elsevier.com/locate/jhazmat](http://www.elsevier.com/locate/jhazmat)

## Research Paper

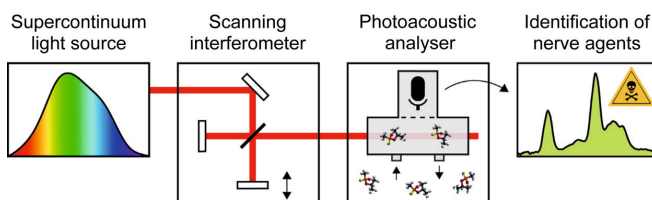
## Detection of gaseous nerve agent simulants with broadband photoacoustic spectroscopy

Tommi Mikkonen<sup>a,\*</sup>, Daniel Luoma<sup>a</sup>, Hanna Hakulinen<sup>b,2</sup>, Goëry Genty<sup>a,3</sup>, Paula Vanninen<sup>b,4</sup>, Juha Toivonen<sup>a,5</sup><sup>a</sup> Photonics Laboratory, Physics Unit, Tampere University, Tampere, Finland<sup>b</sup> Finnish Institute for Verification of the Chemical Weapons Convention (VERIFIN), Department of Chemistry, University of Helsinki, Helsinki, Finland

## HIGHLIGHTS

- Sub-ppm detection of nerve agent simulants.
- Low gas consumption of a few milliliters.
- High selectivity and possibility for multi-species detection.
- Fast response and recovery times.

## GRAPHICAL ABSTRACT



## ARTICLE INFO

## Keywords:

Chemical warfare agent  
Fourier transform spectroscopy  
Supercontinuum  
Gas phase

## ABSTRACT

While recent high-profile assassination attempts have once again brought nerve agents (NAs) into the spotlight, the current portfolio of NA sensors lack a sufficient combination of high performance and field-deployability. Here, we report a novel optical sensor for the detection of gaseous NAs with a potential to fill this gap. The technique is based on Fourier transform spectroscopy with a supercontinuum (SC) light source and cantilever-enhanced photoacoustic detection providing fast multi-species gas sensing with high sensitivity and selectivity in a sample volume of 7 ml, which becomes advantageous when analysing limited NA samples in the field. We study the fundamental C–H stretch bands of four known NA simulants and achieve detection limits of 64–530 ppb in one minute and recovery times of a few minutes. In the near future, the technique has significant potential to improve through the development of more powerful SC sources further in the mid-infrared region.

\* Correspondence to: Faculty of Engineering and Natural Sciences, Tampere University, Finland.

E-mail address: [tommi.mikkonen@tuni.fi](mailto:tommi.mikkonen@tuni.fi) (T. Mikkonen).<sup>1</sup> 0000-0001-7511-2910<sup>2</sup> 0000-0001-7049-1659<sup>3</sup> 0000-0002-0768-3663<sup>4</sup> 0000-0001-9579-0380<sup>5</sup> 0000-0003-0900-174X<https://doi.org/10.1016/j.jhazmat.2022.129851>

Received 30 May 2022; Received in revised form 22 July 2022; Accepted 24 August 2022

Available online 28 August 2022

0304-3894/© 2022 The Author(s). Published by Elsevier B.V. This is an open access article under the CC BY license (<http://creativecommons.org/licenses/by/4.0/>).

## 1. Introduction

The widespread use of chemical warfare agents (CWAs) was initiated in World War I, and despite international efforts to ban their production, stockpiling and exploitation under the Chemical Weapons Convention (1997), CWAs have remained a serious threat in both military and civilian scenarios (Chauhan et al., 2008; Sanderson et al., 2009). An especially lethal class of CWAs are nerve agents (NAs) whose first extensive deployments were in the Iran–Iraq war (1980–88) (Haines and Fox, 2014) and the terrorist attacks in Japan (1994–95) (Seto et al., 2000; Okumura et al., 1996). Recently, NAs have once again ended up at the center of public attention due to incidents in the ongoing Syrian civil war (2011–) (Pita and Domingo, 2014; United Nations, 2013), the assassination of Kim Jong-Nam in Malaysia (2017) (U.S. Department of State, 2020) and the assassination attempts of Sergei Skripal in the United Kingdom (2018) (Vale et al., 2018; Organisation for the Prohibition of Chemical Weapons, 2018a) and Alexei Navalny in Russia (2020) (Organisation for the Prohibition of Chemical Weapons, 2018b).

The toxicity of NAs stem from their ability to irreversibly disrupt the communication of the nervous system, which leads to a wide range of severe consequences depending on the type and dose of the agent and the route of exposure (Costanzi et al., 2018). The most effective passage of NAs into human body is through the respiratory system, where the typically liquid agents can end up as aerosols or vapours due to the volatility of the NAs (e.g., 2800 parts per million (ppm) and 49 ppm for sarin and tabun, respectively, at 20 °C) (Wiener and Hoffman, 2004). Already extremely low NA doses are hazardous, lethal concentrations being 12 ppm and 22 ppm in one minute for gaseous sarin and tabun, respectively (Costanzi et al., 2018), and thus parts per billion (ppb) level detection of these substances in the gas phase is essential. Moreover, NAs are typically detected from urban air or heated liquid/solid field samples with varying concentrations of interfering species, calling for extremely high selectivity against numerous compounds.

The development of NA sensors is largely directed towards portable devices for on-site identification with a fast response time and as high sensitivity and selectivity as possible. The simplest detectors such as electrochemical (Liu and Lin, 2005), colorimetric (Davidson et al., 2020) and fluorimetric sensors (Khan et al., 2018; Meng et al., 2021), surface acoustic wave detectors (Kim et al., 2020) and ion-mobility spectrometers (Puton and Namiesnik, 2016) provide a low-cost option for screening, but they suffer from poor sensitivity, insufficient selectivity and/or susceptibility to changes in temperature and humidity. Technologies with improved performance include gas chromatography mass spectrometry (Smith et al., 2004), Raman spectroscopy (Lafuente et al., 2020) and infrared absorption spectroscopy (Pushkarsky et al., 2006; Mukherjee et al., 2008; Gurton et al., 2012; Levy, 2009; Sharpe et al., 2003; Ruiz-Pesante et al., 2007; Ohru et al., 2020; Melkonian et al., 2020), which are preferred in different scenarios due to their specific characteristics. Infrared absorption spectroscopy is typically well suited for rapid identification of volatile NAs in ambient air, techniques ranging from extremely sensitive photoacoustic spectroscopy (PAS) (Pushkarsky et al., 2006; Mukherjee et al., 2008; Gurton et al., 2012) to Fourier transform infrared spectroscopy (FTIR) (Sharpe et al., 2003; Ruiz-Pesante et al., 2007; Ohru et al., 2020) capable of selective multi-species detection.

These two complementary methods have long been combined in Fourier transform photoacoustic spectroscopy (FT-PAS) (Farrow et al., 1978), which utilizes the parallel down-conversion of optical frequencies of a broadband light into acoustic frequencies, followed by the excitation of absorption-induced pressure waves through periodic thermal relaxations. However, only recent advances in light sources and pressure transducers have fully realized the potential of the technique (Karhu et al., 2019; Mikkonen et al., 2018, 2022b; Sadiek et al., 2018; Wildi et al., 2020). For example, we have previously implemented a supercontinuum (SC) source and a cantilever microphone in a FT-PAS system, which provides fast and selective sensing of hydrocarbons

with ppb-level detection limits in a few milliliter sample volume (Mikkonen et al., 2022b).

Here, we apply FT-PAS to the detection of gaseous NAs by analysing four known NA simulants. We utilize the volatility of the simulants in sampling, where the low gas consumption speeds up the gas exchange process, simplifies the cleaning of the gas cell and would enable the analysis of NA samples with limited availability, a realistic real-life scenario. We examine the unique C–H stretch bands of these species and report our sensor's high performance in terms of detection limits (ppb-level), selectivity and recovery time (a few minutes), convincing the applicability of FT-PAS in reliable and rapid identification of NAs.

## 2. Materials and methods

### 2.1. Experimental setup

The experimental setup illustrated in Fig. 1 closely resembles our previously reported system (Mikkonen et al., 2022b) and has a footprint of about 40 kg and 50 cm × 35 cm × 35 cm when enclosed tightly. The radiation source is a home-built SC (Mikkonen et al., 2018; Amiot et al., 2017), where sub-nanosecond pulses from an erbium-doped fiber laser (1547 nm, 6464 cm<sup>−1</sup>) are injected into two successive optical fibers (a 4-m-long silica dispersion-shifted fiber and an 8.3-m-long fluoride fiber) at 90 kHz repetition rate. The outcome is extensive spectral broadening of the pump up to 3600 nm (2800 cm<sup>−1</sup>) in the long wavelength side. After collimation (2 mm beam diameter), the SC light is spectrally filtered to remove optical power outside the usable wavenumber region, which eliminates water absorption around 3800 cm<sup>−1</sup> and therefore significantly reduces noise (Mikkonen et al., 2022a). A unitless envelope of this filtered SC is shown in the bottom-left corner in Fig. 1 (black line), obtained from a measured (monochromator, Spectral Products DK480 1/2) and post-processed (spectral filtering) spectrum of the SC.

The filtered SC light is directed into a scanning Michelson interferometer (Bruker IRCube), where a slow optical path difference scan velocity of about 0.1 cm/s results in the down-conversion of optical frequencies 2800–3400 cm<sup>−1</sup> into acoustic frequencies 280–340 Hz. This wavenumber-dependent intensity modulation of the light source is schematically illustrated in the bottom-left corner in Fig. 1. The maximum spectral resolution of the interferometer is 1 cm<sup>−1</sup>, but a lower resolution of 4 cm<sup>−1</sup> is selected for this work as the absorption features of NA simulants are relatively broad. For this resolution, a single scan is acquired in five seconds.

The intensity-modulated SC light with 7 mW of optical power is focused into a photoacoustic (PA) analyser (Gasera PA201) and a homebuilt multipass cell (Mikkonen et al., 2022b) which reflects the SC beam ten times through a small cylindrical gas cell (95 mm long, 4 mm in diameter, about 7 ml by total volume). The cumulative power spectral density (PSD) of the SC inside this non-resonant gas cell is shown in Fig. 2a, taking into account the transmittance of the anti-reflection coated BaF<sub>2</sub> windows and a constant 2% loss of the mirrors. The absorption-induced sound waves are detected using an optically read silicon cantilever with a thickness of a few μm, an area of a few mm<sup>2</sup> and a characteristic resonance frequency at 700 Hz (note that the cantilever is operated off-resonance) (Koskinen et al., 2008). The displacement of the cantilever is monitored with a spatial-type interferometer (Kusela and Kauppinen, 2007). The interferogram recorded by the cantilever microphone is windowed (a three-term Blackman-Harris (Naylor and Tahic, 2007)) and Fourier transformed to obtain a background-free absorption spectrum of the gas species inside the cell.

### 2.2. Materials and sampling

We analyse four NA simulants, namely trimethyl phosphate (TMP, Sigma-Aldrich, >99%), dimethyl methylphosphonate (DMMP, Fluka, 97%), diethyl methylphosphonate (DEMP, Sigma-Aldrich, 97.3%) and diisopropyl methylphosphonate (DIMP, Alfa Aesar, 95%), whose

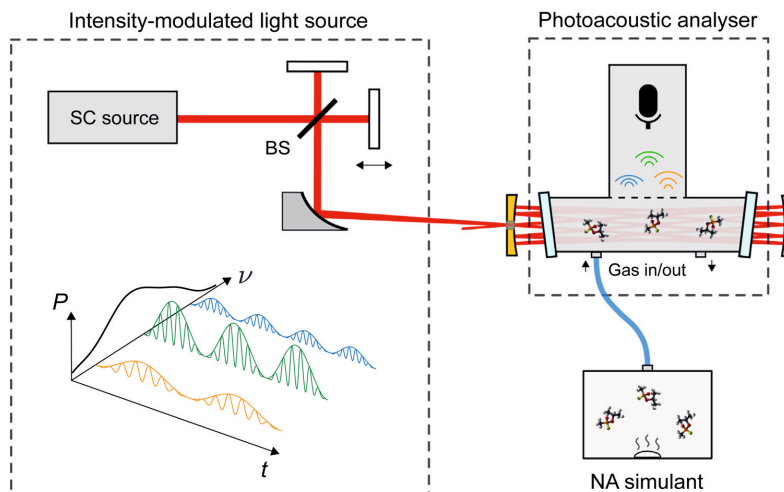


**Fig. 1.** A schematic of the experimental setup: SC - supercontinuum; BS - beamsplitter;  $P$  - optical power;  $\nu$  - wavenumber;  $t$  - time; NA - nerve agent. Wavenumber-dependent intensity modulation of the SC source is illustrated in the bottom left corner, where the relative frequencies are exaggerated. The absolute wavenumber scale of the SC spectrum is shown in Fig. 2a.

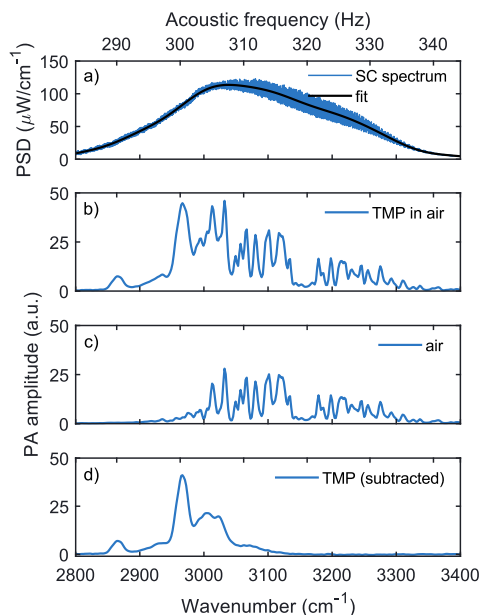


**Fig. 2.** a) Effective power spectral density (PSD) spectrum of the SC radiation inside the gas cell, measured FT-PAS spectrum of b) TMP in air and c) pure air (4 cm<sup>-1</sup> resolution, 60 s measurement time), and d) post-processed spectrum of TMP.

molecular structures and thus spectral properties are similar to G-series NAs such as sarin, tabun and soman (Ruiz-Pesante et al., 2007; Mott and Rez, 2012; Neupane et al., 2019; Kumar et al., 2019). Simulant samples in the gas phase are prepared by placing 20  $\mu$ l of liquid simulant at the bottom of a one-liter container as illustrated at the bottom-right corner in Fig. 1. The liquid simulant in the sampling container is rested for at

least one hour to evaporate, after which the equilibrium vapour pressure at room temperature is assumed to be reached. From the headspace of the container, the gas phase simulants mixed in laboratory air are pumped into the gas cell using a gas exchange system incorporated into the PA analyser. Considering the time to exchange the gas and the time to record a single spectrum, the response time of the sensor is less than ten seconds.

## 2. Results and discussion

### 2.1. Data processing

The measured raw absorption spectrum of TMP in air averaged over 12 scans (one minute) is shown in Fig. 2b. Interfering absorption features in the high-frequency side of the spectrum are from water vapour which dominates the absorption spectrum of air in this spectral region. This interference is eliminated by recording a spectrum of laboratory air (Fig. 2c), fitting that to the TMP-free region (3200–3400 cm<sup>-1</sup>) of the raw spectrum to account for small changes in the water concentration, and subtracting the fitted water spectrum from the raw spectrum. The linear least squares spectral fitting algorithm was implemented using Matlab's `linsolve` function which solves the matrix equation  $Ax = B$  using QR factorization with column pivoting. The same algorithm was employed in all spectral fitting procedures appearing later in this work. The resulting spectrum of pure TMP is shown in Fig. 2d, which is then corrected by the spectral envelope of the SC inside the gas cell shown in black in Fig. 2a.

Corrected FT-PAS spectra of TMP and other simulants are shown in Fig. 3 together with absorption cross section spectra recorded with a conventional FTIR system (Neupane et al., 2019). The measurements agree with each other, FT-PAS spectra exhibiting higher signal-to-noise ratios (SNRs). We note that a small TMP residual was subtracted from the DEMP spectrum. Different magnitudes in the measured spectra result from differences in the absorption cross sections and the concentrations of the simulants inside the cell. These concentrations, which depend on the equilibrium vapour pressures and adsorption properties of the simulant molecules, can be estimated after calibrating the system.

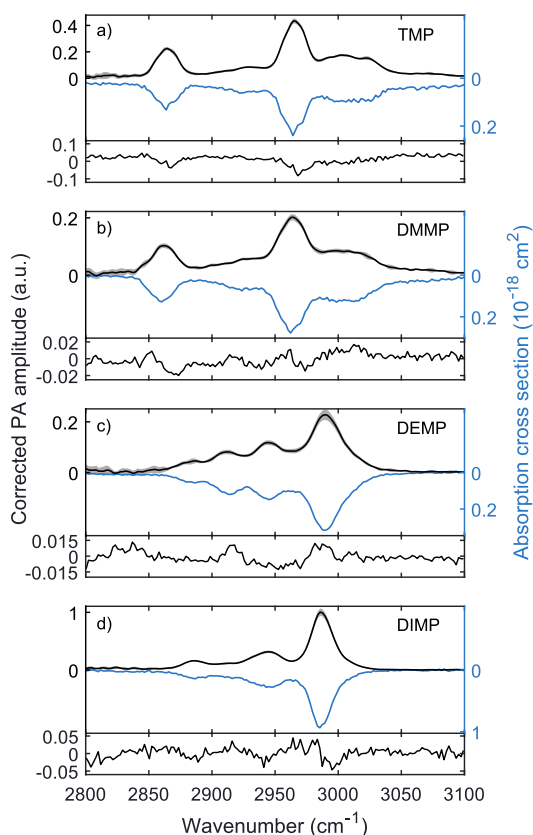


**Fig. 3.** Measured, water-subtracted and PSD-corrected FT-PAS spectra (left axis) and FTIR reference (Neupane et al., 2019) (right axis, inverted) of a) TMP, b) DMMP, c) DEMP and d) DIMP. The average of 12 scans is shown in black and the standard deviation in grey for the FT-PAS spectra. Lower panels show the residuals between these two approaches, acquired by scaling the reference absorption cross sections.

## 2.2. Calibration

Calibration is required in PAS to relate the recorded PA amplitude with the target gas concentration. The calibration process utilizes linear dependence of the wavenumber  $\nu$  dependent PA amplitude  $S(\nu)$  on optical power  $P(\nu)$ , absorption cross section  $\sigma(\nu)$  and concentration  $c$ ,

$$S(\nu) = \Lambda(\nu) * [AP(\nu)\sigma(\nu)c] = AP(\nu)\hat{\sigma}(\nu)c, \quad (1)$$

where  $\Lambda(\nu)$  is the instrument lineshape function (Fourier transform of the window function),  $A$  is the calibration constant, the symbol  $*$  denotes convolution and  $\hat{\sigma}(\nu) = \Lambda(\nu) * \sigma(\nu)$ . The instrument lineshape function does not affect the smoothly varying SC spectral envelope.

As we currently have no reliable way to estimate nor vary the gas phase simulant concentrations in the gas cell, we characterized the calibration constant  $A$  by recording the absorption spectrum (fundamental asymmetric C–H stretch band) of methane ( $\text{CH}_4$ ) with controlled volume mixing ratios between 0.2 and 50 ppm. These volume concentrations were prepared by mixing  $\text{CH}_4$  from a 400 ppm gas bottle with nitrogen using two mass flow controllers (Bronkhorst F-201CV). For simplicity, we only analyzed a single wavenumber ( $\nu_{\text{max}}$ ) corresponding

to the strongest PA amplitude of  $\text{CH}_4$  and measured the linear proportionality constant between  $S(\nu_{\text{max}})$  and  $c$ . We divided this constant by  $P(\nu_{\text{max}})$  and  $\hat{\sigma}(\nu_{\text{max}})$ , which was calculated by convolving the absorption cross section spectrum of  $\text{CH}_4$  (from the HITRAN database (Rothman et al., 2013)) with the instrument lineshape function. This division yields the calibration constant  $A$  for  $\text{CH}_4$ .

Univocal calibration constant for different gas species necessitates constant non-radiative relaxation efficiency (here incorporated into  $A$ ) between the considered species and possible gas mediums, which in general is not the case in PAS (Russo et al., 2021; Müller et al., 2022). However, the situation is considerably simplified here as our modulation frequencies around 300 Hz are unconventionally low for PAS and most importantly lower than the molecular relaxation rates in our gas matrices (Müller et al., 2022; Barreiro et al., 2012). Complete thermal relaxation enables the transfer of the calibration constant of  $\text{CH}_4$  to simulant substances and nerve agents. Simulant concentrations can then be calculated from Eq. 1, where the absorption cross sections of the simulants are collected from the reference FTIR data in Fig. 3. Again, only single wavenumbers corresponding to the maximum absorption cross sections of the simulants are utilized.

Using this calibration procedure, we estimated the simulant concentrations to be in the range of 110–300 ppm in the gas cell as summarized in the second column in Table 1. These concentrations are on average 35% from the initial concentrations in the sampling container (estimated from the vapour pressures of the simulants at 20 °C (Butrow et al., 2009; Cuisset et al., 2008)) due to the adsorption of simulant molecules on the sampling equipment and the surfaces of the gas cell. Sampling efficiencies ( $\eta_s$ ), i.e., the relations between the concentrations in the gas cell and the sampling container, are listed in the third column in Table 1. The observed variations result from measurement errors and various parameters affecting the adsorption process such as polarity and molecular weight (Li et al., 2020). Lower sampling efficiencies of about 10% have been reported for a conventional FTIR system (Ohri et al., 2020), most likely caused by the significantly larger volume of the gas equipment. The uncertainties in the calibrated simulant concentrations shown in the rightmost column of Table 1 include errors in the calibration constant  $A$  (0.5% from the fitting, 3.1% from optical power (Mikkonen et al., 2022b)), and 5% from the absorption cross section of  $\text{CH}_4$  (Daumont et al., 2013), absorption cross sections of simulants (6.2–12% (Neupane et al., 2019)) and optical power again (3.1% (Mikkonen et al., 2022b)).

## 2.3. Detection limits

We estimated the limits of detection (LODs) for all simulants using  $\text{LOD} = 3Nc/S$ , where  $S$  is the strongest PA amplitude of the simulant in the water-corrected spectrum and  $N$  is the noise level, calculated as the standard deviation of a non-absorbing part (2000–2800  $\text{cm}^{-1}$ ) of the water spectrum. The noise level is calculated from a measurement involving no simulant molecules in the gas cell, because significant simulant absorption raises the noise level (Mikkonen et al., 2022a). Calculated detection limits for one minute averaging and corresponding to the minimum concentrations that can be detected inside the gas cell are shown in the fourth column in Table 1. To illustrate the validity of

**Table 1**

Estimated concentrations of four simulants in the gas cell, sampling efficiencies  $\eta_s$ , calculated limits of detection (LODs) in 60 s for simulant samples inside or outside the gas cell, and relative uncertainties in the concentrations and LODs.

Simulant	$c$ (ppm)	$\eta_s$ (%)	LOD (ppb)		$\Delta c$ (%)
			In	Out	
TMP	310	36	130	360	14
DMMP	160	20	110	530	10
DEMP	160	43	79	190	10
DIMP	120	42	26	64	10



this unconventional determination of the detection limit, we measured a small concentration (230 ppb) of DIMP in which case the noise induced by the simulant is negligible and the LOD can be obtained directly from the SNR of the spectrum. A single water-subtracted scan of this measurement is shown in Fig. 4 with a SNR of  $7.7 \pm 0.3$  corresponding to a LOD of  $26 \pm 1$  ppb in 60 s, in perfect agreement with the value in Table 1. The uncertainty includes only the fitting error (no calibration error).

In order to estimate the detection limits that can be reached from samples outside the sensor, the LOD values in the fourth column in Table 1 were divided by the corresponding sampling efficiencies resulting in values of 64–530 ppb (the fifth column in Table 1). By comparing the absorption cross sections of sarin and TMP (Sharpe et al., 2003; Neupane et al., 2019) and assuming 35% sampling efficiency, we estimated a detection limit of  $180 \pm 40$  ppb for sarin which is approximately an order of magnitude higher compared to a LOD achieved with a commercial, high-performance and field-portable FTIR system when normalized by the acquisition time (Ohruai et al., 2020). However, it should be noted that the required sample volume of our system is 57 times smaller and the FTIR system capitalizes on stronger P–O–C stretch bands around  $1000\text{ cm}^{-1}$ .

#### 2.4. Selectivity

Similar features in the C–H stretch bands of some simulants (Fig. 3) and NAs (Sharpe et al., 2003) could indicate complications in the correct identification of these species. We investigated the selectivity of our sensor by compiling a spectral library of the simulants (and water) and performing new single-component and single-scan measurements with these four substances and concentrations ranging 20–40 ppm. Using the spectral library and the least squares spectral fitting algorithm, we estimated the concentration of each species in the gas cell. For each simulant, we repeated this process for five scans, averaged the retrieved concentrations simulant-wise and calculated the absolute values (for illustration purposes as negative values cannot be displayed in a logarithmic scale). The results are shown in Fig. 5 where each row represents the outcome for a specific simulant applied in the gas cell (applied simulant on the left panel, retrieved simulants on the bottom panel).

Noting the logarithmic color scale, Fig. 5 displays good selectivity of the system. All simulants were confidently identified and the average concentration for absent species is 300 ppb (values outside the diagonal). Most remarkably, small differentiating features in the absorption spectra of TMP and DMMP are successfully recognized with no particular cross-sensitivity between these simulants. The most prominent incorrect detection was 1 ppm of DMMP in the DIMP measurement (fourth row, second column), which however may be attributed to

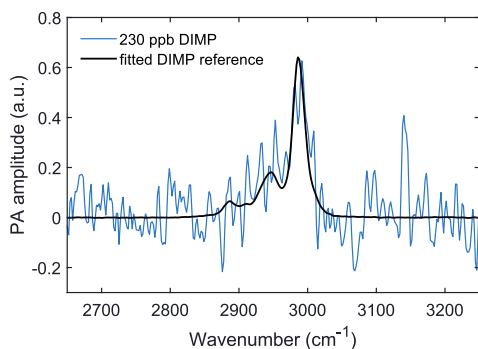


Fig. 4. A single scan, water-subtracted spectrum of 230 ppb of DIMP (blue line) and a fitted DIMP reference (black line) obtained experimentally at a high concentration.

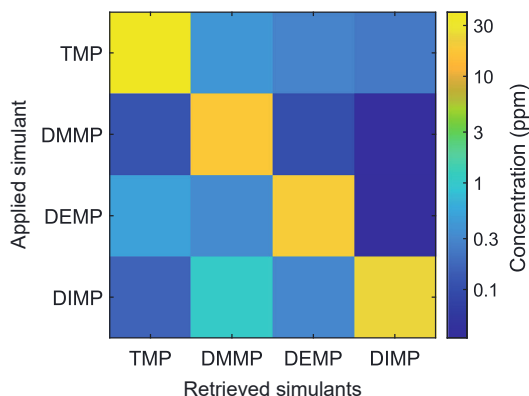


Fig. 5. An illustration of the system's selectivity, compiled from single-component and single-scan measurements of four simulants (left). For each raw spectrum, a library of simulant references was fitted to retrieve the concentrations of the simulants (bottom) in the gas cell. For each simulant, five single scans were acquired, and the final result (each row) shows absolute values of the average retrieved concentrations. Absolute values were calculated due to the logarithmic scale. For example, the analysis of the DIMP measurement is shown at the bottom row, which displays retrieved concentrations of 0.2 ppm, 1 ppm, 0.3 ppm and 30 ppm for TMP, DMMP, DEMP and DIMP, respectively. Average uncertainty in the retrieved concentrations was 42% (fitting error).

residual DMMP in the sampling container (DIMP sample was placed in a container that previously contained DMMP). Similar reasoning also holds for the second most prominent incorrect detection, 500 ppb of TMP in the DEMP measurement. This underlines the difficulty in handling volatile substances and the importance of thorough cleaning of all contaminated surfaces. Without these two doubtful incorrect identifications, the average concentration for absent species is 200 ppb, which is 0.8% from the average applied concentration and around the noise level of the high concentration (and therefore high noise level) measurements.

#### 2.5. Recovery time

An important feature for a NA sensor is the ability to recover fast after encountering high concentrations. In our system, recovery time is limited by the gas adsorption onto the inner surface of the gas cell and the pump system whereof it evaporates back into gas phase after the cell is purged with clean air. It is therefore favourable to change the gas sample inside the cell after each scan which was the procedure in all our measurements. The duration of this cleaning depends on the substance, its initial concentration in the gas cell and the concentration in which the substance cannot be anymore detected, high initial concentrations of sticky molecules with low detection limits exhibiting the longest recovery times. Therefore, we characterized the cleaning of the gas equipment in the worst scenario by injecting a high concentration (100 ppm) of DIMP in the gas cell. We repeated 71 times a sequence of flushing the cell with clean air for two seconds and recording a single spectrum. The concentration of DIMP was retrieved from each raw spectrum by fitting DIMP and water references to the spectrum, and the result of this investigation is shown in Fig. 6.

The concentration of DIMP decreases three orders of magnitude during the flushing procedure. A three-term exponential function was fitted to the concentration trace as three separate evaporation processes are present in the system: one in the gas cell and two in the two gas tube systems delivering the sample in the cell. These three contributions are shown in Fig. 6. The sampling tubes are efficiently cleaned within the

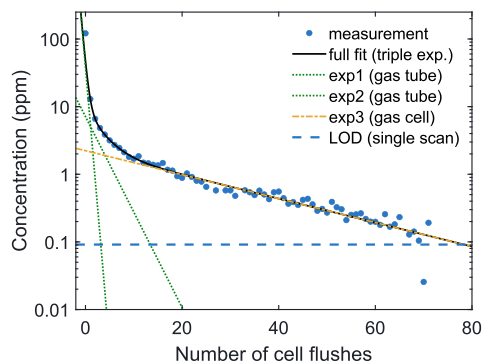


**Fig. 6.** Concentration of DIMP (blue dots) for increasing number of 2 s flushes of the gas cell with clean air, triple exponential fit (solid black line), three components of the fit (dashed green and yellow lines) and the limit of detection in 5 s (dashed blue line).

first ten flushes, after which the DIMP concentration decreases more slowly and is dominated by the adsorbed substance in the gas cell. From the fitted line, we can estimate the number of flushes required to decrease the simulant concentration below the single-scan LOD (dashed line in Fig. 6). For DIMP with an initial concentration of about 100 ppm, 80 flushes correspond to a recovery time of 160 s in terms of active pumping, or  $\sim 12$  min in terms of continuous monitoring in which a spectrum is recorded after each 2 s flush. For lower initial concentrations of DIMP and for other simulants, this time is expected to be shorter. Moreover, heated gas equipment would accelerate the recovery significantly.

#### 4. Conclusions

We have demonstrated Fourier transform photoacoustic spectroscopy (FT-PAS) with a supercontinuum (SC) light source for the detection of gaseous nerve agents (NAs). This approach combines the broadband nature of Fourier transform spectroscopy with the high sensitivity of cantilever-enhanced PAS for a field-deployable sensor with high performance. We analysed the C–H stretch bands of four NA simulants whose measured absorption spectra were in a good agreement with the literature (Neupane et al., 2019). We achieved detection limits of 64–530 ppb in 60 s for the simulants, which should be considered in the context of the system's low gas consumption (7 ml), high selectivity and the possibility for simultaneous multi-species detection (Mikkonen et al., 2022b). While our attained detection sensitivity is an order of magnitude worse compared to a conventional FTIR system with similar footprint (Ohruai et al., 2020), the required sample volume is nearly 60 times smaller providing a significant advantage when analysing field samples with limited availability. Furthermore, low gas consumption increases the sampling efficiency and is expected to decrease the recovery time of the sensor, which for our system was demonstrated to be in the range of a few minutes for an initially high sample concentration.

The performance of the sensor could be significantly enhanced by analysing the stronger and more selective P–O–C stretch bands further in the mid-infrared region (Sharpe et al., 2003; Neupane et al., 2019), where commercial SC sources are currently not available but expected in the near future. This would be especially beneficial when dealing with complex samples that require the construction of a spectral library containing all expected interferences. However, the current sensor operating around  $3000\text{ cm}^{-1}$  has been demonstrated to perform sufficiently in multi-species hydrocarbon detection (Mikkonen et al., 2022b). In this spectral region, the sensitivity can most simply be enhanced by using a SC source with higher power spectral density and optimizing the

multipass cell with better windows. In addition to temporal averaging (Mikkonen et al., 2022b), the detection limits could be further lowered by a factor of six with higher sampling efficiency (by heating the gas equipment), faster scanning velocity and better elimination of water absorption. The precision of the sensor is largely limited by the power variations of the light source, which can be eliminated by continuous power monitoring. Furthermore, the accuracy could be improved with a better calibration against a reference sensor. Especially with these advancements, the demonstrated technique provides a novel and complementary tool for high-performance identification of NAs for example in the diagnosis of poisoning and forensic investigation.

#### Environmental implication

The materials studied in this work are four organophosphorus compounds, which themselves possess a moderate health hazard. However, here we use these compounds to simulate volatile nerve agents such as sarin, soman and tabun, which are one of the most lethal chemical weapons. Our work presents a novel technique for the detection of gaseous nerve agents with high performance and low sample consumption. The approach provides a complementary tool for the analysis of complex field samples with limited availability, thus contributing to faster and more reliable identification for forensic investigation, the diagnosis and treatment of poisoning and occupational health monitoring.

#### CRedit authorship contribution statement

**Tommi Mikkonen:** Conceptualization, Methodology, Formal analysis, Investigation, Writing – original draft, Visualization. **Daniel Luoma:** Investigation, Data curation. **Hanna Hakulinen:** Conceptualization, Resources. **Goëry Genty:** Resources, Writing – review & editing. **Paula Vanninen:** Conceptualization, Resources. **Juha Toivonen:** Conceptualization, Resources, Writing – review & editing, Supervision.

#### Declaration of Competing Interest

The authors declare that they have no known competing financial interests or personal relationships that could have appeared to influence the work reported in this paper.

#### Data Availability

Data will be made available on request.

#### Acknowledgements

This work was supported by the Graduate School of Tampere University and the Academy of Finland Flagship Programme PREIN (grant 320165).

#### References

- Amiot, C., Aalto, A., Ryczkowski, P., Toivonen, J., Genty, G., 2017. Cavity enhanced absorption spectroscopy in the mid-infrared using a supercontinuum source. *Appl. Phys. Lett.* 111 (6), 061103.
- Barreiro, N., Peuriot, A., Santiago, G., Slezak, V., 2012. Water-based enhancement of the resonant photoacoustic signal from methane–air samples excited at  $3.3\text{ }\mu\text{m}$ . *Appl. Phys. B* 108 (2), 369–375.
- Butrow, A.B., Buchanan, J.H., Tevaut, D.E., 2009. Vapor pressure of organophosphorus nerve agent simulant compounds. *J. Chem. Eng. Data* 54 (6), 1876–1883.
- Chauhan, S., R.D'cruz, Faruqi, S., Singh, K., Varma, S., Singh, M., Karthik, V., 2008. Chemical warfare agents. *Environ. Toxicol. Pharmacol.* 26 (2), 113–122.
- Costanzi, S., Machado, J.-H., Mitchell, M., 2018. Nerve agents: what they are, how they work, how to counter them. *ACS Chem. Neurosci.* 9 (5), 873–885.
- Cuisset, A., Mouret, G., Pirali, O., Roy, P., Cazier, F., Nouali, H., Demaison, J., 2008. Gas-phase vibrational spectroscopy and ab initio study of organophosphorus compounds: Discrimination between species and conformers. *J. Phys. Chem. B* 112 (39), 12516–12525.

- Daumont, L., Nikitin, A., Thomas, X., Régalia, L., VonderHeyden, P., Tyuterev, V.G., Rey, M., Boudon, V., Wenger, C., Loëte, M., et al., 2013. New assignments in the 2  $\mu\text{m}$  transparency window of the  $^{12}\text{CH}_4$  Octad band system. *J. Quant. Spectrosc. Radiat. Transf.* 116, 101–109.
- Davidson, C.E., Dixon, M.M., Williams, B.R., Kilper, G.K., Lim, S.H., Martino, R.A., Rhodes, P., Hulet, M.S., Miles, R.W., Samuels, A.C., et al., 2020. Detection of chemical warfare agents by colorimetric sensor arrays. *ACS Sens.* 5 (4), 1102–1109.
- Farrow, M.M., Burnham, R.K., Eyring, E.M., 1978. Fourier-transform photoacoustic spectroscopy. *Appl. Phys. Lett.* 33 (8), 735–737.
- Gurton, K.P., Felton, M., Tober, R., 2012. Selective real-time detection of gaseous nerve agent simulants using multiwavelength photoacoustics. *Opt. Lett.* 37 (16), 3474–3476.
- Haines, D.D., Fox, S.C., 2014. Acute and long-term impact of chemical weapons: lessons from the Iran-Iraq war. *Forensic Sci. Rev.* 26 (2), 97–114.
- Karhu, J., Tomberg, T., Vieira, F.S., Genoud, G., Hänninen, V., Vainio, M., Metsälä, M., Hieta, T., Bell, S., Halonen, L., 2019. Broadband photoacoustic spectroscopy of  $^{14}\text{CH}_4$  with a high-power mid-infrared optical frequency comb. *Opt. Lett.* 44 (5), 1142–1145.
- Khan, M.S.J., Wang, Y.-W., Senge, M.O., Peng, Y., 2018. Sensitive fluorescence on-off probes for the fast detection of a chemical warfare agent mimic. *J. Hazard. Mater.* 342, 10–19.
- Kim, J., Kim, E., Kim, J., Kim, J.-H., Ha, S., Song, C., Jang, W.J., Yun, J., 2020. Four-channel monitoring system with surface acoustic wave sensors for detection of chemical warfare agents. *J. Nanosci. Nanotechnol.* 20 (11), 7151–7157.
- Koskinen, V., Fonsen, J., Roth, K., Kauppinen, J., 2008. Progress in cantilever enhanced photoacoustic spectroscopy. *Vib. Spectrosc.* 48 (1), 16–21.
- Kumar, N., Tiwari, K.R., Meenu, K., Sharma, A., Jain, A., Singh, S., Tomar, R., et al., 2019. Utilization of various analogy of synthetic nanoporous zeolites and composite of zeolites for decontamination/detoxification of CWA simulants—an updated review. *Int. J. Nonferrous Metall.* 8 (04), 35.
- Kuusela, T., Kauppinen, J., 2007. Photoacoustic gas analysis using interferometric cantilever microphone. *Appl. Spectrosc. Rev.* 42 (5), 443–474.
- Lafuente, M., Sanz, D., Urbiztondo, M., Santamaría, J., Pina, M.P., Mallada, R., 2020. Gas phase detection of chemical warfare agents CWAs with portable Raman. *J. Hazard. Mater.* 384, 121279.
- Levy, D., 2009. Advances in portable FTIR spectrometers for the field: the HazMatID Ranger. In: *Next-Generation Spectroscopic Technologies II*, Vol. 7319. International Society for Optics and Photonics, p. 73190E (p).
- Li, X., Zhang, L., Yang, Z., Wang, P., Yan, Y., Ran, J., 2020. Adsorption materials for volatile organic compounds (VOCs) and the key factors for VOCs adsorption process: a review. *Surf. Purif. Technol.* 235, 116213.
- Liu, G., Lin, Y., 2005. Electrochemical sensor for organophosphate pesticides and nerve agents using zirconia nanoparticles as selective sorbents. *Anal. Chem.* 77 (18), 5894–5901.
- Melkonian, J.-M., Armougou, J., Raybaut, M., Dherbecourt, J.-B., Gorju, G., Cézard, N., Godard, A., Pašiškevičius, V., Coetzee, R., Kadlčák, J., 2020. Long-wave infrared multi-wavelength optical source for standoff detection of chemical warfare agents. *Appl. Opt.* 59 (35), 11156–11166.
- Meng, W., Pei, Z., Wang, Y., Sun, M., Xu, Q., Cen, J., Guo, K., Xiao, K., Li, Z., 2021. Two birds with one stone: The detection of nerve agents and AChE activity with an ICT-ESIPT-based fluorescence sensor. *J. Hazard. Mater.* 410, 124811.
- Mikkonen, T., Eslami, Z., Genty, G., Toivonen, J., 2022a. Supercontinuum intensity noise coupling in Fourier transform photoacoustic spectroscopy. *Opt. Lett.* 47 (7), 1713–1716.
- Mikkonen, T., Hieta, T., Genty, G., Toivonen, J., 2022b. Sensitive multi-species photoacoustic gas detection based on mid-infrared supercontinuum source and miniature multipass cell. *Phys. Chem. Chem. Phys.* 24, 19481–19487.
- Mikkonen, T., Amiot, C., Aalto, A., Patokoski, K., Genty, G., Toivonen, J., 2018. Broadband cantilever-enhanced photoacoustic spectroscopy in the mid-IR using a supercontinuum. *Opt. Lett.* 43 (20), 5094–5097.
- Mott, A.J., Rez, P., 2012. Calculated infrared spectra of nerve agents and simulants. *Spectrochim. Acta Part A: Mol. Biomol. Spectrosc.* 91, 256–260.
- Mukherjee, A., Dunayevskiy, I., Prasanna, M., Go, R., Tsekoun, A., Wang, X., Fan, J., Patel, C.K.N., 2008. Sub-parts-per-billion level detection of dimethyl methyl phosphonate (DMMP) by quantum cascade laser photoacoustic spectroscopy. *Appl. Opt.* 47 (10), 1543–1548.
- Müller, M., Rück, T., Jobst, S., Pangerl, J., Weigl, S., Bieri, R., Matysik, F.-M., 2022. An algorithmic approach to compute the effect of non-radiative relaxation processes in photoacoustic spectroscopy. *Photoacoustics*, 100371.
- Naylor, D.A., Tahir, M.K., 2007. Apodizing functions for Fourier transform spectroscopy. *JOSA A* 24 (11), 3644–3648.
- Neupane, S., Peale, R., Vasu, S., 2019. Infrared absorption cross sections of several organo-phosphorous chemical-weapon simulants. *J. Mol. Spectrosc.* 355, 59–65.
- Ohrui, Y., Hashimoto, R., Ohmori, T., Seto, Y., Inoue, H., Nakagaki, H., Yoshikawa, K., McDermott, L., 2020. Continuous monitoring of chemical warfare agents in vapor using a Fourier transform infra-red spectroscopy instrument with multi pass gas cell, mercury cadmium telluride detector and rolling background algorithm. *Forensic Chem.* 21, 100292.
- Okumura, T., Takasu, N., Ishimatsu, S., Miyanoi, S., Mitsuhashi, A., Kumada, K., Tanaka, K., Hinohara, S., 1996. Report on 640 victims of the Tokyo subway sarin attack. *Ann. Emerg. Med.* 28 (2), 129–135.
- Organisation for the Prohibition of Chemical Weapons, 2018a. Summary of the report on activities carried out in support of a request for technical assistance by the United Kingdom of Great Britain and Northern Ireland, (Accessed 23 September 2021) [https://www.opcw.org/sites/default/files/documents/S series/2018/en/s-1612-2018\\_e1.pdf](https://www.opcw.org/sites/default/files/documents/S%20series/2018/en/s-1612-2018_e1.pdf).
- Organisation for the Prohibition of Chemical Weapons, 2018b. Summary of the report on activities carried out in support of a request for technical assistance by Germany, (Accessed 23 September 2021) <https://www.opcw.org/documents/2020/0/s19062020/note-technical-secretariat-summary-report-activities-carried-out>.
- Pita, R., Domingo, J., 2014. The use of chemical weapons in the Syrian conflict. *Toxics* 2 (3), 391–402.
- Pushkarsky, M.B., Webber, M.E., Macdonald, T., Patel, C.K.N., 2006. High-sensitivity, high-selectivity detection of chemical warfare agents. *Appl. Phys. Lett.* 88 (4), 044103.
- Puton, J., Namieśnik, J., 2016. Ion mobility spectrometry: current status and application for chemical warfare agents detection. *TrAC Trends Anal. Chem.* 85, 10–20.
- Rothman, L., Gordon, I., Babikov, Y., Barbe, A., Benner, D.C., Bernath, P., Birk, M., Bizzocchi, L., Boudon, V., Brown, L., Campargue, A., Chance, K., Cohen, E., Couder, L., Devi, V., Drouin, B., Fayt, A., Flaud, J.-M., Gamache, R., Harrison, J., Hartmann, J.-M., Hill, C., Hodges, J., Jacquemart, D., Jolly, A., Lamouroux, J., Roy, R.L., Li, G., Long, D., Lyulin, O., Mackie, C., Massie, S., Mikhailenko, S., Müller, H., Naumenko, O., Nikitin, A., Orphal, J., Perevalov, V., Perrin, A., Polovtseva, E., Richard, C., Smith, M., Starikova, E., Sung, K., Tashkun, S., Tennyson, J., Toon, G., Tyuterev, V., Wagner, G., 2013. The HITRAN2012 molecular spectroscopic database. *J. Quant. Spectrosc. Radiat. Transf.* 130, 4–50. HITRAN2012 special issue.
- Ruiz-Pesante, O., Pacheco-Londoño, L.C., Primera-Pedrozo, O.M., Ortiz, W., Soto-Feliciano, Y.M., Nieves, D.E., Ramirez, M.L., Hernández-Rivera, S.P., 2007. Detection of simulants and degradation products of chemical warfare agents by vibrational spectroscopy. In: *Chemical and Biological Sensing VIII*, Vol. 6554. International Society for Optics and Photonics, p. 65540B (p).
- Russo, S.D., Sampaolo, A., Patimisco, P., Menduni, G., Giglio, M., Hoelzl, C., Passaro, V.M., Wu, H., Dong, L., Spagnolo, V., 2021. Quartz-enhanced photoacoustic spectroscopy exploiting low-frequency tuning forks as a tool to measure the vibrational relaxation rate in gas species. *Photoacoustics* 21, 100227.
- Sadiek, I., Mikkonen, T., Vainio, M., Toivonen, J., Foltynowicz, A., 2018. Optical frequency comb photoacoustic spectroscopy. *Phys. Chem. Chem. Phys.* 20 (44), 27849–27855.
- Sanderson, H., Fauser, P., Thomsen, M., Sørensen, P.B., 2009. Human health risk screening due to consumption of fish contaminated with chemical warfare agents in the Baltic Sea. *J. Hazard. Mater.* 162 (1), 416–422.
- Seto, Y., Tsunoda, N., Kataoka, M., Tsuge, K., Nagano, T., 2000. Toxicological analysis of victims' blood and crime scene evidence samples in the sarin gas attack caused by the Aum Shinrikyo cult. *ACS Publications*, pp. 318–332. Ch. 21, pp.
- Sharpe, S.W., Johnson, T.J., Chu, P.M., Kleimyer, J., Rowland, B., 2003. Quantitative infrared spectra of vapor phase chemical agents. In: *Chemical and Biological Sensing IV*, Vol. 5085. International Society for Optics and Photonics, pp. 19–27 (pp).
- Smith, P.A., Koch, D., Hook, G.L., Erickson, R.P., Lepage, C.R.J., Wyatt, H.D., Betsinger, G., Eckenrode, B.A., 2004. Detection of gas-phase chemical warfare agents using field-portable gas chromatography-mass spectrometry systems: instrument and sampling strategy considerations. *TrAC Trends Anal. Chem.* 23 (4), 296–306.
- U.S. Department of State, 2020. Imposition of chemical and biological weapons control and warfare elimination act sanctions on North Korea, (Accessed 23 September 2021) <https://2017-2021.state.gov/imposition-of-chemical-and-biological-weapon-control-and-warfare-elimination-act-sanctions-on-north-korea/index.html>.
- United Nations, 2013. Report of the United Nations Mission to Investigate Allegations of the Use of Chemical Weapons in the Syrian Arab Republic on the alleged use of chemical weapons in the Ghouta area of Damascus on 21 August 2013, (Accessed 22 September 2021) <https://www.un.org/zh/focus/northafrica/cwinvestigation.pdf>.
- Vale, J.A., Marrs, T.C., Maynard, R.L., 2018. Novichok: a murderous nerve agent attack in the UK. *Clin. Toxicol.* 56 (11), 1093–1097.
- Wiener, S.W., Hoffman, R.S., 2004. Nerve agents: a comprehensive review. *J. Intensive Care Med.* 19 (1), 22–37.
- Wildt, T., Voumard, T., Brasch, V., Yilmaz, G., Herr, T., 2020. Photo-acoustic dual-frequency comb spectroscopy. *Nat. Commun.* 11 (1), 1–6.





